RADIATION MEASUREMENTS FROM POLAR AND GEOSYNCHRONOUS SATELLITES

T. H. VONDER HAAR, PRINCIPAL INVESTIGATOR

FINAL REPORT
GRANT NGR-06-002-102
PERIOD:
10 OCTOBER 1970 – 31 JULY 1978

DEPARTMENT OF ATMOSPHERIC SCIENCE
COLORADO STATE UNIVERSITY
FORT COLLINS, COLORADO

RADIATION MEASUREMENTS FROM POLAR AND GEOSYNCHRONOUS SATELLITES

Annual Report
(Period: 1 November 1976 - 31 October 1977)

and

Final Report
(10 October 1970 - 31 July 1978)

for

National Aeronautics and Space Administration
Grant NGR-06-002-102

by

Thomas H. Vonder Haar, Principal Investigator
Department of Atmospheric Science
Colorado State University

With Contributions by:
Stanley Q. Kidder
Donald W. Hillger
James S. Ellis

June 1978

Technical Monitor: Robert Curran

F
A

SUMMARY

During the final annual period of Grant NGR-06-002-102 (1 November 1976 - 31 October, 1977) work was done in five areas: climate, radiation budget, oceanic precipitation, mesoscale weather and tropical storm measurements:

1) A Ph.D. dissertation investigating the role that clouds play in climate determinations was completed.

2) A paper on the annual variation of the global heat balance of the earth was submitted for publication.

3) Progress was made in an attempt to determine the accuracy of precipitation estimates made from passive microwave measurements from satellites. Also a paper on seasonal oceanic precipitation frequencies was published.

4) A paper on obtaining mesoscale temperature and moisture fields over land from VTPR data was published.

5) Some initial work was done on obtaining surface winds and pressures in tropical storms from Nimbus 6 Scanning Microwave Spectrometer data.

During the annual period the Grant fully supported one Ph.D. candidate and sponsored the publication of two papers, the completion of one Ph.D. dissertation and the initial work on a paper presented in December 1977.

TABLE OF CONTENTS

SUMMARY

1.0 INTRODUCTION

2.0 DISCUSSION OF SCIENTIFIC RESULTS

- 2.1 Cloud Albedo for Global Climate Studies
- 2.2 Variation of the Annual Cycle of the Radiation Budget Components
- 2.3 Oceanic Precipitation
- 2.4 Mesoscale Temperature and Moisture Fields from VTPR Data
- 2.5 Tropical Storm Surface Winds and Pressures from Nimbus 6 Scanning Microwave Spectrometer (SCAMS) Data

REFERENCES

APPENDIX A: Cumulative Summary of Papers and Publications Sponsored by Grant NGR-06-002-102.

B: Papers and Publications Produced during the Annual Period 1 November 1976 - 31 October 1977.

1.0 INTRODUCTION

During the 7 years of sponsorship, more than 35 papers and publications have been produced under Grant NGR-06-002-102. A complete list appears in Appendix A. During the final year of grant sponsorship, two papers were published, one was accepted for publication, one Ph.D. dissertation was completed, and the initial work for a paper presented in December 1977 was done. One Ph.D. student (S. Kidder) was fully supported by the Grant and several research staff were partially supported. A brief discussion of scientific results is given below.

2.0 DISCUSSION OF SCIENTIFIC RESULTS

2.1 Cloud Albedo for Global Climate Studies

J. Ellis (1978) has used radiation budget measurements from Nimbus-3 and from a 29 month composite from six satellites (Vonder Haar and Ellis, 1974) to investigate the effects of clouds on the radiation budget of the earth. He found that clouds affect the absorbed shortwave flux more than the emitted longwave flux and that this effect is larger over the ocean than over the land. He showed that other things being equal, an increase in global cloud amount would cause a decrease in the global mean surface temperature, and that clouds tend to moderate climate variation by reducing the amplitude of the inter-annual variation in the planetary net radiation budget. Contrary to the results of Cess (1976), his study shows the definite and significant importance of clouds on the earth's radiation budget. These and other findings comprise Ellis' Ph.D. dissertation which appears in Appendix B.

2.2 Variation of the Annual Cycle of the Radiation Budget Components

In a companion study to Oort and Vonder Haar (1976), Ellis, Vonder Haar, Oort and Levitus (1977) have used satellite radiation budget data, atmospheric energy transport data, and ocean temperature data to obtain the annual variation in the global heat balance of the earth. Their paper has been submitted to the Journal of Geophysical Research. (See Appendix B.)

2.3 Oceanic Precipitation

Progress was made on our project to investigate the accuracy which one can expect from precipitation measurements from passive satellite microwave data. A copy of a Mie scattering program, with which to calculate the brightness temperatures for various rainfall rates and atmospheric/surface conditions, was obtained from Robert Curran of Goddard Space Flight Center. Data for model input and for checking the output was collected, and progress was made on converting the model from the infrared to the microwave portion of the spectrum. But much remains to be done.

A paper by Kidder and Vonder Haar (1977) entitled "Seasonal Oceanic Precipitation Frequencies from Nimbus 5 Microwave Data" was published in the Journal of Geophysical Research. A reprint appears in Appendix B.

2.4 Mesoscale Temperature and Moisture Fields from VTPR Data

A paper by Hillger and Vonder Haar (1977) entitled "Deriving Mesoscale Temperature and Moisture Fields from Satellite Radiance Measurements Over the United States" was published in the Journal of Applied Meteorology. It covers work performed and reported on earlier under this grant. (See Appendix B.)

2.5 Tropical Storm Surface Winds and Pressures from Nimbus 6 Scanning Microwave Spectrometer (SCAMS) Data

Some initial work was done on a project to obtain information on the surface winds and pressures in tropical storms from the 55.45 GHz channel of SCAMS. The basic idea is that the weighting function for this channel peaks in the region of the maximum warm anomaly above the storm. The 55.45 GHz brightness temperature, therefore, provides information on the mean warming in the column and thus the surface pressure. A correlation coefficient of -.86 was found between brightness temperature anomalies (difference from mean conditions 4-10° latitude from the storm center) and central pressure for 13 storms during 1975. Also an attempt was made to calculate outer surface winds from pressure gradients. A paper on the subject (Kidder, _et_ _al_., 1977) was given in December, 1977. (See Appendix B.)

REFERENCES

Cess, R.D., 1976: Climate change: An appraisal of atmospheric feedback mechanisms employing zonal climatology. *Journal of the Atmospheric Sciences*, Vol. 33, No. 10, pp. 1831-1843.

Ellis, J.S., 1978: Cloudiness, the planetary radiation budget, and climate. Ph.D. Dissertation, Colorado State University, Fort Collins, CO.

Ellis, J.S., T.H. Vonder Haar, S. Levitus, and A.H. Oort, 1977: The annual variation in the global heat balance of the earth. Submitted to *J. Geophys. Res.*

Hillger, D.W. and T.H. Vonder Haar, 1977: Deriving mesoscale temperature and moisture fields from satellite radiance measurements over the United States. *J. Appl. Meteorol.*, *16*, 715-726.

Kidder, S.Q. and T.H. Vonder Haar, 1977: Seasonal oceanic precipitation frequencies from Nimbus 5 microwave data. *J. Geophys Res.*, *82*, 2083-2068.

Kidder, S.Q., W.M. Gray and T.H. Vonder Haar, 1977: Satellite-derived temperature structure of tropical cyclones. Postprints, Eleventh Technical Conference on Hurricanes and Tropical Meteorology of the AMS, Dec. 13-16, 1977, Miami.

Oort, A.H. and T.H. Vonder Haar, 1976: On the observed annual cycle in the ocean-atmosphere heat balance over the northern hemisphere. *J. Phys. Oceanog.*, *6*, 781-800.

Vonder Haar, T.H. and J.S. Ellis, 1974: Atlas of radiation budget measurements from satellites (1962-1970). Colorado State University, Atmospheric Science Paper No. 231, Fort Collins, CO 80523.

APPENDIX A

Cumulative Summary of Papers and Publications
Sponsored by Grant NGR-06-002-102

PAPERS AND PUBLICATIONS SPONSORED BY GRANT NGR 06-002-102

Vonder Haar, T., E. Raschke, M. Pasternak and W. Bandeen, 1971: Global measurements of energy exchange between earth and space during the 1960's including latest results from the Nimbus-III satellite. Paper presented at the Annual Meeting of the AMS, San Francisco.

Raschke, E., T. Vonder Haar, W. Bandeen and M. Pasternak, 1971: The radiation balance of the earth-atmosphere system during June and July, 1969, from Nimbus-III radiation measurements, Space Research XI, Akademie-Verlag, pp. 661-667.

Vonder Haar, T., E. Raschke, M. Pasternak and W. Bandeen, 1971: Measurements of solar energy reflected by the earth and atmosphere from meteorological satellites. Invited paper presented at the International Solar Energy Society Conf., Greenbelt, MD. Solar Energy, 14, 2.

Raschke, E. and T. Vonder Haar, 1971: Climatological studies of the earth's radiation budget and its variability with measurements of the satellite Nimbus-III. Presented at the Symposium on Physical and Dynamical Climatology, Leningrad.

Vonder Haar, T., 1971: Global radiation budget and cloud cover by satellite measurements. Presented at the Remote Sensing Workshop, Miami.

Vonder Haar, T., E. Raschke, M. Pasternak and W. Bandeen, 1972: The radiation budget of the earth-atmosphere system as measured from the Nimbus-III satellite (1969-70). Presented at the XIV meeting of COSPAR, Seattle. Space Research XII.

Vonder Haar, T., and E. Raschke, 1972: Measurements of energy exchange between earth and space from satellites during the 1960's. Atmospheric Science Paper no. 184, Colorado State Univ., Ft. Collins.

Downey, P., S. Lassman and T. Vonder Haar, 1972: A study of extreme and persistent cloudiness based on satellite observations (1969-70). Tech. Report, Dept. of Atmos. Sci., Colorado State Univ., Ft. Collins.

Vonder Haar, T., 1972: Natural variation of the radiation budget of the earth-atmosphere system as measured from satellites. Paper presented at the Intern. Radia. Symp., Sendii, Japan, May. Also presented at the Conf. on Atmos. Rad., Sponsored by AMS, Colorado State Univ., August, Ft. Collins.

Korff, H. and T. Vonder Haar, 1972: The albedo of snow in relation to the sun position. Presented at the Conf. on Atmos. Rad., sponsored by AMS, Ft. Collins, August.

Raschke, E., T. VonderHaar, M. Pasternak and W. Bandeen, 1973: The radiation balance of the earth-atmosphere system from Nimbus-3 radiation measurements. NASA Tech. Note.

Downey, P., 1972: Distribution and parameterization of absorption of solar radiation in the atmosphere. M.S. thesis, Colorado State Univ., Ft. Collins.

Ellis, J., 1972: Interannual variations in the earth's radiative budget and the general circulation. M.S. thesis, Colorado State Univ., Ft. Collins.

Dittberner, G. and T. Vonder Haar, 1973: Large-scale precipitation estimated using satellite data; application to the Indian monsoon. *Archiv fur Meteor, Geophysik and Bioclimate.*, Ser. B, *21*.

Vonder Haar, T., 1973: Measurements of the planetary albedo from satellites. Presented at the Smithsonian Symp. on Solar Radiation Meas. and Instrumentation. Rockville, MD., November.

Vonder Haar, T., 1973: Global heat balance. Presented to the Joint Session of Radiometry and Photometry and Atmospheric Optics Tech. Groups, 1973 meeting of the Optical Society of America, Denver, CO.

Vonder Haar, T., 1973: Measurement of albedo over polar snow and ice fields using Nimbus 3 satellite data. Presented at the Interdisciplinary Symposium on the Study of Snow and Ice Resources, Monterey, CA.

Vonder Haar, T., 1973: Satellite observations of the earth's energy budget. Presented at the 1973 National Center for Atmospheric Research Summer Climate Meeting, Boulder, CO.

Vonder Haar, T. and A. Oort, 1973: New estimate of annual poleward energy transport by northern hemisphere oceans. *J. Phys. Ocean.*, *3*, 169-172.

Raschke, E., T. Vonder Haar, W. Bandeen and M. Pasternak, 1973: The annual radiation balance of the earth-atmosphere system during 1969-70 from Nimbus 3 measurements. *J. Atmos. Sci.*, *30*, 3, 341-346.

Vonder Haar, T. and J. Ellis, 1974: Satellite measurements of the interannual variations of the equator-to-pole radiation gradient, the effect of clouds and the response of the large-scale circulation. Presented at the 1st IAMAP Special Assembly, Melbourne, Australia.

Vonder Haar, T. and J. Ellis, 1974: Atlas of radiation budget measurements from satellites (1962-70). Colorado State Univ. Atmos. Sci. Paper No. 231, Ft. Collins.

Ellis, J.S., 1975: Radiative properties of large scale cloudiness for climate models. Presented at the Second Conf. on Atmos. Radia. of the AMS, Arlington, VA., Oct.

Vonder Haar, T. and J. Ellis, 1975: Albedo of the cloud-free earth-atmosphere system. Presented at the Second Conf. on Atmos. Rad. of the AMS, Arlington, VA., Oct.

Kidder, S. and T. Vonder Haar, 1975: Day-night variation of oceanic precipitation frequency inferred from Nimbus 5 electrically scanning microwave radiometer data for December 1972 - February 1973. Presented at the Second Conf. on Atmos. Rad. of the AMS, Arlington, VA., Oct.

Vonder Haar, T. and J. Ellis, 1975: Satellite radiation budget data applied to climate studies. Presented at the Intern. Union of Geophysics and Geodesy Conf., Grenoble, Aug.

Ellis, J.S., and T.H. Vonder Haar, 1976a: Zonal average earth radiation budget measurements from satellites for climate studies. Colorado State Univ., Atmos. Sci. Paper No. 240, Ft. Collins.

Ellis, J.S., and T.H. Vonder Haar, 1976b: The annual cycle in planetary radiation exchange with space. Presented at the COSPAR Symposium C, 8-19 June, Philadelphia, PA.

Vonder Haar, T., A. Oort, J. Ellis and S. Levitus, 1976: Determination of the annual cycle of energy transport by northern hemisphere oceans with the aid of satellite radiation budget measurements. Presented at COSPAR Symposium C, 8-19 June, Philadelphia, PA.

Oort, A.H., and T.H. Vonder Haar, 1976: On the observed annual cycle in the ocean-atmosphere heat balance over the northern hemisphere. J. Phys. Oceanog., 6, 781-800.

Kidder, S.Q., 1976: Tropical oceanic precipitation frequencies from Nimbus-5 microwave data. Colorado State Univ., Atmos. Sci. Paper No. 248, Ft. Collins, CO.

Kidder, S.Q. and T.H. Vonder Haar, 1976: A comparison of satellite rainfall-estimation techniques over the GATE area. Presented at COSPAR Symposium C, 8-19 June, Philadelphia, PA.

Hillger, D.W., and T.H. Vonder Haar, 1976: Mesoscale temperature and moisture fields from satellite infrared soundings. Presented at COSPAR Symposium C, 8-19 June, Philadelphia, PA.

Campbell, G.G. and T.H. Vonder Haar: 1976: Spherical harmonic analysis of the earth radiation budget components and the storage of future climate data from satellites in this form. Presented at COSPAR Symposium C, Philadelphia, PA, 8-19 June.

Hillger, D.W. and T.H. Vonder Haar, 1976: Mesoscale temperature and moisture fields from satellite infrared soundings. Colorado State University, Atmospheric Science Paper No. 249, Ft. Collins, CO.

Hillger, D.W. and T.H. Vonder Haar, 1976: Mesoscale temperature and moisture fields from satellite infrared soundings. Presented at the Workshop on Satellite Soundings, White Sands Missile Range, NM, September.

Kidder, S.Q. and T.H. Vonder Haar, 1977: Seasonal oceanic precipitation frequencies from Nimbus-5 microwave data. J. Geophys. Res., 82, 2083-2086.

Ellis, J.S., T.H. Vonder Haar, S. Levitus, and A.H. Oort, 1977: The annual variation in the global heat balance of the earth. Submitted to J. Geophys. Res.

Hillger, D.W. and T.H. Vonder Haar, 1977: Deriving mesoscale temperature and moisture fields from satellite radiance measurements over the United States. J. Appl. Meteorol., 16, 715-726.

Kidder, S.Q., W. M. Gray and T.H. Vonder Haar, 1977: Satellite-derived temperature structure of tropical cyclones. Postprints, Eleventh Technical Conference on Hurricanes and Tropical Meteorology of the AMS, Dec. 13-16, 1977, Miami.

APPENDIX B

Papers and Publications Produced During the Annual Period 1 November 1976 - 31 October 1977

Reprinted from JOURNAL OF APPLIED METEOROLOGY, Vol. 16, No. 7, July 1977
American Meteorological Society
Printed in U. S. A.

Deriving Mesoscale Temperature and Moisture Fields from Satellite Radiance Measurements over the United States

DONALD W. HILLGER AND THOMAS H. VONDER HAAR

Department of Atmospheric Science, Colorado State University, Fort Collins 80523

(Manuscript received 31 January 1977, in revised form 14 May 1977)

ABSTRACT

The ability to provide mesoscale temperature and moisture fields from operational satellite infrared sounding radiances over the United States is explored. High-resolution sounding information for mesoscale analysis and forecasting is shown to be obtainable in mostly clear areas. An iterative retrieval algorithm applied to NOAA-VTPR radiances uses a mean radiosonde sounding as a best initial guess profile. Temperature soundings are then retrieved at a horizontal resolution of $\sim$70 km, as is an indication of the precipitable water content of the vertical sounding columns. Derived temperature values may be biased in general by the initial guess sounding, or in certain areas by the cloud correction technique, but the resulting relative temperature changes across the field when not contaminated by clouds will be useful for mesoscale forecasting and models. The derived moisture, however, since affected only by high clouds, proves to be reliable to within 0.5 cm of precipitable water and contains valuable horizontal information. Present day applications from polar orbiting satellites as well as possibilities from upcoming temperature and moisture sounders on geostationary satellites are noted.

1. Introduction

High-horizontal-resolution temperature and moisture sounding information has become increasingly necessary for mesoscale research and applications. Both mesoscale forecasting and computer models require a large mass of input data on temperature and moisture. Only recently has this data become available from high resolution sounders such as the Vertical Temperature Profile Radiometer (VTPR) on NOAA operational satellites. However, the calibrated radiances are not used operationally to produce temperature profiles over the land masses, but only over data-sparse regions of the oceans where conventional soundings are not available. The method outlined here shows how the same VTPR radiances can be applied to mesoscale weather situations such as those over the Great Plains of the United States. Potentially, a sounding can be available at every VTPR scan spot at $\sim$70 km resolution, if clouds do not prohibit obtaining a sounding to the earth's surface. This is a great increase in resolution from normal operational radiosonde soundings which are spaced approximately every 400 km in the western United States. In the operational retrieval of soundings over the oceans many adjacent scan spots of the VTPR are used in order to compensate for cloud-contaminated fields of view and to provide the best sounding without need for a "best" first guess profile. However, a single-field-of-view temperature retrieval algorithm, based on a best initial guess profile, is used here to obtain soundings at much higher resolution.

An important aspect is that a concurrent radiosonde sounding is used for the first guess. This is possible, in general, only over land, not over the oceans. Fritz (1977) has independently approached this method, which he terms the "adjustment method." For an excellent synopsis of the impact of satellite temperature soundings over oceans on large-scale weather forecasts, the reader is referred to Phillips (1976). A similar study of the impact of satellite data on mesoscale forecasts over land is in order and follows from the present study. At present, satellite soundings are available at 6–12 h intervals from the sun-synchronous NOAA and DMSP (Air Force) satellites. However, in 1980, temperature and moisture soundings of much higher frequency (i.e., 30 min to 3 h) will be available over the United States from the geostationary satellites (Suomi *et al.*, 1971).

Recent work has shown that mesoscale temperatures can be derived even in partly cloudy conditions (Hillger and Vonder Haar, 1976a,b). A cloud-correction technique based on a single field of view is able to provide suitable above-cloud soundings in some completely and partly cloudy situations. The technique proves to be too simple in complex cloud situations, and temperatures derived in cloud areas may remain cloud-contaminated. Cloud problem areas are pointed out and should be used with caution. Even if clouds do significantly interfere with remote soundings, the use of high-resolution radiances does increase the possibility of sensing between clouds to obtain clear atmospheric temperatures. However, besides obtaining temperatures, mesoscale precipitable water (PW) fields are also realizable by eliminating temperature effects on the VTPR H_2O sounding channel. An application of these techniques is shown to provide mesoscale temperature and total precipitable water fields for 24 April 1975, a case study day for NASA's Atmospheric Variability Experiment (AVE) No. IV. (Hill and Turner, 1977).

2. Retrieval algorithm for NOAA VTPR applied to the mesoscale

The retrieval algorithm is based on a modified iterative type solution developed by Duncan (1974). To obtain the temperature profile of the atmosphere, one must find a solution $T(x)$ which satisfies the radiative transfer equation

$$N(\nu_i)=B[\nu_i,T(x_0)]\tau(\nu_i,x_0)+\int_{x_0}^{0} B[\nu_i,T(x)]\frac{\partial\tau(\nu_i,x)}{\partial x}dx \quad (1)$$

for each of the observed outgoing radiances $N(\nu_i)$ sensed by the satellite. The observed radiances are a product of the blackbody radiances B and the atmospheric transmittances $\tau(\nu_i,x)$ integrated from the surface, or cloud top, x_0 to the satellite along some vertical coordinate x. The blackbody radiances B are related directly to the temperature profile $T(x)$ and channel wavenumber ν_i by the Planck equation

$$B[\nu_i,T(x)]=\frac{C_1\nu_i^3}{\exp[C_2\nu_i/T(x)]-1}, \quad (2)$$

where C_1 and C_2 are known constants. Chahine (1968, 1970) applied the relaxation equation

$$B^{(n+1)}[\nu_i,T(x)]=\frac{\hat{N}(\nu_i)}{N^{(n)}(\nu_i)}B^{(n)}[\nu_i,T(x)] \quad (3)$$

to the radiative transfer equation to obtain an iterative solution for temperatures $T(x)$ at certain levels x, where the number of levels was equal to the number $\hat{N}$ of observed radiances. The observed radiances are thus used to fit the blackbody radiances B for each channel ν_i in successive iterations n, until the residuals between observed and calculated radiances

$$D_i^{(n)}=\hat{N}(\nu_i)-N^{(n)}(\nu_i) \quad (4)$$

for each channel reach an acceptable limiting value, usually the instrumental noise level.

This radiative transfer equation assumes a nonscattering atmosphere in local thermodynamic equilibrium. The dependence of the transmittances on changes in temperature is small compared to that of the Planck function so that the transmittances are calculated once before the first iteration to account for larger differences in initial guess temperature profiles.

Smith (1970) applied a relaxation formula based on radiance differences

$$B^{(n+1)}[\nu_i,T(x)]=[\hat{N}(\nu_i)-N^{(n)}(\nu_i)]+B^{(n)}[\nu_i,T(x)] \quad (5)$$

rather than radiance ratios. However instead of obtaining a solution at only specified levels x, independent estimates of the temperature profile $T(x)$ can be obtained for each channel ν_i through the Planck blackbody equation. The weights

$$W(\nu_i,x)=\partial\tau(\nu_i,x) \quad \text{for} \quad x\neq x_0$$
$$W(\nu_i,x_0)=\tau(\nu_i,x_0) \quad \text{for} \quad x=x_0$$

or derivatives of the transmittance are then used to compute a weighted average temperature $T(x)$ at each level x, i.e.,

$$T^{(n+1)}(x)=\frac{\sum_{i=1}^{6} T^{(n+1)}(\nu_i,x)W(\nu_i,x)}{\sum_{i=1}^{6} W(\nu_i,x)}. \quad (6)$$

In this case the six VTPR CO_2 channels are used to derive the entire temperature profile $T(x)$.

Smith *et al.* (1972) also used as his vertical coordinate $x=p^{2/7}$ divided into 100 equal levels in x from 0.01 mb to 1000 mb. This allows a temperature profile to be obtained which is not restricted to six atmospheric levels where the weighting functions are maximum. This method does not increase the information content of the radiances, but effectively allows a temperature determination at any desired level.

Duncan applied Chahine's relaxation formula (3) to Smith's independent temperature determinations in his retrieval algorithm. This is basically the same algorithm used in this study with modifications for input of any temperature profile as an initial guess sounding with an appropriate stratospheric profile above where the radiosonde sounding ends.

The VTPR instrument contains a water vapor and a window channel besides the six CO_2 channels as shown in Table 1 [for information on calculations of the transmittances see Weinreb and Neuendorffer (1973) and McMillin and Fleming (1970) for the H_2O and CO_2 transmittances, respectively]. The CO_2 transmittances are temperature-corrected by the initial guess profile using a second-degree polynomial representation according to the difference between the initial guess profile and a chosen standard atmosphere

TABLE 1. NOAA VTPR channels.

Channel number	Wavelength (μm)	Wavenumber (cm^{-1})	Approximate peak level of weighting function (mb)
CO_2 channels: 15 μm CO_2 absorption band			
1 (Q branch)	14.96	668.5	30
2	14.77	677.5	50
3	14.38	695.0	120
4	14.12	708.0	400
5	13.79	725.0	600
6	13.38	747.0	surface
H_2O channel: rotational water vapor absorption band			
7	18.69	535.0	600
Window channel: atmospheric window region			
8	11.97	833.0	surface

profile. Typical transmittances and weighting functions for the six CO_2 channels are shown in Figs. 1 and 2 for a U.S. standard atmosphere. The H_2O transmittances, however, are much more dependent on the initial guess profile than the CO_2 transmittances and are not shown here. Wark *et al.* (1974) have done some work with atmospheric water vapor which utilized the water vapor, window and lowest CO_2 channel. Other information on the VTPR instrument and the data archive format from which the data was obtained are explained in McMillin *et al.* (1973).

The retrieval of temperatures is a fairly straightforward process using the iterative method with up to 25 iterations for each profile to obtain a convergence noise level of less than 0.25 mW (m^2 sr cm^{-1})$^{-1}$ for each of the six VTPR CO_2 channels. This convergence value is considered to be a limitation due to instrumental noise, and the reason for the cutoff at 25 iterations is due to a decreasing improvement in the radiance residuals with successive iterations at the expense of computer time.

3. Initial guess profile

The retrieval program was modified to provide mesoscale temperatures from calibrated radiances from NOAA VTPR archive data tapes and a suitable initial guess profile which has close proximity in space and time to the desired soundings. By using radiosonde soundings to create an initial guess we hoped to obtain reasonable retrieved profiles, because an iterative program, such as the one used, provides best resultant temperatures with a "best initial guess profile." A best initial guess profile should also aid to the cloud correction used, which depends on a good initial guess profile, as will be explained later.

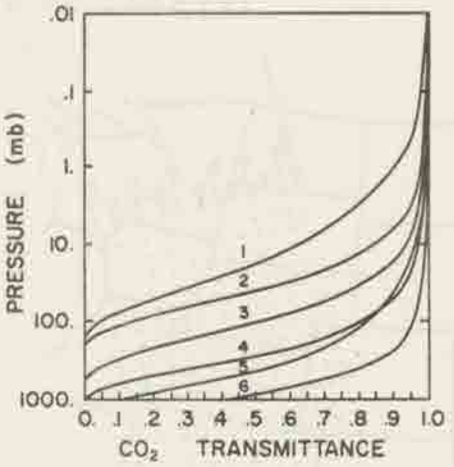

FIG. 1. VTPR CO_2 transmittances for U.S. Standard Atmosphere (Channels 1–6).

The idea of a best initial guess profile is one that will allow the retrieval of temperature profiles which are most near the actual atmospheric temperature structure at the time of observation by the satellite. Even on this AVE experiment day there is a discrepancy between the radiosonde launch times which are used to compute initial guess profiles and the satellite overpass time of at least 1 or 2 h. During this time, since it is early morning, there usually is a large change in surface conditions as the morning surface inversion is broken or lifted. Also, the moisture changes rapidly during this time as vertical mixing takes place. Horizontal distances across the desired field may also reveal different types of air masses with differing lapse rates and moisture contents.

Because of physical limitations, temperature retrieval methods lack the vertical resolution to change small vertical features below the resolution of the weighting functions. In spite of this an attempt is not made to find the best initial guess for each air mass, but to

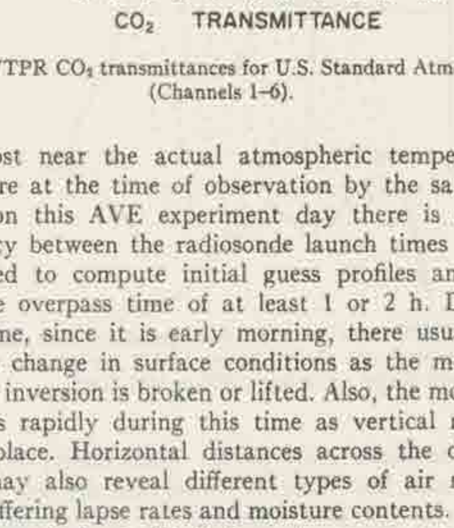

FIG. 2. As in Fig. 1 except for VTPR CO_2 weighting functions.

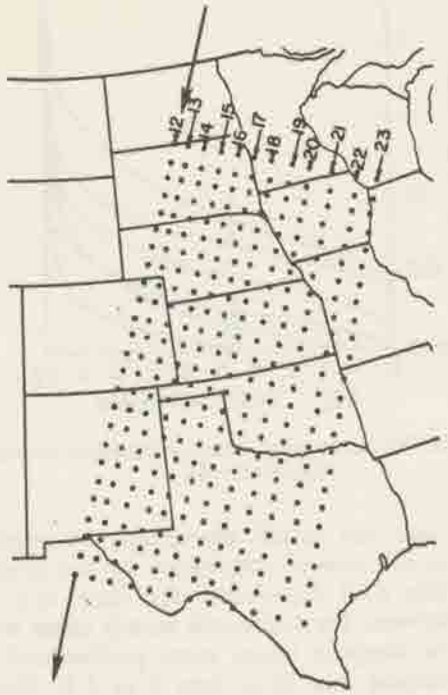

FIG. 3. VTPR scan coverage and resolution. Left half of several scan lines are shown (spots 12–23) for satellite pass over the Great Plains on 24 April 1975 at 1615 GMT.

provide one initial guess profile which should be applicable across the whole horizontal field desired. This may not be the best approach in many weather situations where air masses are widely different. However, by averaging a number of radiosonde soundings, features such as temperature inversions particular to individual radiosonde profiles should be smoothed out in the initial guess and features present across the whole field should be retained. Then, the same initial guess could be used to obtain the real or observed profile features through the iterations on the observed radiances without adding features particular to one radiosonde used as initial guess. Actually, Chahine (1968) proposed using an isothermal initial guess profile. However, in that case the transmittances would not be correctly initialized by the initial guess profile in terms of temperature lapse rates and total moisture content. A mean initial guess profile should then provide a best initial guess for the wide range of conditions on a certain day. Work is continuing on using two or more widely different initial guess profiles to try to optimize the desired effects of each profile.

The initial guess profiles used for 24 April 1975 were derived from special AVE radiosonde launches which provided soundings approximately every 3 h during the day. VTPR radiances were available at approximately 1615 GMT over the Great Plains from the morning or descending orbit of the NOAA 4 satellite. We used a space-averaged sounding derived from the radiosonde profiles as an initial guess profile for the area of the satellite pass shown in Fig. 3.

To obtain the space-averaged sounding required taking a set of radiosondes and weighting each one equally in an averaging program. All AVE radiosondes were given in 25 mb increments, so they were easily averaged. The main impact of this averaging was to smooth out small temperature inversions particular to specific areas and to make a mean mixing ratio profile which should be more moist than the driest sounding and drier than the most moist soundings. This average sounding is a rather smooth vertical profile and will not reproduce small temperature inversions when used as an initial guess in the retrieval algorithm. Also, since the mean moisture profile will be too dry in the moist air mass it will cause temperatures to be retrieved that are too cool in very low levels. Moisture makes the observed radiances low, therefore causing low retrieved temperatures near the H_2O weighting functions peak, usually at or below 700 mb. On the other hand, the mean profile will be too moist in the dry region causing higher temperatures than with a correct moisture profile. These temperature differences are being studied as another approach toward moisture determination using the CO_2 channels alone.

The initial guess profile that was used was obtained by averaging ten 1800 GMT radiosonde profiles from the AVE radiosonde network shown in Fig. 4. Likewise a 1500 GMT mean profile was also computed from all 10 radiosondes, but the 1800 GMT profile was chosen as an initial guess because of higher surface

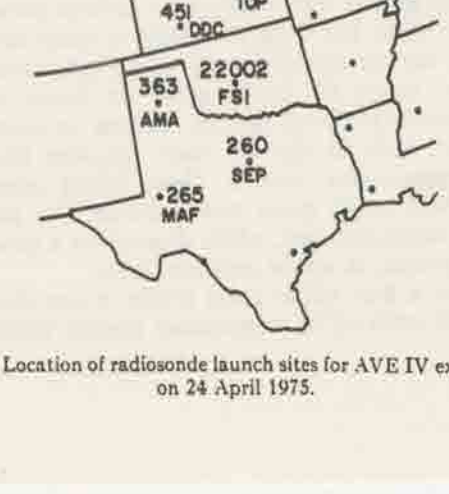

FIG. 4. Location of radiosonde launch sites for AVE IV experiment on 24 April 1975.

temperatures and lack of a surface temperature inversion. The difference between the two mean profiles was less than 1.0°C except below 850 mb where the temperature was 2.5°C larger at the surface in the 1800 mean profile than the 1500 mean. The main reason for choosing this profile was to aid the cloud correction technique explained below.

Another mean profile was also calculated at 1500 GMT. Besides the one containing all ten stations, a mean using only the six southern stations in Fig. 4 was also used as an initial guess in a small sample of 27 soundings scattered from north to south. The results of comparisons between temperature and moisture values using each mean profile as an initial guess are shown in Table 2. For case A with 10 and 6 profiles, respectively, in the mean, the main difference in the initial guess profiles was generally warmer temperatures by 2–3°C in the southern mean profile below 200 mb (tropopause) and cooler temperatures above the tropopause. This is caused by a higher tropopause in the southern mean. In spite of this difference, the derived profiles give 500 mb temperatures which are only 1.4°C warmer using the southern initial guess, whereas the initial guess difference was 2.6°C at 500 mb. The retrieved temperature profiles are affected by the initial guess, but a correlation of 0.95 between two samples of 500 mb temperatures for 27 profiles shows a high degree of reproducibility of the field structure in spite of two different initial guesses, even in cloudy cases included in the sample.

TABLE 2. Results of using different mean profiles as initial guess.

	Case	
	A*	B**
RMS difference between mean profiles for 38 levels (25 to 950 mb)	2.8°C	0.8°C
RMS difference between 500 mb temperatures derived using each initial guess profile for 27 sample profiles	1.4°C	0.7°C
Initial guess difference at 500 mb	(2.6°C)	(0.8°C)
Correlation coefficient for 500 mb temperatures from two samples	0.95	0.99
Total precipitable water (PW) (1) in each initial guess (2)	1.88 cm 1.96 cm	1.88 cm 1.87 cm
Correlation coefficient for PW values from two samples	0.99	0.99

* Case A. Comparison using mean profiles at 1500 GMT, one containing all ten radiosondes (1) and the other only the six southern radiosondes (2) in the mean.

** Case B. Comparison using mean profiles at 1500 GMT (1) and 1800 GMT (2), each containing all ten radiosondes in the mean.

The difference in initial guess total precipitable water for the two profiles was negligible and a correlation of 0.99 between the two data samples results in spite of the difference in temperature profiles for the two initial guesses.

Case B is a similar comparison between the two previously mentioned mean profiles created using all 10 profiles at 1500 and 1800 GMT, respectively. The difference in the initial guess profiles was smaller here and the correlation was higher for the two samples of 500 mb temperatures. These comparisons show that the obtained horizontal field structure is not highly dependent on the initial guesses tested here. Other initial guesses with different lapse rates and different moisture profiles should exhibit larger differences in the derived profiles.

4. Cloud correction technique

The cloud correction is a modification of a technique used by Shaw *et al.* (1970). The technique is not intended to be sophisticated, but to correct for cloudy situations which are most easily identifiable, single cloud layers. The cloud layer is assumed to be completely overcast, and if not overcast, a lower than actual cloud level will result. Although this cloud correction technique does not work well in many situations with small cloud amounts or high or multilevel clouds, it does eliminate problems with some cloudy fields of view, thereby producing more horizontally homogeneous temperatures compared to nearby non-cloudy columns at and slightly above the calculated cloud level than with no correction.

Basically the idea relies on a best initial guess profile and integrated radiances derived from it through the radiative transfer equation (1). These integrated radiances are then compared to observed radiances for three VTPR CO_2 channels whose weighting functions peak lowest in the atmosphere (channels 4, 5 and 6). If the rms residual between the observed and calculated radiances is large, then the observed radiances are probably cloud-contaminated and have low values. The hypothesized cloud level is then raised in increments and the radiances are again calculated and compared until the rms radiance residual reaches a minimum, meaning that the calculated radiances are now smaller than the observed radiances, or that an effective cloud-top level has been attained. Using the 1800 mean profile as an initial guess instead of the 1500 mean aided the cloud correction technique. The higher lapse rate near the surface at 1800 GMT made the determination of the effective cloud level easier. If a temperature inversion were present the rms radiance residual would reach a temporary minimum value at that level, falsely underestimating the cloud-caused minimum, which may be at a higher level.

The use of a best initial guess profile will also aid this method by producing calculated radiances nearly like those of the desired profile in a clear atmosphere.

A similar technique was used by Hodges (1976) in a cloud model in an attempt to also obtain cloud amount information. The technique used here will be valid only for overcast situations unless a fractional cloud cover is assumed. In this case, since 100% cloud cover is assumed, the cloud level will be at a minimum or lower height in order to make the rms radiance residual a minimum. Temperature soundings are then obtained above this effective cloud level through the iterative process previously outlined.

5. Integrated moisture values

To obtain precipitable water values a slightly more involved method was required. The idea was to compare observed H_2O channel (channel 7) radiances with radiances calculated using the radiative transfer equation on the derived temperature profiles with a known initial guess precipitable water amount. The comparison was done after the iterative process was used to obtain the temperature profiles in order to try to compensate for horizontal temperature changes in each scan spot across the derived field.

The H_2O channel radiance is strongly dependent on both total atmospheric moisture and temperature, but by reducing or eliminating the temperature effect on the H_2O radiance, the result should be correlated with conventional precipitable water values obtained at the standard radiosonde sites. The H_2O radiance residual, as it is called here, is a difference between the observed H_2O channel radiance and the calculated H_2O channel radiance using the iterated or derived temperature profile

$$H_2O\ \text{Residual} = N_{\text{obs}}(T_a, PW_a) - N_{\text{calc}}(T_i, PW_0) \qquad [H_2O\ \text{channel}]$$

where:

- T_a actual temperature profile
- PW_a actual precipitable water amount
- T_i iterated temperature profile
- PW_0 initial guess precipitable water amount ($\sim$2 cm for 24 April 1975 18 GMT mean initial guess sounding).

The initial guess precipitable water amount is a constant value which is not changed in the iterative process. Now, if the iterated temperature profile approximates the actual profile, i.e., $T_i \approx T_a$, then the difference between the calculated and observed radiances will be a function only of the difference between actual and initial guess precipitable water amounts:

$$\begin{aligned} H_2O\ \text{Residual} &\propto PW_a - PW_0 \\ &\propto PW_a. \end{aligned}$$

This radiance residual is, however, just proportional to the actual precipitable water amount PW_a since the initial guess moisture content PW_0 was constant throughout the iteration process for all derived profiles. The H_2O channel radiance is used solely for the determination of precipitable water amounts. A least-squares linear regression between this H_2O radiance residual and the precipitable water values at the radiosonde sites gives a high correlation, as will be shown.

Looking back at Table 2, we see in case A that the derived 500 mb temperatures using each initial guess profile had an rms difference of 1.4°C. Values for other lower levels tended to be larger where the initial guess profiles were most different. However, the derived precipitable water values were still highly correlated at 0.99. At least for the mean initial guess profiles used here, there appears to be little effect of the initial guess on the structure of the obtained total precipitable water values. Larger rms differences in initial guess profiles should again display correspondingly larger rms differences in the resultant derived temperature profiles, but only initial guess profiles with different vertical temperature structure should display a lower correlation in derived total moisture values. Again, work is expanding into the testing of different initial guess profiles to optimize the resultant horizontal structure of the moisture fields. A better feeling for errors in the moisture content can be seen by looking at the linear least-squares line fit shown with the precipitable water results.

6. 24 April 1975 results

The AVE experiment day, 24 April 1975, proved to be quite interesting and also provide radiosonde soundings at time periods near the satellite overpass at 1615 GMT. The surface weather observations for 1600 are plotted using the standard station model in Fig. 5 for the most interesting area centered in Oklahoma. The surface dry tongue extending through the panhandle of Texas into Oklahoma presents a strong moisture gradient along the dry line to its south. The most important features in this figure are the observed cloud cover shown in the stippled regions and the isopleths of surface dew point temperature. These isodrosotherms will later be shown to be reproduced quite well by the integrated moisture values obtained from the VTPR H_2O channel.

Fig. 6 shows the Synchronous Meteorological Satellite (SMS) visible image for this case study day at 1600 GMT. Northern Texas and most of Oklahoma are clear. Cloud cover is extensive in Kansas, and partly cloudy conditions in southern Texas will be shown below to affect the derived temperatures there.

7. Derived 500 mb temperatures on the mesoscale

Temperatures obtained through iterations on the mean initial guess profile were plotted according to their calculated horizontal positions for certain pressure

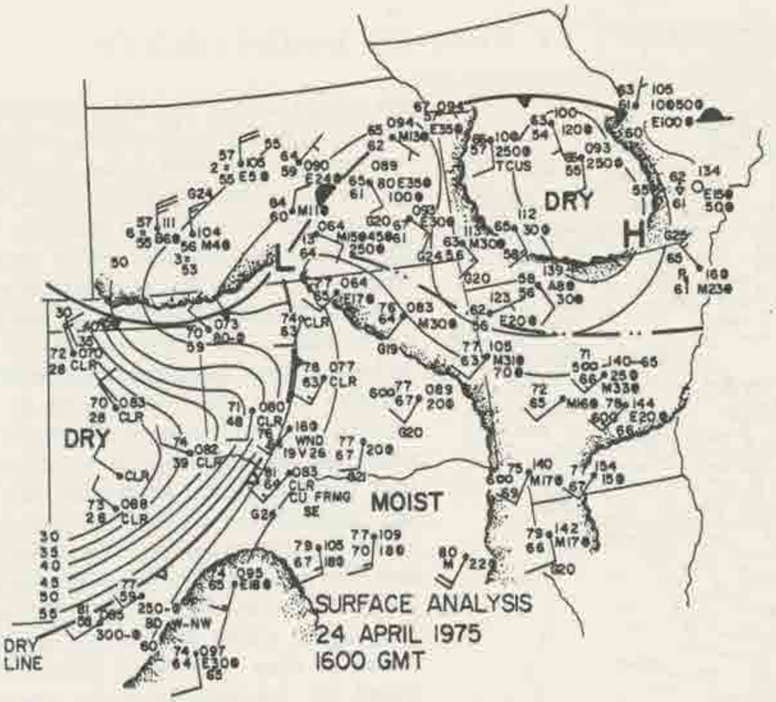

FIG. 5. Surface observations plotted according to standard station model. Isopleths of dew point temperature are analyzed and stippled regions indicate clouds.

levels and analyzed. An earth location algorithm involving spherical geometry was used to calculate individual scan spot positions from satellite orbit parameters. The 500 mb temperatures are characteristic of the mesoscale temperature fields which satellite sounders are capable of producing. Higher tropospheric levels contain less temperature variation, and lower levels are plagued both by clouds and the unchanging initial guess moisture profile used. Since temperature profiles were derived only above the calculated cloud level, the 700 mb temperatures, for example, were unobtainable in many cloudy columns. The 700 mb temperatures were also too high in the dry tongue area due to the effect of the dry atmosphere on the VTPR CO_2 channels with lowest weighting function peaks. The dryness, as explained earlier, causes observed radiances to be high and therefore causes temperatures derived from these observed radiances to be high when the moisture content is kept constant in the iteration process.

Fig. 7 shows the derived 500 mb temperatures at 1615 GMT. The contours were analyzed from about 200 temperature soundings obtained at almost every scan spot of the VTPR instrument over this region. The initial guess 500 mb temperature was about −15°C, corresponding to a mean temperature on the Kansas-Oklahoma border at this level. The individually derived temperature values at 500 mb are shown to indicate data coverage and resolution and to give a feel for the random noise in the temperatures.

The 500 mb temperature analyses obtained from the radiosonde soundings alone are shown in Figs. 8 and 9. The first figure contains the 500 mb temperatures from AVE radiosonde launches at a time period before the satellite pass at 1500 GMT and the second contains the radiosonde launches for the period 3 h later (1800 GMT) after the satellite pass. Both figures are fairly consistent with only a slight warming in the 1800 GMT 500 mb temperatures and a slight shift of the cold trough axis to the east.

When compared to the radiosonde analyses, the

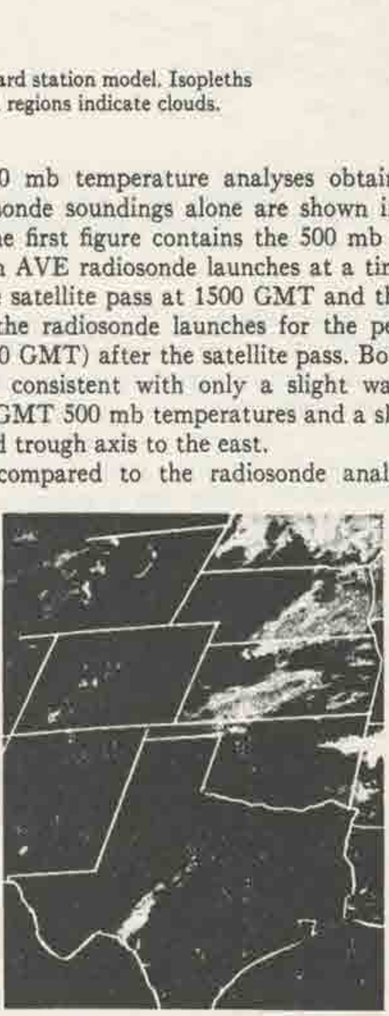

FIG. 6. SMS visible image for 24 April 1975 at 1600 GMT.

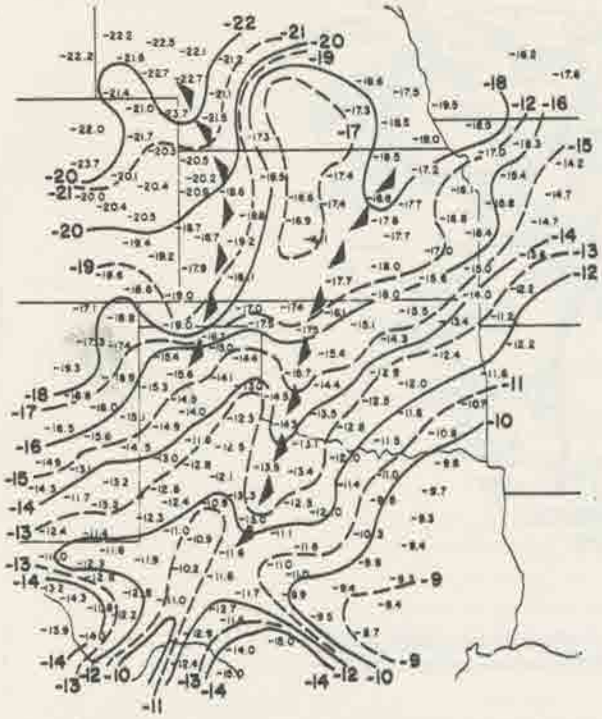

FIG. 7. Satellite-derived 500 mb temperature field obtained using an iterative retrieval algorithm with a mean radiosonde sounding as initial guess profile. Numbers at scan spot positions indicate data coverage and resolution.

satellite-derived temperatures in Fig. 7 appear in general to be biased too low by about 1–2°C. This is probably due to the vertical structure or magnitude of the mean initial guess temperature profile used, or to the transmittances which are corrected for temperature and moisture by the initial guess profile. The initial guess temperature profile has a strong compounding influence since it is used both as an initial guess and to calibrate the transmittances. (Associating the bias to the initial guess profiles also assumes that the observed radiances are calibrated correctly.) Using the mean profile created from the six southern stations at 1500 or 1800 GMT instead of for all ten stations should have raised the derived temperatures at 500 mb and reduced the bias in the analyzed field. However, the absolute values are not as important as the relative temperature changes, especially the horizontal temperature structure at the mesoscale. Absolute temperature values are not needed to determine significant horizontal changes across the temperature field. The cold trough axis does appear in central Oklahoma about where it is also shown in the radiosonde analyses. Any difference in the actual axis location between the two data sets is probably due to the difference in horizontal resolution capabilities of the two data sets. Since the satellite-derived temperatures are more densely spaced by a factor of about 36, the trough axis is probably more correctly placed by this much denser satellite data network.

Two main problem areas caused by clouds exist in this particular 500 mb analysis. The low temperature regions of −14°C in southern Texas are caused by cloud contamination which was not sufficiently dealt with by the simple cloud corrections technique. These scan spots contain small cloud amounts which are handled least effectively by the cloud correction technique when complete cloud cover is assumed. The effective cloud level was placed at too low a level, causing derived temperature to be low by 3–4°C above the assumed cloud level. However, by knowing that these cases are biased too low by clouds they can hopefully be eliminated. Also in Kansas where clouds do become thicker, the ability to obtain soundings does decrease. The horizontal resolution capability is reduced by clouds extending up to and above 500 mb. Here again, where the 500 mb temperatures are obtained in cases with small cloud amounts, they are biased too low because of the assumed 100% cloud amount in only slightly cloudy columns. The position of the effective cloud level is critical to the cloud correction technique used here, and the effect of clouds

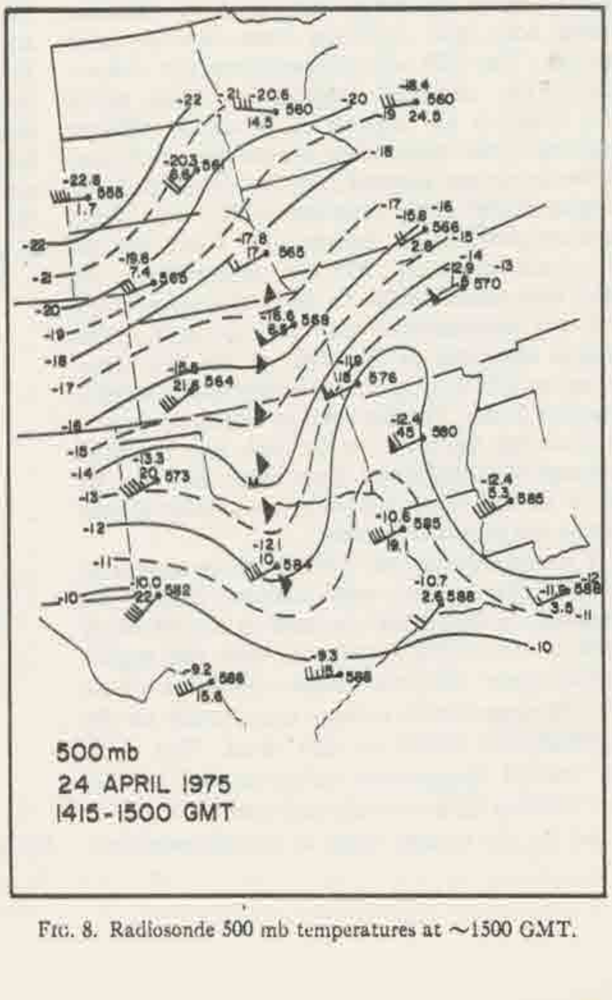

FIG. 8. Radiosonde 500 mb temperatures at ~1500 GMT.

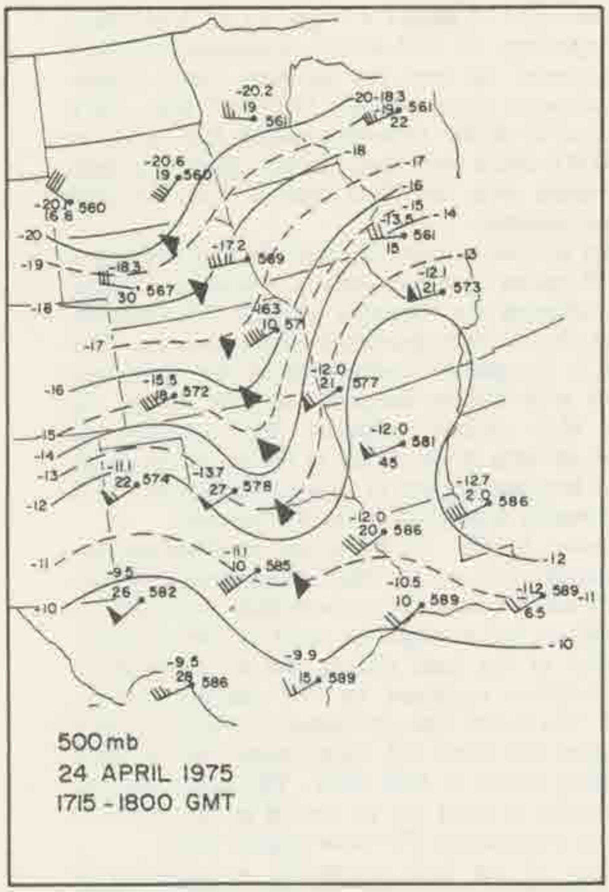

FIG. 9. Radiosonde 500 mb temperatures at ~1800 GMT.

can be summed up as mainly increasing the variability of temperatures derived under cloudy situations.

An example of the effect of small cloud amounts is the region in southeastern Colorado and western Kansas where the isotherms are bent towards lower temperatures. This feature does not show up in the radiosonde analyses alone and is associated with the small cloud amounts there. Other temperature features which occur in clear areas are associated with the observed radiances and not the cloud correction technique. Also, multi-level and high-cloud situations, such as in central Nebraska and Kansas, lead to temperatures which are too warm. The simple cloud correction should not be expected to work in such complex cloud situations.

These two problem areas show the need for an assumed cloud amount parameter in this simple cloud-corrections technique, especially small cloud amount cases. In cases with small cloud amounts, the effective cloud level is much lower than the actual partial cloud level. This causes temperatures above this effective cloud level to be biased too low due to an isothermal temperature tendency of the derived profiles below the cloud level when no cloud is assumed (Chahine, 1970). The derived temperatures below the actual cloud level tend toward the cloud top temperature when the observed radiances originate from a completely overcast column.

The idea behind using this cloud correction technique was to try to obtain more horizontal temperature resolution in cases where the vertical column was not completely clear. Over half of the derived temperatures were obtained from completely clear columns, but a certain amount of horizontal resolution would have been lost by throwing out all cloudy columns. Rather, the cloud correction was applied and its effects on derived temperatures are pointed out to show that it is least effective in cases with small but detectable cloud amounts and in high or multi-level cloud situations. So, unless the cloud situation is known, this simple cloud correction technique provides little extra value to the clear soundings alone. For this reason, an independent visible or infrared channel, from which cloud amount information can be extracted, should be available along with the satellite sounding radiances. Such information will be available from the new generation of sounding instruments to be launched on the operational NOAA satellites in the 1980's.

8. Precipitable water field on the mesoscale

Perhaps the most interesting and useful analysis obtained is the precipitable water (PW) analysis in

FIG. 10. Satellite-derived precipitable water field obtained using a least-squares linear regression of radiosonde total precipitable water values against H_2O radiance residuals. Numbers indicate data coverage and resolution.

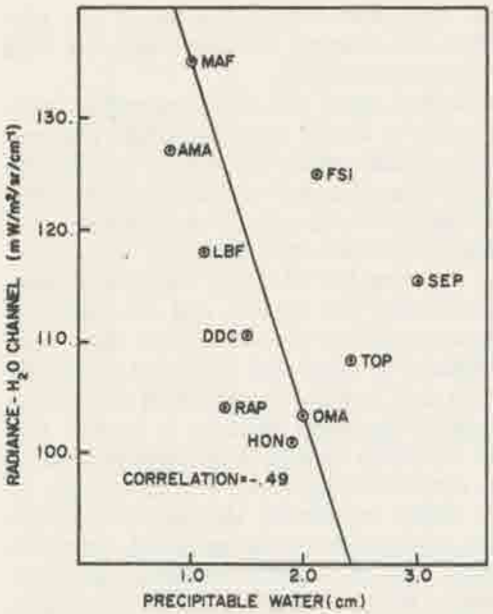

FIG. 11. H_2O channel radiances plotted against time-interpolated precipitable water values at radiosonde sites in the study area.

Fig. 10. The procedure explained earlier was used to try to eliminate the temperature effect on the VTPR H_2O channel by using the derived temperature profiles to obtain calculated radiances. If the derived temperatures are reasonably accurate then differences between observed and calculated radiances would be due to moisture effects only. This is shown graphically in Figs. 11 and 12, where H_2O channel radiances and H_2O channel radiance residuals are plotted against time-interpolated PW values at the AVE radiosonde sites. In order to obtain a larger set of data points for comparison, the field of derived satellite soundings was extended up into the northern Great Plains. PW values at approximately 1500 and 1800 GMT were used to obtain time-interpolated PW values at 1615 GMT which were then plotted against the radiance values from the H_2O channel and the H_2O radiance residuals.

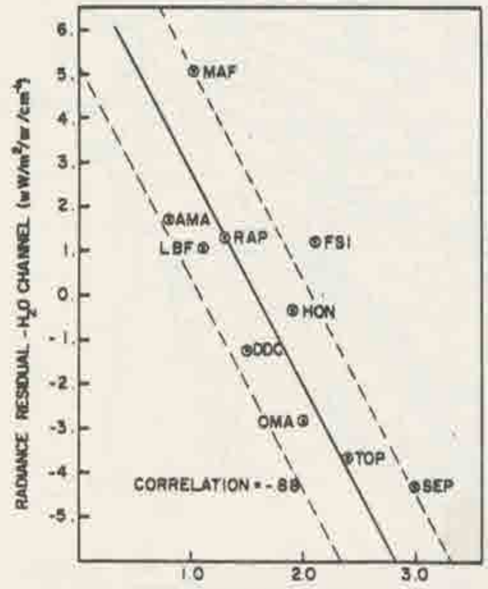

FIG. 12. As in Fig. 11 except for H_2O radiance residuals.

When plotted against the H_2O channel radiances, the PW values produced only a −0.49 correlation. Large radiances are correlated with low PW amounts, but are also strongly dependent on temperature. This is seen in the general arrangement of the radiosonde stations with highest temperatures also having the largest H_2O channel radiances. The southern, or warmer, stations in Fig. 11 are in the top of the graph and the least-squares line fit shows a steep slope which is only weakly dependent on the PW amount.

However, in Fig. 12, by trying to eliminate the temperature effect on the H_2O channel radiance, the stations are not arranged preferentially according to temperature, but arranged in terms of PW amounts. The slope of the least squares line fit shows much more variation explained by PW changes than in Fig. 11. The rather high correlation of −0.88 excludes the station FSI (Fort Sill, Okla.) which did not have a sounding launch at 1500 GMT. This point was not used because it could not be treated as the others to obtain an interpolated PW value at 1615 GMT.

Because of the high correlation, a least-squares linear regression was used to calculate coefficients to convert H_2O radiance residuals directly into the PW values plotted in Fig. 10. The scatter of time-interpolated PW values about the regression line, except for FSI, is less than 0.5 cm of H_2O which can be considered a maximum error level for this data set. Dashed lines at ±0.5 cm from the line fit encompass all values except for FSI.

The only high-resolution data set to compare with these PW values are the surface observations in Fig. 5. The surface dry tongue through Texas into Oklahoma is shown in the satellite derived field by a large change in PW values from less than 0.5 cm in western Texas to over 2.5 cm of H_2O in eastern Texas. The surface dry line oriented southwest to northeast is designated by a strong PW gradient of about 1 cm of H_2O per 70 km, the linear distance between scan spot centers.

The moist areas in eastern Texas and western Kansas in the surface observations contain over 2.5 cm of PW. However, the dry region in central Kansas of less than 1.5 cm of PW is caused by cloud contamination up to and above the 500 mb level. In this case the radiances are integrated from vertical columns truncated by the high cloud levels. As expected, this causes the radiance residuals to be low because of the decreased difference between observed and calculated radiances which arises mainly from H_2O differences in the low levels. Clouds do, therefore, cause some contamination of these data but the PW values seem to be mostly unaffected unless cloud levels are high. In southern Texas where lower clouds caused 500 mb temperatures to be low, the PW values seem to be unaffected compared to neighboring scan spots. High PW values here agree with small dew point depression values in the surface observations.

These two data sets (Figs. 5 and 10) should not be correlated exactly since one is for surface values and the other for integrated moisture. However, since moisture in the atmosphere is concentrated near the surface, there should be some indication of PW amounts in the surface dew point temperatures (Smith, 1966). Differences in the two moisture analyses should yield an indication of vertical mixing of moisture provided the data sets were obtained at the same time. High surface dew point temperatures and low PW values would indicate little vertical mixing, whereas higher PW values with the same surface moisture would indicate more vertical mixing.

Moisture features such as the indicated dry line feature or moisture gradient in the derived PW values are extremely important to forecasting convective storm development. The horizontal position of the dry line usually determines a line along which the most severe storms occur. The dry line feature and vertical moisture mixing information together could help pinpoint subsequent convective development later in the day.

9. Conclusions

High-resolution temperature and moisture information is necessary for mesoscale weather analysis and forecasting. The ability to provide such mesoscale information is shown to be feasible now, from existing operational satellite sounding radiances over the United States. Even though the derived temperature values are biased by cloud contamination in certain areas, they do show significant relative horizontal changes in non-cloudy areas, which for example can better locate cold trough positions.

Precipitable water information is probably the most needed information on the mesoscale. Moisture varies more rapidly in space and time than temperature at smaller scales. Precipitable water values derived from the NOAA VTPR H_2O channel, when corrected for temperature effects, provide a reliable source of horizontal moisture information. Cloud contamination which lowers temperature values does not significantly affect the derived integrated moisture amounts beyond the maximum noise level of 0.5 cm of H_2O except in high cloud cases.

An important aspect of the present study, in contrast to earlier large-scale temperature soundings from satellites over the oceans, is the use of concurrent satellite and radiosonde data in a joint analysis. The more widely spaced radiosondes, with their good vertical resolution, may be considered the trunks of the data set; the higher horizontal resolution satellite data (the branches) are coupled to and dependent upon the trunks. No attempt has yet been made of optimum analysis and assimilation of the data sets. That study, as well as preparation to add the fourth dimension (time) from upcoming high-frequency geostationary satellite sounders will be the subject of considerable future research. If information on temperature and moisture does become routinely available from satellite soundings for mesoscale analysis and forecasting, it will provide a valuable additional tool to conventional radiosonde sounding information alone.

Acknowledgments. Special thanks go to Robert Maddox of the APCL/NOAA labs in Boulder for analyzing the surface and 500 mb maps used for this case study day. Dr. L. Duncan at the U.S. Army White Sands Missile Range provided help in initiating the iterative temperature retrieval program, and additional technical assistance and data were obtained from the Indirect Soundings Branch of NOAA/NESS.

Funding for this research was received from NASA, Contract NGR-06-002-102, and the Bureau of Reclamation, Contract 6-07-DR-20020.

REFERENCES

Chahine, M. T., 1968: Determination of the temperature profile in an atmosphere from its outgoing radiance. *J. Opt. Soc. Amer.*, **58**, 1634–1637.

——, 1970: Inverse problems in radiative transfer: Determination of atmospheric parameters. *J. Atmos. Sci.*, **27**, 960–967

Duncan, Louis D., 1974: An iterative inversion of the radiative transfer equation for temperature profiles. R & D Tech. Rep. ECOM-5534, Atmos. Sci. Lab., White Sands Missile Range, New Mexico, 18 pp. [NTIS Ref. AD-776 899/7GI].

Fritz, Sigmund, 1977: Temperature retrievals from satellite radiance measurements—an empirical method. *J. Appl. Meteor.*, **16**, 172–176.

Hill, Kelly, and Robert E. Turner, 1977: NASA's atmospheric variability experiments (AVE). *Bull. Amer. Meteor. Soc.*, **58**, 170–172.

Hillger, Donald W., and Thomas H. Vonder Haar, 1976a: Mesoscale temperature and moisture fields from satellite infrared soundings. Atmos. Sci. Pap. No. 249, Colorado State University [NTIS Ref. number applied for].

——, and ——, 1976b: Mesoscale temperature and moisture fields from satellite infrared soundings. *Proc. Meteorological Observations from Space: Their Contribution to the First GARP Global Experiment*, COSPAR, Philadelphia, June, 59–63 [NTIS Ref. PB 262 530/AS].

Hodges, Donald B., 1976: A single field of view method for retrieving tropospheric temperature profiles from cloud-contaminated radiance data. NASA Contractor Report, NASA CR-2726, 90 pp. [NTIS Ref. N76-29861/1GI].

McMillin, L. M., D. Q. Wark, J. M. Siomkajlo, P. G. Abel, A. Werbowetzki, L. A. Lauritson, J. A. Pritchard, D. S. Crosby, H. M. Woolf, R. C. Luebbe, M. P. Weinreb, H. E. Fleming, F. E. Bittner and C. M. Hayden, 1973: Satellite infrared soundings from NOAA spacecraft. NOAA Tech. Rep. NESS 65, 112 pp. [NTIS Ref. COM-73-50936/6AS].

——, and H. E. Fleming, 1976: Atmospheric transmittance of an absorbing gas: A computationally fast and accurate transmittance model for the absorbing gases with constant mixing ratios in inhomogeneous atmosphere. *Appl. Opt.*, **15**, 358–363.

Phillips, Norman A., 1976: The impact of synoptic observing and analysis systems on flow pattern forecasts. *Bull. Amer. Meteor. Soc.*, **57**, 1225–1240.

Shaw, J. H., M. T. Chahine, C. B. Farmer, L. D. Kaplan, R. A. McClatchey and P. W. Schaper, 1970: Atmospheric and surface properties from spectral radiance observations in the 4.3 micron region. *J. Atmos. Sci.*, **27**, 773–780.

Smith, W. L., 1966: Note on the relationship between total precipitable water and surface dew point. *J. Appl. Meteor.*, **5**, 726–727.

——, 1970: Iterative solution of the radiative transfer equation for the temperature and absorbing gas profile of an atmosphere. *Appl. Opt.*, **9**, 1993–1999.

——, H. M. Woolf and H. E. Fleming, 1972: Retrieval of atmospheric temperature profiles from satellite measurements for dynamical forecasting. *J. Appl. Meteor.*, **11**, 113–122.

Suomi, V., T. Vonder Haar, R. Kraus and A. Stam, 1971: Possibilities for sounding the atmosphere from a geosynchronous spacecraft. *Space Research XI*, Academie-Verlag, 609–617.

Wark, D. Q., J. H. Lienesch and M. P. Weinreb, 1974: Satellite observations of atmospheric water vapor. *Appl. Opt.*, **13**, 507–511.

Weinreb, M. P., and A. C. Neuendorffer, 1973: Method to apply homogeneous-path transmittance models to inhomogeneous atmospheres. *J. Atmos. Sci.*, **30**, 662–666.

VOL. 82, NO. 15 JOURNAL OF GEOPHYSICAL RESEARCH MAY 20, 1977

Seasonal Oceanic Precipitation Frequencies From Nimbus 5 Microwave Data

STANLEY Q. KIDDER AND THOMAS H. VONDER HAAR

Department of Atmospheric Science, Colorado State University, Fort Collins, Colorado 80523

Microwave brightness temperature data from the Nimbus 5 satellite have been analyzed by using threshold brightness temperatures to yield tropical oceanic precipitation frequencies for several classes of rainfall rates during the season December 1972 through February 1973. Data taken near local noon and near local midnight were analyzed. The overall results are consistent with both climatological precipitation frequency and with concurrent satellite-derived frequency of highly reflective clouds. The difference between the local noon and the local midnight frequency is small, but the heavier rainfall rates tend to occur more frequently near local noon. The ratios of the frequencies of light, moderate, and heavy rain were observed to be relatively constant over the tropical oceans. Passive microwave measurements from space seem to be an important step toward accurate measurement of oceanic precipitation.

INTRODUCTION

Knowledge of oceanic precipitation is of fundamental importance to meteorology. Approximately 80% of the earth's precipitation falls in the ocean [*Sellers*, 1965], where fewer than 10% of the world's weather stations exist. Yet latent heat released over the ocean plays a major role in the maintenance of the general circulation and affects almost everything known as 'weather.'

Many ingenious attempts to determine oceanic precipitation from surface observations have been made [e.g., *McDonald*, 1938; *Tucker*, 1961; *Jacobs*, 1968; *Allison et al.*, 1969], but such observations have not the spatial nor temporal resolution necessary for accurate measurement of anything except long-term climatological precipitation. Satellite data offer much better resolution, but until the launch of Cosmos 243 in 1968 and Nimbus 5 in 1972, all satellite data were from the visible or infrared portions of the electromagnetic spectrum in which precipitation cannot be observed directly because of the opacity of clouds. (See *Martin and Scherer* [1973] and *Dittberner and Vonder Haar* [1973] for a review of precipitation estimation techniques using visible and infrared satellite data.)

Several authors have shown the usefulness of microwave imagery from the Nimbus 5 electrically scanning microwave radiometer (ESMR) in depicting oceanic precipitation zones [*Theon*, 1973; *Sabatini and Merritt*, 1973; *Allison et al.*, 1974*a*, *b*; *Wilheit et al.*, 1976]. The present study uses Nimbus 5 ESMR data to infer tropical oceanic precipitation frequencies for the season December 1972 through February 1973. This approach is a first step toward measuring seasonal precipitation amounts, and the results may be of interest to modelers of the general circulation.

THE RADIOMETER

Nimbus 5 is a sun synchronous satellite which crosses the equator at 1130 and 2330 LT and has an orbital period of 107 min. The ESMR receives radiation in a 250-MHz band centered at 19.35 GHz (1.55 cm), with a noise equivalent temperature difference of approximately 2 K. The antenna electrically scans across the spacecraft track from 50° left to 50° right in 78 steps every 4 s. In this study, only data within 30° of nadir were used. The radiometer half-power resolution is 25 × 25 km at nadir and degrades to 42 km crosstrack by 30 km downtrack at 30° from nadir.

In the course of this study it was found that the ESMR brightness temperatures vary with scan angle in a manner not explainable as increased path length through the atmosphere or as variation of the sea surface emissivity. Also, a small offset between noon and midnight data was found. Additive corrections, amounting to at most 6 K, were developed by requiring the 3-month mean brightness temperature over nonraining areas of the Pacific Ocean to be independent of scan angle and local time [*Kidder*, 1976].

MICROWAVE DETECTION OF OCEANIC PRECIPITATION

Because the physics of the transfer of microwave radiation through the atmosphere has been described in detail elsewhere [e.g., *Wilheit*, 1972], only a brief summary will be given here. The 19.35-GHz brightness temperature of the ocean surface (emissivity 0.4) is approximately 120 K, which is colder than any thermodynamic temperatures encountered in the atmosphere. The active constituents of an atmospheric column (oxygen, water vapor, and liquid water) over the ocean are therefore seen in emission; they add to the upwelling radiation stream in the normal process of absorption and reemission. A nonraining atmospheric column, however, is more than 96% transparent; thus it adds only a small amount to the satellite-observed brightness temperature, which ranges from 125 to 175 K over the ocean in the absence of precipitation. Raindrops, which are comparable in size to the 1.55-cm ESMR wavelength, interact strongly with microwave radiation and rapidly increase the brightness temperature of an atmospheric column over the ocean. *Wilheit et al.* [1975] have done preliminary calculations of the 19.35-GHz brightness temperature as a function of rainfall rate and freezing level (Figure 1). Comparisons between radar data and ESMR data and between ground-based radiometer data and rain gage data indicate that these curves are accurate to within a factor of 2.

In this study, zonal mean freezing levels [*Oort and Rasmusson*, 1971; *Taljaard et al.*, 1969] were combined with the curves of Figure 1 to obtain zonal threshold brightness temperatures for the detection of precipitation during the season December–February (Figure 2). Brightness temperatures corresponding to the 0.25 mm h^{-1} rainfall rate were selected as thresholds to differentiate raining from nonraining observations on the basis that the curves of Figure 1 become relatively flat at 0.25 mm h^{-1}. The use of a threshold temperature to detect precipitation has several problems; among them are that (1) precipitating areas which do not fill the beam (500 km^2 at nadir) may

Paper number 7C0054.

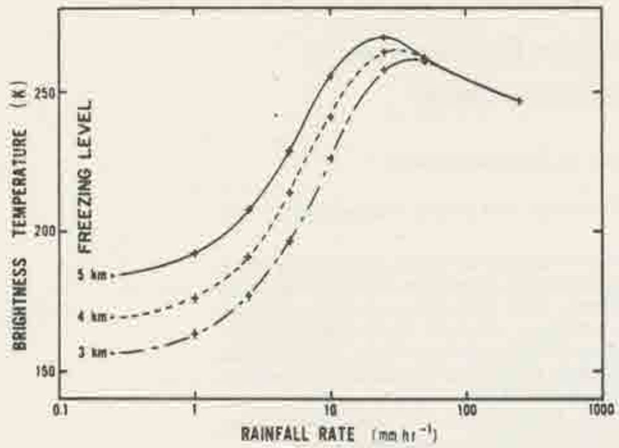

Fig. 1. Theoretical satellite-observed 19.35-GHz brightness temperature versus rainfall rate [after *Wilheit et al.*, 1975].

not be detected and (2) local atmospheric and surface conditions may deviate from those used to calculate the brightness temperature versus rainfall rate curves. However, comparison of radar data and ESMR data shows that the 170 K brightness temperature contour (which corresponds to a 0.25 mm h^{-1} rainfall rate when the freezing level is 4 km) closely follows the radar echo [*Allison et al.*, 1974*a*].

DATA ANALYSIS AND RESULTS

Data from the period December 22, 1972, through February 26, 1973, were stratified by position (5° latitude-longitude squares) and local time. The data in each category were first corrected for scan angle, and then the fraction of the observations above each of the brightness temperature thresholds was calculated. Figure 3 shows the fraction of observations above the 0.25 mm h^{-1} threshold, which may be interpreted as the frequency of precipitation regardless of intensity. Noon and midnight frequencies have been averaged. Figure 4 shows, for comparison, the precipitation frequencies of *McDonald* [1938] compiled from ship observations.

The microwave precipitation frequencies reproduce the expected general pattern: (1) narrow convergence bands, (2) dry eastern oceans, and (3) the splitting of the ITCZ in the mid-Pacific. The precipitation frequencies in the northwest oceans may be biased upward by the more frequent occurrence of strong winds in those areas [*McDonald*, 1938]. Strong winds, by forming foam on the sea surface, increase the surface emissivity and thus the observed brightness temperature [*Nordberg et al.*, 1971].

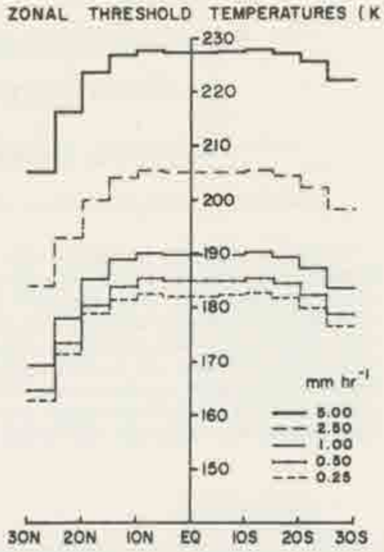

Fig. 2. Zonal 19.35-GHz threshold brightness temperatures for the detection of oceanic precipitation during the season December-February.

The microwave precipitation frequencies are generally lower than those of McDonald, and the mid-Pacific precipitation maximum seems to be about 20° further west. These findings are in agreement with *Ramage* [1975], who in his study of the 1972-1973 El Niño found that the frequency of highly reflective clouds was generally less in December 1972 than in the more normal period of December 1971 and that the position of maximum cloudiness had shifted westward in December 1972.

Figures 5-7, showing the frequencies of light (0.25-1.0 mm h^{-1}), moderate (1.0-2.5 mm h^{-1}), and heavy (>2.5 mm h^{-1}) precipitation, indicate that the ratios of the frequencies in these categories do not vary appreciably over the tropical ocean.

Finally, an indication of the diurnal variation of precipitation frequency was obtained by comparing the noon and midnight frequencies. Table 1, showing the percentage of the total of noon and midnight precipitation events occurring near

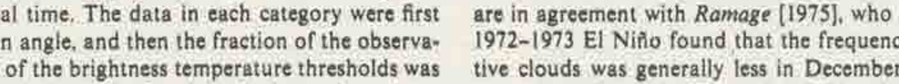

Fig. 3. Frequency of precipitation (in percent of observations) for the season December 1972 through February 1973 as derived from Nimbus 5 ESMR data. The noon and midnight observations have been averaged.

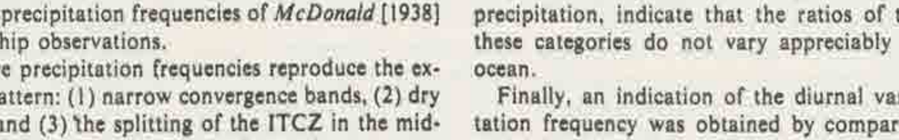

Fig. 4. Frequency of precipitation (in percent of observations) for the season December-February from ship observations taken at noon, universal time [after *McDonald*, 1938].

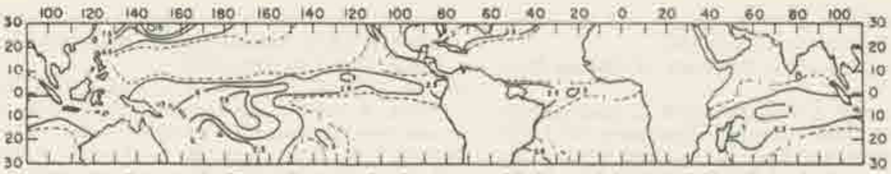

Fig. 5. Same as in Figure 3 except for frequency of light precipitation (0.25–1.0 mm h^{-1}).

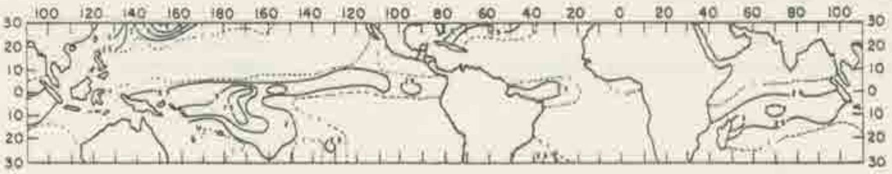

Fig. 6. Same as in Figure 3 except for frequency of moderate precipitation (1.0–2.5 mm h^{-1}).

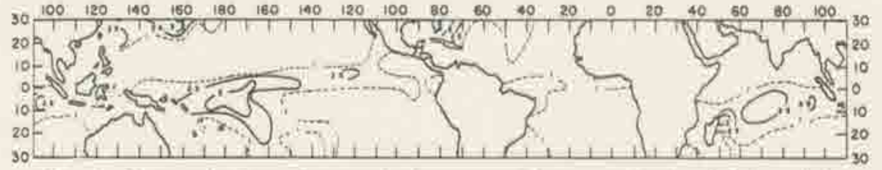

Fig. 7. Same as in Figure 3 except for frequency of heavy precipitation (>2.5 mm h^{-1})

TABLE 1. Percentage of the Total of Noon and Midnight Precipitation Events Occurring near Local Noon in Oceanic Regions Between 20°N and 30°S During the Season December 1972 through February 1973

Rainfall Category, mm h^{-1}	Precipitation Frequencies		
	Dry Regions (0–5%)	Wet Regions (5–100%)	All Regions (0–100%)
Light (0.25–1.0)	47	50	48
Moderate (1.0–2.5)	48	52	49
Heavy (2.5–5.0)	49	54	51
Very heavy (>5.0)	53	61	57
All rain	49	52	50

local noon in oceanic regions between 20°N and 30°S, indicates that there is little difference between noon and midnight precipitation frequencies. Although a diurnal variation of tropical oceanic precipitation with an early morning maximum and a late afternoon minimum has been observed, little difference is to be expected between noon and midnight frequencies [*Lavoie*, 1963; *Jacobson and Gray*, 1976]. However, the increasing tendency, shown in Table 1, for the heavier precipitation events to occur near local noon supports the early morning maximum.

CONCLUSIONS

Nimbus 5 ESMR data have yielded reasonable seasonal precipitation frequencies over the tropical oceans by use of preliminary calibration curves. Other investigators are working on obtaining oceanic precipitation amounts [*Rao et al.*, 1976] and on improving the calibration curves. Soon we will be able to accurately measure this important atmospheric parameter and its interannual variation.

Acknowledgments. This research was sponsored by the National Aeronautics and Space Administration under grant NGR-06-002-102. Acknowledgment is also made to the National Center for Atmospheric Research, which is sponsored by the National Science Foundation, for the computing time used in this research.

REFERENCES

Allison, L. J., E. R. Kreins, F. A. Godshall, and G. Warnecke, Examples of the usefulness of satellite data in general atmospheric circulation research, *NASA Tech. Note D-5630*, 1969.

Allison, L. J., E. B. Rodgers, T. T. Wilheit, and R. Wexler, A multisensor analysis of Nimbus 5 data on 22 January 1973, *NASA/GSFC X Doc. 910-74-20*, 1974*a*.

Allison, L. J., E. B. Rodgers, T. T. Wilheit, and R. W. Fett, Tropical cyclone rainfall as measured by the Nimbus 5 electrically scanning microwave radiometer, *Bull. Amer. Meteorol. Soc.*, *55*, 1074–[illegible], 1974*b*.

Dittberner, G. J., and T. H. Vonder Haar, Large-scale precipitation estimates using satellite data: Application to the Indian monsoon, *Arch. Meteorol. Geophys. Bioklimatol., Ser. B*, *21*, 317–334, 1973.

Jacobs, W. C., The seasonal apportionment of precipitation over the ocean, *Ass. Amer. Geogr. Yearb.*, *30*, 63–78, 1968.

Jacobson, R. W., and W. M. Gray, Diurnal variation of oceanic deep cumulus convection, *Atmos. Sci. Pap. 243*, Colo. State Univ., Fort Collins, 1976.

Kidder, S. Q., Tropical oceanic precipitation frequency from Nimbus 5 microwave data, *Atmos. Sci. Pap. 248*, Colo. State Univ., Fort Collins, 1976.

Lavoie, R. L., Some aspects of the meteorology of the tropical Pacific viewed from an atoll, *Rep. 27*, Hawaii Inst. of Geophys., Honolulu, 1963.

Martin, D. W., and W. D. Scherer, Review of satellite rainfall estimation methods, *Bull. Amer. Meteorol. Soc.*, *54*, 661–674, 1973.

McDonald, W. F., *Atlas of Climatic Charts of the Oceans*, U.S. Weather Bureau, Department of Agriculture, Washington, D. C., 1938.

Nordberg, W., J. Conaway, D. B. Ross, and T. Wilheit, Measurements of microwave emission from a foam-covered, wind-driven sea, *J. Atmos. Sci.*, *28*, 429–435, 1971.

Oort, A. H., and E. M. Rasmusson, Atmospheric circulation statistics, *NOAA Prof. Pap. 5*, U.S. Dep. of Commer., Rockville, Md., 1971.

Ramage, C. S., Preliminary discussion of the meteorology of the 1972–1973 El Niño, *Bull. Amer. Meteorol. Soc.*, *56*, 234–242, 1975.

Rao, M. S. V., W. V. Abbott III, and J. S. Theon, Satellite-derived global oceanic rainfall atlas (1973 and 1974), *NASA/GSFC X Doc. 911-76-116*, 1976.

Sabatini, R. R., and E. S. Merritt, The Nimbus 5 ESMR and its application to storm detection, *EPRF 51-0873-004*, U.S. Navy Environ. Predict. Res. Facil., Monterey, Calif., 1973.

Sellers, W. P., *Physical Climatology*, University of Chicago Press, Chicago, Ill., 1965.

Taljaard, J. J., H. van Loon, H. L. Crutcher, and R. L. Jenne, *Climate of the Upper Atmosphere, part 1, Southern Hemisphere*, vol. 1, National Center for Atmospheric Research, National Weather Records Center, and Department of Defense, Washington, D. C., 1969.

Theon, J. S., A multispectral view of the Gulf of Mexico from Nimbus 5, *Bull. Amer. Meteorol. Soc.*, *54*, 934–937, 1973.

Tucker, G. B., Precipitation over the North Atlantic ocean, *Quart. J. Roy. Meteorol. Soc.*, *87*, 147–158, 1961.

Wilheit, T. T., The electrically scanning microwave radiometer (ESMR) experiment, in *The Nimbus 5 User's Guide*, edited by R. R. Sabatini, ERTS/Nimbus Project, NASA/Goddard Space Flight Center, Greenbelt, Md., 1972.

Wilheit, T. T., M. S. V. Rao, T. C. Chang, E. B. Rodgers, and J. S. Theon, A satellite technique for quantitatively mapping rainfall rates over the oceans, *NASA/GSFC X-Doc. 911-75-72*, 1975.

Wilheit, T. T., J. S. Theon, W. E. Shenk, L. J. Allison, and E. B. Rodgers, Meteorological interpretations of the images from the Nimbus 5 electrically scanned microwave radiometer, *J. Appl. Meteorol.*, *15*, 166–172, 1976.

(Received September 24, 1976;
revised January 17, 1977;
accepted January 17, 1977.)

VOL. 83, NO. C4 JOURNAL OF GEOPHYSICAL RESEARCH APRIL 20, 1978

The Annual Variation in the Global Heat Balance of the Earth

J. S. Ellis[1] and T. H. Vonder Haar

Colorado State University, Fort Collins, Colorado 80523

S. Levitus and A. H. Oort

Geophysical Fluid Dynamics Laboratory/NOAA, Princeton, New Jersey 08540

An annual variation with a range of 31 W m^{-2} is found in the global net radiation balance of the earth. The net radiation flux values measured from satellites and the changes in total heat content computed from independent sets of atmospheric and oceanic data show annual variations which are consistent with each other in both phase and magnitude. The net energy gain and loss by the planet within a year is stored and released within the system primarily by the oceans.

INTRODUCTION

The analyses of independent sets of satellite radiation flux, oceanic temperature, and atmospheric temperature and humidity data presented in this paper give, for the first time, estimates of the annually varying heat balance of the earth. As far as the authors know, an annual variation in the global heat balance has not been reported in the literature. However, an annual variation in the global net radiation balance was suggested by *Simpson* [1929]. *Vonder Haar and Suomi* [1971] and *Raschke* [1973] indicated the possibility of an annual variation in the radiation balance from limited sets of early satellite data. The annual variation in the radiation balance reported in this paper has been determined from a 29-month composite of satellite data.

For global energy balance the net radiation flux across the upper atmospheric boundary must at all times equal the rate of change in total heat content of the combined atmosphere-ocean-cryosphere-land system. Energy available due to geothermal heating is extremely small in comparison with the flux of solar radiation [*Sellers*, 1965] and has been neglected in this study. Thus the energy balance for the atmosphere-earth system can be written as follows:

$$F_{TA} = S_A + S_o + S_L + S_I \qquad (1)$$

in which

$$F_{TA} = \int_{\text{globe}} [(1 - A)I - R]\, dA \qquad (2)$$

is the net global flux of radiation at the top of the atmosphere,

$$S_A = \frac{\partial}{\partial t} \int_0^{20\text{ km}} \int_{\text{globe}} \rho(C_A T + gZ + L_e q)\, dA\, dz \qquad (3)$$

is the rate of storage in the atmosphere,

$$S_o = \frac{\partial}{\partial t} \int_{-275\text{ m}}^{0} \int_{\text{globe}} \rho C_o T\, dA\, dz \qquad (4)$$

is the rate of storage in the oceans, S_L is the rate of storage in land (neglected in this study), S_I is the rate of storage in snow and ice, and

A planetary albedo;
C_A, C_o specific heat at constant volume for atmosphere and ocean;
g acceleration due to gravity;
I incoming solar flux;
L_e latent heat of evaporation;
q specific humidity of air;
R long-wave flux to space;
t time;
T temperature;
z height;
ρ density.

A height of 20 km was chosen as the 'top' of the atmosphere and a depth of 275 m as the lower limit of integration for the oceans because of the almost negligible contributions beyond these limits.

BASIC DATA

Data sets used in this study will be briefly described. Net radiative flux values were computed from a 29-month set of satellite data. Some of the important characteristics of this data set are shown in Table 1. The composited radiation values include data from wide-angle field of view sensors on board Experimental, Essa 7, Itos 1, and NOAA 1 satellites and medium field of view scanning sensors on board Nimbus 2 and 3 satellites. *Ellis and Vonder Haar* [1976] have discussed the spatial and temporal distribution of the data and uncertainties in the measurements. In a later part of this paper we will show that the total uncertainty in the composited global mean values is probably less than 10 W m^{-2}.

Atmospheric temperature and humidity data between the surface and 20-km height were taken from 5 years (May 1968–April 1973) of daily rawinsonde measurements at 850 meteorological stations over the globe. Figure 1 shows the distribution of these stations and illustrates the relative lack of observing stations in the southern hemisphere. As a result, less confidence can be placed in the southern hemisphere contribution to our results. The method of analysis of this data set is the same as the one used by *Oort and Rasmusson* [1971]. The uncertainty in the rate of atmospheric storage is less than 1 W m^{-2} for the northern hemisphere but somewhat larger for the southern hemisphere because of data void regions.

Oceanic temperature analyses were based on historical data files from the National Oceanographic Data Center, Washington, D. C., containing approximately 400,000 hydrographic soundings, 740,000 mechanical bathythermograph soundings,

---

[1] Now at Lawrence Livermore Laboratory, Livermore, California 94550.

Paper number 7C0932.
0148-0227/78/047C-0932$03.00

TABLE 1. Chronological List of Earth-Orbiting Satellites From Which Present Radiation Measurements Were Taken

	Year								Sample Size
	1964	1965	1966	1967	1968	1969	1970	1971	
January		EX (1030)				E7 (1430)	N3 (1130)		3
February		EX (1035)				E7 (1430)			2
March		EX (1040)				E7 (1430)			2
April						N3 (1130)	I1 (1500)		2
May			N2 (1130)			N3 (1130)	I1 (1500)	NO1 (1500)	4
June			N2 (1130)			N3 (1130)	I1 (1500)		3
July	EX (0830)		N2 (1130)			N3 (1130)			3
August	EX (0855)					N3 (1130)			2
September	EX (0915)								1
October	EX (0940)				E7 (1430)	N3 (1130)			3
November	EX (1005)				E7 (1430)				2
December	EX (1030)				E7 (1430)				2
Annual	6	3	3	0	3	9	4	1	29

The approximate local time at which each satellite crossed the equator during daylight hours is given in parentheses. EX stands for experimental; N2, Nimbus 2; N3, Nimbus 3; E7, Essa 7; I1, Itos 1; and NO1, NOAA 1.

and 100,000 expendable bathythermograph soundings. The data were averaged by month for each 1° latitude-longitude square at 11 standard levels between the surface and 250 m. An objective analysis scheme of the iterative difference-correction type [*Cressman*, 1959] was applied at each standard level to produce a global analysis. A depth of 275 m was taken as the maximum significant depth for the penetration of the annual temperature wave. Figure 2 shows the distribution of sea surface temperature observations for the month of March. The bias toward more observations in the northern hemisphere coastal regions is true of all other months as well. Because of this bias the oceanic estimates from the southern hemisphere must be considered less reliable than the estimates from the northern hemisphere. Examination of the distribution of observations as a function of depth for all months indicates that down to 250 m the distributions are similar to the surface distribution, although the number of observations does decrease. The use of historical data and the general lack of observations must be considered in evaluation of the oceanic rate of storage estimates. Essentially, a sampling problem is involved. With the exception of areas around ocean weather ship stations where relatively long-term serial data exist, most of our data are scattered in time. Our ocean analysis is an attempt to describe large-scale permanent or semipermanent features of the oceanic temperature distribution. The use of observations that may have been taken during anomalous situations will be reflected in the analysis. Uncertainty in the rate of oceanic storage is about 10 W m^{-2}, but owing to sampling deficiencies, particularly in the southern hemisphere, even this error estimate must be considered tentative. A complete description of the oceanographic data, their representativeness, and the analysis methods used can be found in the work of *Levitus and Oort* [1977].

The rates of heat storage in the atmosphere and ocean were computed as follows. Monthly means of the heat content were evaluated at all grid points for each month. Rate of heat storage for any particular month was then computed as the difference in heat content between the following and previous months.

The rate of storage in snow and ice was computed from the change in areal coverage of snow and ice reported by *Kukla and Kukla* [1974] for the period August 1968–July 1969, an average water equivalent depth of 50 cm for the snow and ice being assumed. The resulting values are quite small, about one half the atmospheric values, and correspondingly, their uncertainty contributes little to the uncertainty in the total rate of

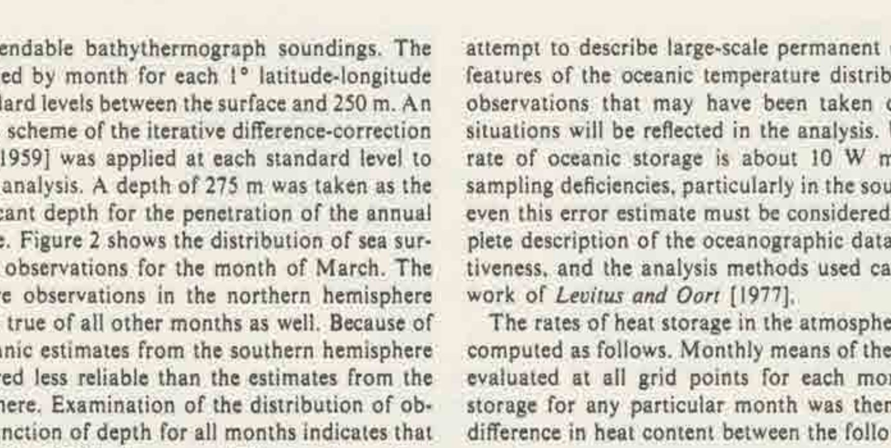

Fig. 1. Distribution of radiosonde stations.

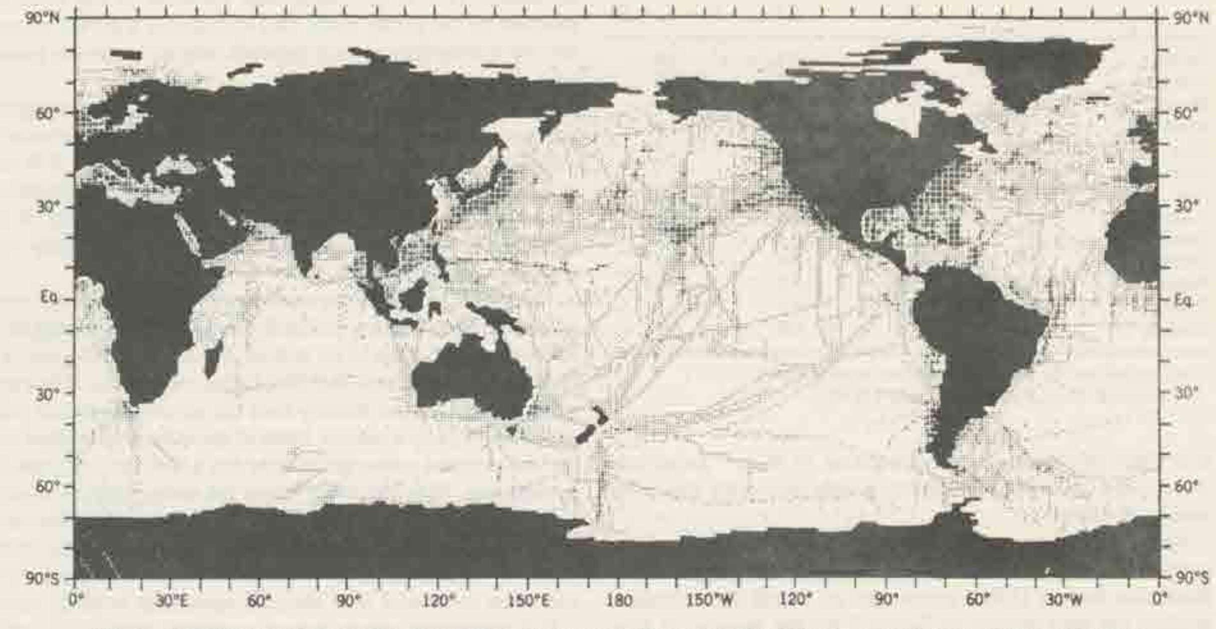

Fig. 2. Distribution of sea surface temperature observations for the month of March. A small dot indicates a 1° square containing less than 10 observations, and a large dot indicates 10 or more observations.

storage. More detailed information on the methods used in determining uncertainty in the rates of storage can be found in the work of *Oort and Vonder Haar* [1976].

Radiation Balance Components

The mean values of the radiation terms on the left-hand side of (1), which are based on the 29-month set of satellite data, are tabulated by month in Table 2. Shown are the global averages of reflected and long-wave flux to space at the top of the atmosphere. In addition, the computed global averages of incoming solar flux and net radiation at the top of the atmosphere are given as well as the albedo of the earth-atmosphere-ocean system. The incoming solar flux is computed from the known characteristics of earth-sun geometry and an assumed solar constant of 1360 W m^{-2} [*Drummond et al.*, 1968].

The mean global values of planetary albedo, long-wave, and net radiation flux are also shown graphically in Figure 3. The values for the 29 individual months of our data set are indicated by crosses, while the mean annual variation is shown by a solid curve. Of the seven zero net radiation values (or near-zero values), six are Essa 7 values. As a part of the Essa 7 data reduction method, global radiative equilibrium ($F_{TA} = 0$) was assumed to exist on a time scale of several days. This assumption was a necessary constraint for determining the planetary albedo. It is apparent from the distribution of values in Figure 3 that global radiative equilibrium does not generally exist even at the longer monthly time scale.

TABLE 2. Radiation Components of the Global Heat Balance

	I	A	$(1 - A)I$	R	F_{TA}
January	350.7	0.308	242.7	231.1	11.8
February	347.6	0.309	240.2	230.0	10.1
March	342.5	0.299	240.1	227.8	12.1
April	336.8	0.304	234.4	246.8	−12.4
May	332.0	0.314	227.8	245.0	−17.1
June	329.1	0.311	226.7	245.4	−18.6
July	328.8	0.296	231.5	236.5	−5.0
August	331.1	0.290	235.1	235.2	−0.3
September	335.7	0.287	239.4	231.1	8.4
October	341.6	0.298	239.8	235.8	4.1
November	347.1	0.313	238.5	232.6	5.8
December	350.5	0.318	239.0	230.7	8.5
Annual	339.5	0.304	236.3	235.7	0.6

All values (except A) are in units of watts per square meter.

The scatter of the values about the composited net radiation profile should be a measure of the uncertainty. The plotted values suggest a value of about 10 W m^{-2} for the uncertainty.

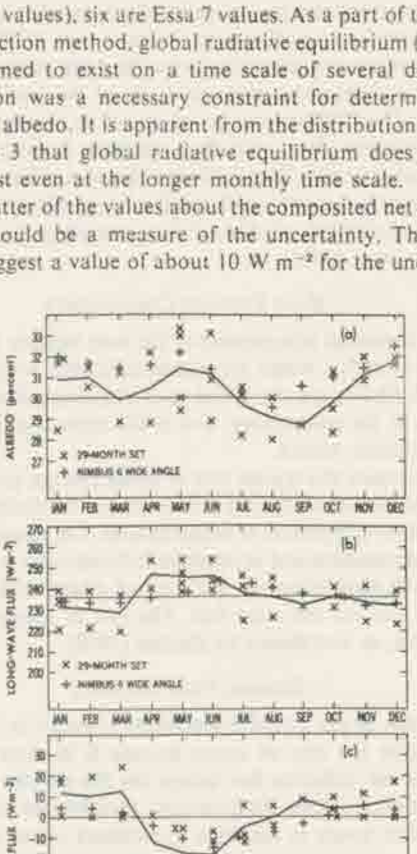

Fig. 3. Components of the global radiation balance of the earth. Shown are (*a*) the planetary albedo, (*b*) long-wave flux to space, and (*c*) net radiative flux.

TABLE 3. Storage Components of the Global Heat Balance

	S_0	S_A	S_I*	$S_0 + S_A + S_I$
January	−6.4	0.9	−0.1	−5.6
February	1.6	0.7	0.3	2.6
March	18.8	0.7	0.6	20.1
April	−5.2	1.6	0.9	−2.7
May	−25.5	2.2	0.9	−22.4
June	−9.5	2.6	1.2	−5.7
July	−1.7	0.6	0.6	−0.5
August	−6.0	−2.1	−0.1	−8.2
September	5.5	−3.1	−0.4	2.0
October	5.7	−2.8	−0.9	2.0
November	9.4	−1.4	−2.0	6.0
December	13.4	0.0	−1.1	12.3
Annual	0.0	0.0	0.0	0.0

All values are in units of watts per square meter.
*Estimated from *Kukla and Kukla* [1974].

It is clear that there is an approximate 15 W m^{-2} amplitude wave in the seasonal net radiation profile detectable above the scatter of values.

As an independent check, monthly averaged values of the components of radiation balance from the wide-angle Earth Radiation Budget (ERB) experiment on board the Nimbus 6 satellite are also plotted in Figure 3 for the months of July 1975–June 1976. These data are not included in the composited mean profile. They are preliminary data which incorporate corrections to the calibration transfer function and earth view factor as discussed by *Smith et al.* [1977]. The ERB albedo values are generally larger than the composited mean values, but the phase and amplitude of the profiles are quite similar. The ERB long-wave values are an average of daytime and nighttime data, and they compare favorably with the composited profile. During the months of April and May some differences are noted which could be a manifestation of interannual variability or diurnal time-sampling bias [*Ellis and Vonder Haar*, 1976].

HEAT STORAGE COMPONENTS

The terrestrial components of the heat balance in the right-hand side of (1), which are measured in situ, are presented in Table 3. Shown are the global rates of storage of energy in the oceans, in the atmosphere, and in the snow and ice cover for each calendar month.

To compute the typical rate of ocean storage per unit ocean area, the value of S_0 in Table 3 should be divided by 0.71, which is the proportion of ocean to land. The storage of energy in the atmosphere and cryosphere is found to be much smaller than and approximately 90° out of phase with the ocean storage and the radiation flux. The rate of storage in land is negligible, as was shown by *Gabites* [1950].

GLOBAL HEAT BALANCE

A graph of the global components is shown in Figure 4. It shows that the rate of ocean storage is in close agreement with the net radiation flux except for the months of January and February. (This disagreement may be due in large part to possible errors in southern hemisphere ocean data.)

The annual variation in the earth's net radiation balance may largely be accounted for by considering the effects which the present day earth-sun geometry and the asymmetrical distribution of continents between the northern and southern hemispheres have on the net radiation balance. The orbit of the earth about the sun is such that the earth is closest to the sun in January and farthest from the sun in July. This creates an annual 11.2 W m^{-2} amplitude variation in the solar flux received by the planet earth. This variation is a purely external driving mechanism, since it depends only on earth-sun geometry.

When a value of 30.4% (Table 2) for annual mean global albedo is used, the annual 11.2 W m^{-2} amplitude variation of incoming solar flux translates into an approximate 7.8 W m^{-2} variation in absorbed solar flux at the top of the atmosphere. This value is of interest, since it gives an estimate of the variation in absorbed solar flux apparently due solely to a change in earth-sun distance.

The global albedo varies considerably from the annual mean of 30.4%. This seasonal variability may be nearly described by a linear combination of an annual and semiannual wave. The minima, 29.9 in March and 28.7 in September, occur at a time when the sun is most directly over the earth's equatorial zone, which apart from a narrow band of cloudiness associated with the intertropical convergence zone has a lower albedo than the extratropics. Maxima occur when the snow- and ice-covered polar regions are receiving the greatest amount of incoming solar flux, near the solstices. An annual wave and other anomalies may be associated with the advance and retreat of sea ice and snow cover and with seasonal variability in cloud cover.

It is reasonable also to expect an annual cycle in the earth's long-wave emission to space because of the large surface temperature contrasts between land and oceans and the asymmetric land-sea distribution between the northern and southern hemispheres. Atmospheric data show an annual cycle in the global average near-surface temperature with an amplitude of 2°C [*Van Loon*, 1972]. Maximum and minimum values are found in July and January, respectively. This temperature variation may be interpreted as an amplitude variation of 7 W m^{-2} in the long-wave flux emission to space if typical atmospheric emissions are considered and all temporal variations in the intervening atmosphere are ignored [*Ellis*, 1977]. This effect in the long-wave flux combines with the effect in the absorbed flux to give a 15 W m^{-2} amplitude variation in the annual net radiation balance profile. The variation found in this suggested accounting of a cause and effect relationship is in close agreement with the variation observed in the composited profile from satellite data.

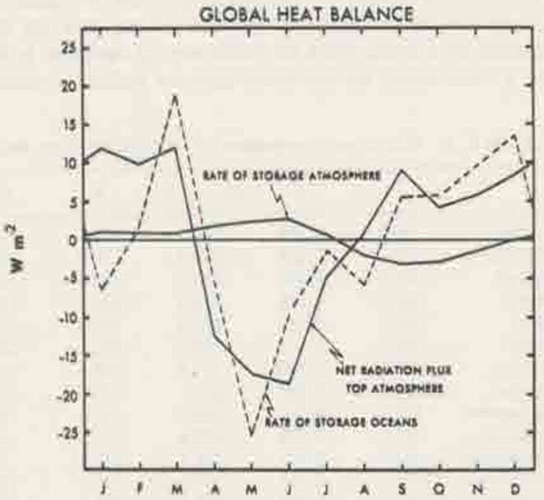

Fig. 4. Principal components of the global heat balance of the earth (in watts per square meter).

Examination of the storage components of the global heat balance shows that the world oceans play the dominant role in the earth's response to the annual variation in incoming solar flux. This result is expected because of the exceptionally high heat capacity of water and the large portion of the planetary surface covered by oceans. The rate of heat storage in the ocean is of nearly the same amplitude and in phase with the net radiation flux. The global ocean can maintain equilibrium by an average change in its heat content between times of maximum storage and maximum release of less than 1°C over a 50-m-thick layer.

The atmospheric component of the global heat balance is seen to be out of phase with the net radiation flux. This is a result of the global land-sea distribution. The maximum and minimum of the atmospheric component occur during northern hemisphere summer and winter, respectively. The extremes of heating and cooling of the atmosphere over the northern hemisphere continents dominate the annual cycle.

Although the rate of storage in ice and snow is relatively small, their presence or absence may influence the global heat balance because of their effect on the earth's albedo.

There is no doubt that each of the data sets used in this study contains inaccuracies. One must also consider that the observational periods during which the data in each set were taken are different. However, the fact that the satellite radiation budget and the atmosphere-ocean heat storage data sets are independent of each other yet give results which nearly satisfy both sides of (1) suggests that the annual cycle of global heat balance presented in this paper is real. Furthermore, the independent data sets are not likely to be grossly in error. The finer details in the annual variation must be considered tentative until improved data are collected and assimilated into a composite profile.

SUMMARY

The observations discussed in this paper may be summarized as follows. There is a significant annual variation in the two major components of the global heat balance: net radiation flux and rate of ocean storage. No cause and effect relationship is established; however, the effects of the earth-sun geometry, land-sea distribution, and pole to equator albedo difference in the global net radiation balance are discussed. The combined effects are in agreement with the observed annual variation. The world oceans apparently store and release heat in phase with the annual variation in the net radiation balance. The results of this study should be tested with more accurate and more extensive data as these data sets become available. Of particular interest are possible interannual variations from the average conditions reported in this paper.

Acknowledgments. Research performed at Colorado State University was partially supported by the National Aeronautics and Space Administration grant NGR06-002-102.

REFERENCES

Cressman, G. P., An operational objective analysis scheme, *Mon. Weather Rev.*, *87*, 367–374, 1959.

Drummond, A. J., J. R. Hickey, W. J. Scholes, and E. G. Love, New value for the solar constant, *Nature*, *218*, 259–262, 1968.

Ellis, J. S., Cloudiness, the planetary radiation budget, and climate, Ph.D. dissertation, Dep. of Atmos. Sci., Colo. State Univ., Fort Collins, 1977.

Ellis, J. S., and T. H. Vonder Haar, Zonal average earth radiation budget measurements from satellites for climate studies, *Atmos. Sci. Pap. 240*, 50 pp., Colo. State Univ., Fort Collins, 1976.

Gabites, J. F., Seasonal variations in the atmospheric heat balance, D. Sc. thesis, 272 pp., Mass. Inst. Technol., Cambridge, 1950.

Kukla, G. H., and H. J. Kukla, Increased surface albedo in the northern hemisphere, *Science*, *183*, 709–714, 1974.

Levitus, S., and A. H. Oort, Global analysis of oceanographic data, *Bull. Amer. Meteorol. Soc.*, *58*, 1977.

Oort, A. H., and E. M. Rasmusson, Atmospheric circulation statistics, *NOAA Prof. Pap. 5*, 323 pp., U.S. Government Printing Office, Washington, D. C., 1971.

Oort, A. H., and T. H. Vonder Haar, On the observed annual cycle in the ocean atmosphere heat balance over the northern hemisphere, *J. Phys. Oceanogr.*, *6*, 781–800, 1976.

Raschke, E., Satellites measure the radiation budget of the earth (in German), *Umschau*, *73*, 464–466, 1973.

Sellers, W. D., *Physical Climatology*, 272 pp., University of Chicago Press, Chicago, Ill., 1965.

Simpson, G. C., The distribution of terrestrial radiation, *Mem. Roy. Meteorol. Soc.*, *III*(23), 53–78, 1929.

Smith, W. L., J. Hickey, H. B. Howell, H. Jacobwitz, D. T. Hilleary, and A. J. Drummond, Nimbus-6 earth radiation budget experiment, *Appl. Opt.*, *16*, 306–318, 1977.

Van Loon, H., Temperature in the southern hemisphere, in *Meteorology of the Southern Hemisphere*, American Meteorology Society, Boston, Mass., 1972.

Vonder Haar, T. H., and V. E. Suomi, Measurements of the earth radiation budget from satellites during a five-year period, I, Extended time and space means, *J. Atmos. Sci.*, *28*(3), 305–314, 1971.

(Received December 16, 1976;
revised September 8, 1977;
accepted September 15, 1977.)

Presented at the Eleventh Technical Conference on Hurricanes and Tropical Meteorology of the AMS, Dec. 13-16, 1977, Miami.

SATELLITE-DERIVED TEMPERATURE STRUCTURE OF TROPICAL CYCLONES

Stanley Q. Kidder, William M. Gray and Thomas H. Vonder Haar

Department of Atmospheric Science
Colorado State University
Fort Collins, Colorado

1. INTRODUCTION

It has long been recognized that satellite data is useful in the study of tropical cyclones (Sadler, 1964). With the launch of the Nimbus 5 and Nimbus 6 satellites in 1972 and 1975, respectively, scanning radiometer data have become available in the radio window of the earth's atmosphere (1 mm to a few meters). Because clouds are nearly transparent to microwave radiation and because emission of microwave radiation is sensitive to a number of atmospheric and surface parameters, many studies of the microwave characteristics of tropical cyclones have begun to appear in the literature (e.g. Allison et al., 1974; Adler and Rodgers, 1976; Rosenkranz et al., 1977). Two important parameters of tropical cyclones are surface wind speeds and surface pressures. In this paper, we will examine one technique for extracting wind and pressure information in tropical storms from brightness temperatures measured by the Scanning Microwave Spectrometer (SCAMS) on board Nimbus 6.

2. THE RADIOMETER

The Scanning Microwave Radiometer is a five channel instrument sensing radiation nominally at 22.235, 31.65, 52.85, 53.85 and 55.45 GHz (Staelin et al., 1975). The upper three channels are used for sounding the atmosphere, while the lower two are used to measure integrated atmospheric water vapor and liquid water content. The lower two have also been used to measure surface wind speed in typhoon June (Rosenkranz et al., 1977). The radiometer scans across the spacecraft track in 13 steps at 7.2° intervals each 16 s. The half power beam width is 7.5°, which results in a spacial resolution of 145 km at nadir degrading to 220 km downtrack by 360 km crosstrack at the maximum scan angle. The orbit and scan geometries are such that the earth is viewed completely twice per day, and more often near the poles. The data are recorded on magnetic tape and archived at the National Space Science Data Center.

The upper three channels are located on the wing of an oxygen absorption band. In the absence of scattering (precipitation) the brightness temperature observed by channel i (i = 3, 4, 5) of the radiometer is given by:

$$T_{B_i} = \epsilon_i T_s t_i + \int_0^\infty T(z) W_i(z) dz \qquad (1)$$

where ϵ_i is the surface emissivity, t_i is the transmittance from the surface to the satellite, T_s is the surface temperature, $T(z)$ is the atmospheric temperature at height z and $W_i(z)$ is a weighting function (Staelin et al., 1974). $W_i(z)$ is weakly dependent on temperature, humidity, and ϵ_i, and is more strongly dependent on scan angle. Figure 1 shows the SCAMS weighting functions suitable for use over an ocean surface.

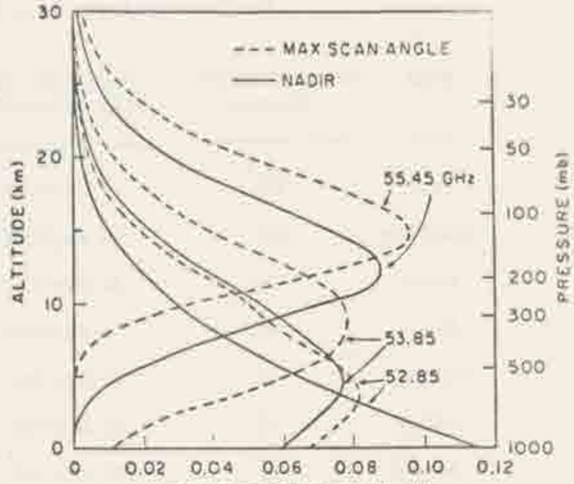

FIGURE 1. SCAMS weighting functions for use over an oceanic surface. (After Staelin et al., 1975.)

The RMS noise levels of the radiometer are 0.2 K for the lower two channels, and 0.5 K for the upper three. The absolute accuracy is ± 1.5 K (Rosenkranz et al., 1977).

3. TEMPERATURE ANOMALIES

The strong surface winds in a tropical cyclone can be traced through the hydrostatic and gradient wind equations to temperature anomalies centered in the upper troposphere. Frank (1977) has calculated the azimuthally-averaged temperature anomaly (difference from temperatures 14° from the storm center) for the mean typhoon (fig. 2). The main feature is the large positive anomaly centered between 250 and 300 mb and extending several hundred kilometers from the center of the storm. A much smaller cold anomaly exists at approximately 100 mb. Atlantic storms exhibit a very similar structure (LaSeur and Hawkins, 1963; Hawkins and Rubsam, 1968; Hawkins and Imbembo, 1976; Gray 1977).

Because the weighting function for SCAMS channel 5 peaks in the region of maximum temperature anomaly, one would expect to see a positive anomaly in the channel 5 brightness temperature over tropical cyclones. Indeed these anomalies have been observed previously by Rosenkranz and Staelin (1976) and by Rosenkranz _et al_. (1977) for West Pacific typhoon June of 1975. In an effort to substantiate the above findings and to relate them to surface characteristics, we obtained SCAMS data for eight typhoons and five hurricanes during 1975 (Table 1).

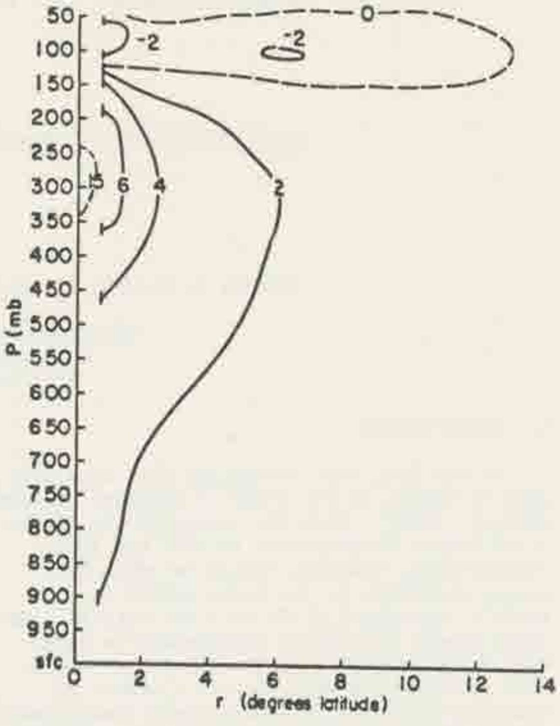

FIGURE 2. Temperature anomalies for the mean typhoon. (After Frank, 1977)

TABLE 1

Tropical Cyclones Used in this Study (all 1975).

NAME	PEAK INTENSITY (knots)	DATE/TIME OF PEAK INTENSITY	MINIMUM SEA LEVEL PRESSURE (mb)	CENTRAL LOCATION AT TIME OF PEAK INTENSITY	
June	160	19 Nov/12Z	875	13.2N	141.0E
Phyllis	120	14 Aug/18Z	925	24.1N	137.1E
Rita	80	22 Aug/12Z	---	32.9N	134.4E
Tess	95	4 Sep/18Z	945	23.0N	147.6E
Winnie	65	10 Sep/06Z	---	31.0N	162.8E
Alice	75	17 Sep/12Z	973	15.4N	123.1E
Betty	95	22 Sep/00Z	947	22.6N	123.6E
Cora	105	4 Oct/18Z	943	30.3N	133.2E
Caroline	100	31 Aug/00Z	963	24.0N	97.0W
Doris	95	2 Sep/18Z	---	37.7N	44.2W
Eloise	110	23 Sep/06Z	961	28.4N	87.3W
Faye	84	26 Sep/18Z	979	31.0N	63.1W
Gladys	125	2 Oct/00Z	942	31.0N	73.0W

The storms were positioned by interpolating between six hourly best track locations from the 1975 Annual Typhoon Report and from Hebert et al. (1977). Maximum sustained surface wind speed estimates for the typhoons were interpolated from the best track estimates from the Typhoon Report. Hurricane winds were interpolated between aircraft measurements, when available, and between satellite estimates, otherwise, both from Hebert et al. (1977). Central pressure estimates were interpolated between aircraft observations in Hebert et al. (1977) and Staff, JTWC (1976). In all, 116 images of the storms were collected. The quality of the images varies according to the minimum distance of the subsatellite point from the center of the storm and the amount of missing data.

Figure 3 shows examples of channel 5 brightness temperature anomalies over four storms of varying intensity. The temperatures plotted are the difference between the observed brightness temperatures and the mean brightness temperature in the region between 4° and 10° latitude from the storm center (the environment). Before the environmental temperature was calculated, all temperatures were corrected for scan angle by adding the temperatures listed in Table 2. This correction was developed by Rosenkranz et al. (1977) and it "flattens out the brightness temperature near the equator".

TABLE 2

Corrections to channel 5 (55.45 GHz) for scan angle away from vertical.

Scan Angle (degrees)	Correction (K)
7.2	0.1
14.4	0.6
21.6	1.8
28.8	3.2
36.0	4.9
43.2	7.2

Surface winds greater than 7 m s^{-1} cause foam formation which increases surface emissivity and can increase satellite observed brightness temperatures (Nordberg et al., 1971). However, the SCAMS channel 5 weighting function is zero at the surface; thus the channel 5 brightness temperatures are not affected by surface winds. Clouds and precipitation also alter the satellite-observed brightness temperature. At the levels sensed by SCAMS channel 5, most of the cloud droplets will be frozen which reduces their microwave absorption about two orders of magnitude (Westwater, 1972). Most of the precipitation is far below the peak of the channel 5 weighting function and thus should only change the satellite-observed brightness temperature slightly, and, because of back scattering by the raindrop-size particles, heavy rain will decrease the brightness temperature (Tsang et al., 1977). We conclude that the brightness temperature anomalies plotted in figure 3 represent real atmospheric temperature anomalies. This same conclusion was reached by Rosenkranz et al. (1977).

Typhoon June was an extremely large storm with 50 kt winds extending 200 n mi from the center (1975 Annual Typhoon Report). The warming in the center of June is striking. It extends 3° from the center and reaches 4.1 K. The warming in less intense storms is of lower magnitude and covers a smaller area. In weak storms such as Caroline, however, the warming is probably within the noise level of the data.

4. CENTRAL PRESSURES

It has been observed that the 50 mb level is virtually undisturbed by the tropical cyclone below it (Frank, 1977). It follows from the hydrostatic equation that a large positive temperature anomaly in the upper troposphere will cause a surface pressure drop. Because the SCAMS channel 5 brightness temperature is proportional to a weighted mean upper tropospheric temperature, it ought to be correlated with surface pressure. (See Gray (1977) for elaboration of this point.) However, the height (with respect to pressure) of the tropopause decreases from equator to pole and the temperature of the lower stratosphere increases. Since the peak of the SCAMS channel 5 weighting function is at a constant pressure, the environmental brightness temperature increases away from the equator. This is clearly evident in figure 3b. To avoid latitude corrections, we correlated central pressure with brightness temperature anomalies rather than with the brightness temperature itself. This is equivalent to assuming that the environment has a constant pressure.

A plot of central pressure versus maximum channel 5 brightness temperature anomaly within 2° of the storm center for the cases: (a) for which we had central pressure estimates, and (b) in which the satellite passed reasonably close to the storm center, is shown in figure 4. The correlation coefficient is -0.859, and the best estimate of the standard deviation from the regression line is ± 15 mb. Thus if this sample is representative of all tropical cyclone cases, one ought to be able to estimate the central pressure to within 15 mb approximately two thirds of the time. Some of the causes of variance are:

1) Radiometer noise
2) Eye smaller than radiometer resolution and of variable size
3) Non-constant environmental pressure
4) Vertical variation of the position of maximum warming
5) The scan angle correction
6) Non-centering of the eye in the radiometer scan spot
7) Weighting function peak not at level of maximum temperature anomaly
8) Clouds and precipitation.

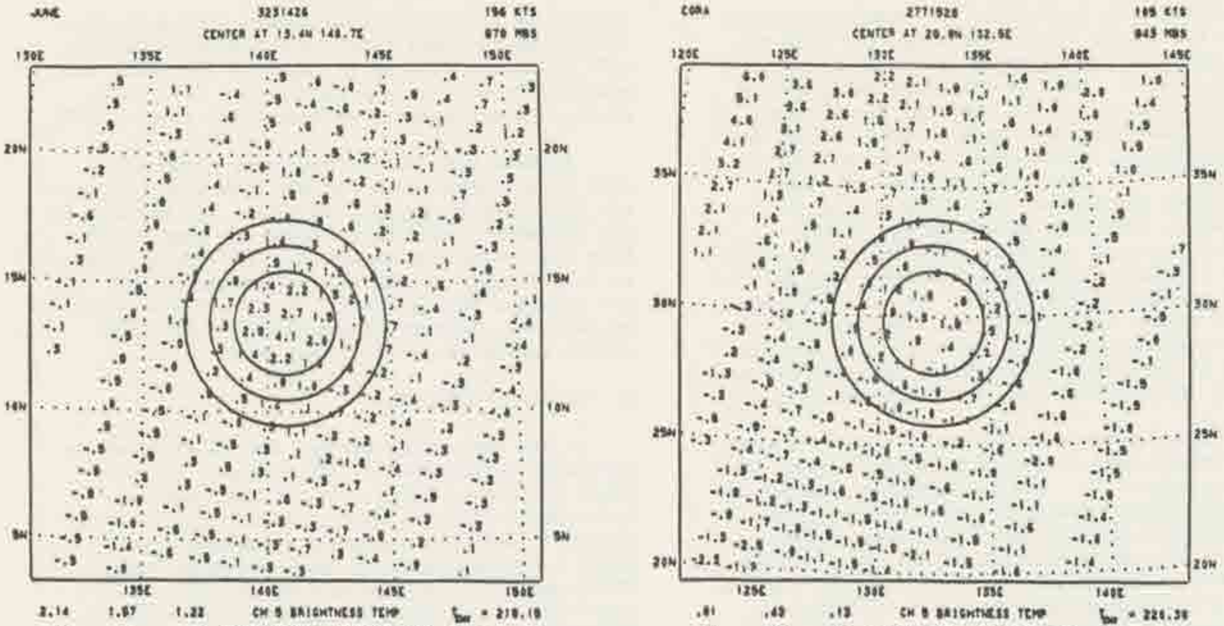

(a) Typhoon June on 19 November 1975 at 1426Z

(b) Typhoon Cora on 4 October 1975 at 1528Z

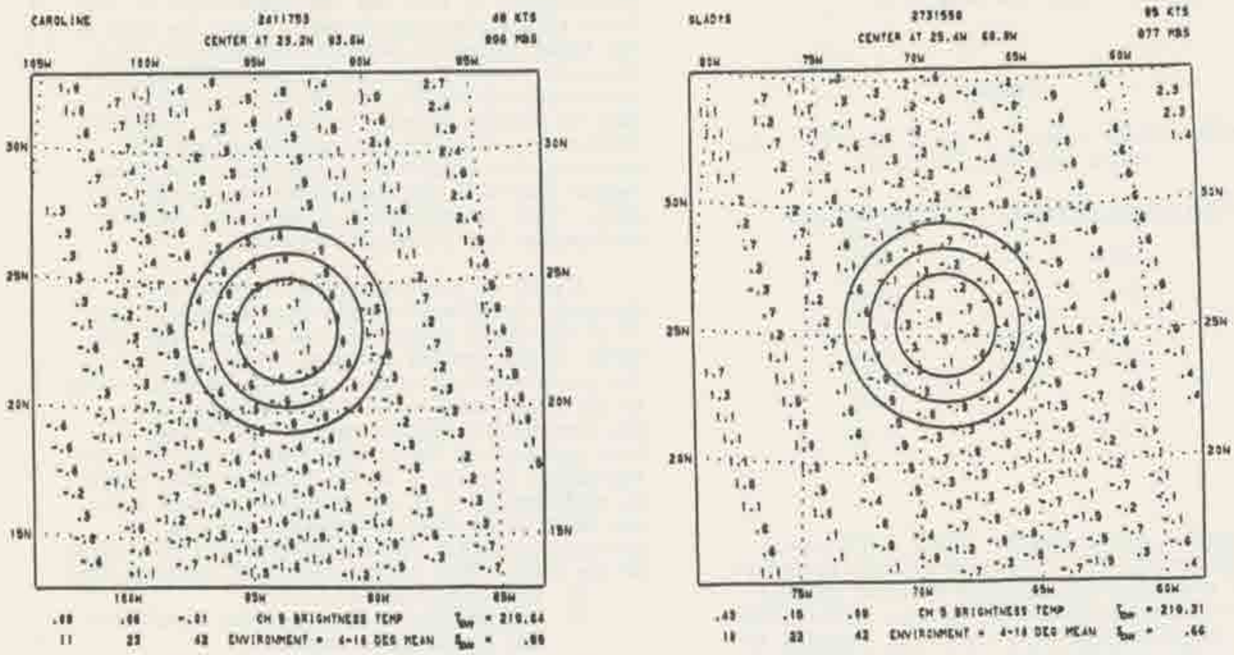

(c) Hurricane Caroline on 29 August 1975 at 1753Z

(d) Hurricane Gladys on 30 September 1975 at 1558Z

FIGURE 3. 55.45 GHz brightness temperature anomalies (K). The three circles are at radii of 2°, 3°, and 4° latitude from the interpolated best track storm center. The interpolated wind speed and central pressure are shown in the upper right hand corner. The environmental mean brightness temperature and its standard deviation are shown in the bottom right hand corner. The numbers in the bottom left hand corner are the mean anomalies inside the 2°, 3°, and 4° circles and the number of points used to calculate the means.

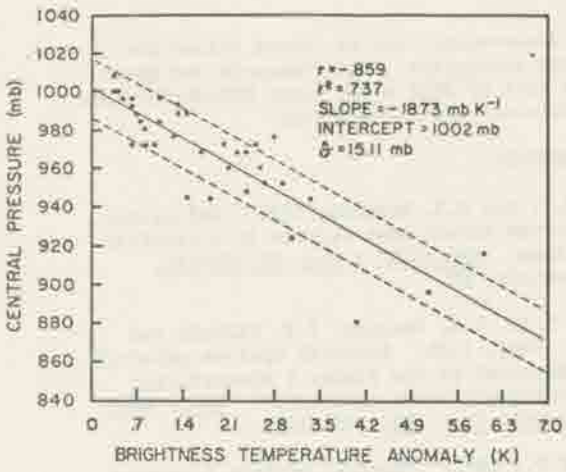

FIGURE 4. Central pressure versus maximum channel 5 brightness temperature anomaly within 2° latitude of the interpolated best track center.

Some of these errors may be corrected by more rigorous treatment of the data (3, 5, 8) and some could be alleviated in the future by a different radiometer design (1, 2, 7). Nevertheless, it is encouraging that this preliminary treatment of the data yields such a high correlation between central pressure and brightness temperature anomaly.

5. OUTER WINDS

If one can obtain the surface pressure field of a tropical storm, one can obtain an estimate of the surface winds by assuming that they are in gradient balance. It has been suggested by Hughes (1952), Riehl (1954, 1963) and Shea (1972) that outside the radius of maximum winds, the tangential wind varies with radius as:

$$V_\theta = Cr^{-x} \qquad (2)$$

where x is approximately 0.5. We assumed that $x = 0.5$ and that the tangential winds were in gradient balance,

$$RT\,\frac{\partial(\ln p)}{\partial r} = \frac{V_\theta^{\,2}}{r} + f\,V_\theta \qquad (3)$$

where R is the gas constant, T is the atmospheric temperature, and f is the Coriolis parameter. Treating f and T as constants, equation (3) can be integrated

$$\ln(p/p_o) = \frac{1}{RT}\left[-\frac{C^2}{r} + 2fCr^{1/2}\right] \qquad (4)$$

p_o is an integration constant. Setting

$$y = RT\,\ln p \qquad (5)$$

where p is the observed surface pressure, we find by the method of least squares that C is the positive, real root of the following equation.

$$\begin{aligned}
&\left[(\textstyle\sum r^{-2}) - \frac{1}{N}(\sum r^{-1})^2\right] C^3 \\
&+ 3f\left[\frac{1}{N}(\textstyle\sum r^{-1})(\sum r^{1/2}) - (\sum r^{-1/2})\right] C^2 \\
&+ \Big\{(\textstyle\sum yr^{-1}) - \frac{1}{N}(\sum y)(\sum r^{-1}) \qquad\qquad (6) \\
&+ 2f^2\left[(\textstyle\sum r) - \frac{1}{N}(\sum r^{1/2})^2\right]\Big\}\, C \\
&+ f\left[\frac{1}{N}(\textstyle\sum y)(\sum r^{1/2}) - (\sum yr^{1/2})\right] = 0
\end{aligned}$$

We used the regression line in figure 4 to calculate the surface pressures. Although the regression line underestimates pressures (being based on observations of a relatively small eye), and although there is noise in the pressure field produced, we believe that the azimuthal averaging inherent in the least squares technique produces approximately the correct radial pressure gradients and azimuthally-averaged tangential winds. For $T = 300$ K, we calculated tangential winds using the position of the maximum temperature anomaly inside 2° radius as the center of the storm. Figure 5 shows the results for the four storms in figure 3. Note the large differences in the outer circulations.

We have as yet no data with which to compare these curves. They appear to be reasonable, yet the winds for Gladys seem to be underestimated, and, in a few cases not shown, the winds at 1° radius are larger than the interpolated maximum winds. Still it is possible that improved treatment of the data could yield good estimates of the outer winds around tropical cyclones.

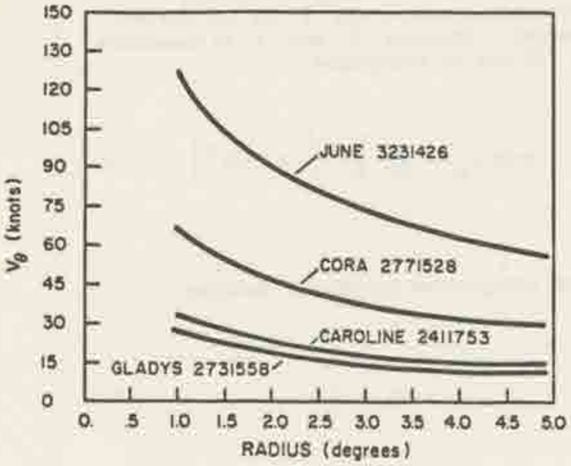

FIGURE 5. Calculated tangential winds for the four storms in figure 3.

6. SUMMARY AND CONCLUSIONS

Microwave observations from space contain a wealth of information on tropical cyclones which is unavailable from visible and infrared observations because clouds are opaque to visible and infrared radiation. The Dvorak technique (Dvorak, 1975), for example, yields estimates of maximum surface wind in a tropical cyclone from the structure of cloudiness observed in visible satellite images. However, it yields little or no information on outer winds or surface pressures because they are not well-correlated with cloudiness patterns. Microwave radiation, on the other hand, easily penetrates clouds and is sensitive to atmospheric and surface parameters which are directly related to surface winds and pressures. We believe that in the not too distant future, a complete picture of surface winds and pressures in tropical cyclones will be obtainable from satellite-borne microwave radiometers.

In this paper we have shown that the warm 55.45 GHz brightness temperature anomaly previously observed over typhoon June can be found over other tropical cyclones. We have correlated maximum brightness temperature anomaly with central pressure and calculated a correlation coefficient of -0.859. Finally, we calculated outer wind speeds by assuming gradient balance and using the regression between brightness temperature anomaly and central pressure to estimate the pressure gradients. These winds appear to be reasonable, but they have not been verified against observations. We conclude that the technique of using SCAMS-type data for measuring surface winds and pressures in tropical cyclones appears promising and deserves further attention.

7. ACKNOWLEDGEMENTS

The authors would like to thank Drs. D.H. Staelin and P.W. Rosenkranz of MIT for their encouragement and help in the interpretation of the data tapes, Dr. W.M. Frank of CSU for helpful discussions, and Ms. Donna Willey for typing the manuscript. This research was sponsored in part by NASA under Grant NGR-06-002-102, and by Colorado State University.

8. REFERENCES

Adler, R.F. and E.B. Rodgers, 1976: Satellite-observed latent heat release in a tropical cyclone. NASA/GSFC X Doc. 911-76-151, Greenbelt, MD.

Allison, L.J., E.B. Rodgers, T.T. Wilheit and R.W. Fett, 1974: Tropical cyclone rainfall as measured by the Nimbus 5 electrically scanning microwave radiometer. Bull. Amer. Meteorol. Soc., 55, 1074-1089.

Dvorak, V.F., 1975: Tropical cyclone intensity analysis and forecasting from satellite imagery. Mon. Wea. Rev., 103, 420-430.

Frank, W.M., 1977: The structure and energetics of the tropical cyclone I. Storm structure. Mon. Wea. Rev., 105, 1119-1135.

Gray, W.M., 1977: Cyclone intensity determination through upper tropospheric reconnaissance. Postprints, Eleventh Technical Conference on Hurricanes and Tropical Meteorology of the AMS, Miami, FL.

Hawkins, H.F. and D.T. Rubsam, 1968: Hurricane Hilda, 1964 II. Structure and budgets of the hurricane on October 1, 1964. Mon. Wea. Rev., 96, 617-636.

Hawkins, H.F. and S.M. Imbembo, 1976: The structure of a small intense hurricane - Inez 1966. Mon. Wea. Rev., 104, 418-442.

Hebert, P.J. and Staff, NHC, 1977: Annual data and verification tabulation Atlantic tropical cyclones 1975, NOAA Tech. Memo, NWS NHC 2, National Hurricane Center, Miami, FL.

Hughes, L.A., 1952: On the low level wind structure of tropical cyclones. J. Meteorol. 9, 422-428.

LaSeur, N.E. and H.F. Hawkins, 1963: An analysis of hurricane Cleo (1958) based on data from research reconnaissance aircraft. Mon. Wea. Rev., 91, 694-709.

Nordberg, W., J. Conaway, D.B. Ross and T. Wilheit, 1971: Measurements of microwave emission from a foam-covered, wind-driven sea. J. Atmos. Sci., 28, 429-435.

Riehl, H., 1954: Tropical Meteorology. McGraw-Hill, New York.

Riehl, H., 1963: Some relations between wind and thermal structure of steady-state hurricanes. J. Atmos. Sci., 20, 276-287

Rosenkranz, P.W. and D.H. Staelin, 1976: Summary of operations: The scanning microwave spectrometer (SCAMS) experiment. The Nimbus 6 Data Catalog, 3, NASA/Goddard Space Flight Center, Greenbelt, MD.

Rosenkranz, P.W., D.H. Staelin and N.C. Grody, 1977: Typhoon June (1975) viewed by a scanning microwave spectrometer. J. Geophys. Res., in press.

Sadler, J.C., 1964: Tropical cyclones of the Eastern North Pacific as revealed by TIROS observations. J. Appl. Meteor., 3, 347-366.

Shea, D.J., 1972: The structure and dynamics of the hurricane's inner core region. Atmos. Sci. Paper 182, Colorado State University, Fort Collins, CO.

Staelin, D.H., A.H. Barrett, P.W. Rosenkranz, F.T. Barath, E.J. Johnson, J.W. Waters, A. Wouters, and W.B. Lenoir, 1975: The scanning microwave spectrometer (SCAMS) experiment. The Nimbus 6 User's Guide, edited by J.E. Sissala, LANDSAT/Nimbus Project, NASA/Goddard Space Flight Center, Greenbelt, MD.

Staff, Joint Typhoon Warning Center, 1975: 1975 Annual Typhoon Report, Joint Typhoon Warning Center, COMNAVMARIANAS Box 12, FPO, San Francisco, CA.

Staff, Joint Typhoon Warning Center, 1976: Tropical cyclone center fix data for the 1975 typhoon season. FLEWEACEN Tech. Note JTWC 76-5, Joint Typhoon Warning Center, COMNAVMARIANAS Box 12, FPO, San Francisco, CA.

Tsang, L., J.A. Kong, E. Njoku, D.H. Staelin and J.W. Waters, 1977: Theory for microwave thermal emission from a layer of cloud or rain. IEEE Trans. Antennas Propagation, AP-24, 650-657.

Westwater, E.R., 1972: Microwave emission from clouds. NOAA Tech. Rep. ERL 219-WPL 18, NOAA/Environmental Research Laboratories, Boulder, CO.

THESIS

CLOUDINESS, THE PLANETARY RADIATION BUDGET, AND CLIMATE

Submitted by

James S. Ellis

In partial fulfillment of the requirements
for the Degree of Doctor of Philosphy
Colorado State University
Fort Collins, Colorado
Spring 1978

COLORADO STATE UNIVERSITY

March 10, 1978

WE HEREBY RECOMMEND THAT THE THESIS PREPARED UNDER OUR

SUPERVISION BY James S. Ellis

ENTITLED CLOUDINESS, THE PLANETARY RADIATION BUDGET, AND CLIMATE

BE ACCEPTED AS FULFILLING IN PART REQUIREMENTS FOR THE

DEGREE OF Doctor of Philosophy

Committee on Graduate Work

Adviser

ABSTRACT OF THESIS

CLOUDINESS, THE PLANETARY RADIATION BUDGET, AND CLIMATE

Satellite planetary radiation budget measurements from the Nimbus 3 satellite for four semi-monthly periods along with a 29 month composite of measurements from six satellites are applied in a quantitative study to evaluate the effect of cloudiness on the planetary radiation budget. Annual and seasonal results are expressed as zonal, hemispherical and global mean values.

The results show that for the planet as a whole the effect of "present day" clouds in reducing the absorbed shortwave flux is larger than their effect in reducing the longwave emitted flux. The difference between the two effects is significantly larger over oceans than over land. Similarly, the sensitivity to changes in cloud amount is greater in the shortwave absorbed flux than in the longwave flux emitted to space. It was also shown that the presence of clouds act to reduce the amplitude of the annual variation of the global planetary net radiation budget.

One may hypothesize from the results of this study and the works of others that a uniform increase in global cloud amount (in the absence of changes in cloud top height, cloud albedo, other atmospheric constituents, and vertical temperature lapse rates) will decrease the global mean surface temperature until radiative equilibrium is restored.

James Stephen Ellis
Atmospheric Science Department
Colorado State University
Fort Collins, Colorado 80523
Spring, 1978

ACKNOWLEDGEMENTS

I wish to express my appreciation to Dr. Thomas H. Vonder Haar for his guidance and encouragement on this project; this research was undertaken because of his confidence in the scientific merit of its objectives. Thanks are extended to Dr. Stephen Cox for his helpful suggestions on the manuscript. I also appreciate the many discussions with G. Garret Campbell, which were quite beneficial in formulating the scope of the research. This research was sponsored in part under NASA Grant NGR 06-002-102.

TABLE OF CONTENTS

Page

ABSTRACT iii

ACKNOWLEDGEMENTS iv

LIST OF TABLES vi

LIST OF FIGURES viii

1. INTRODUCTION 1

2. DATA COLLECTION, PROCESSING AND ANALYSIS 5

    2.1 Flux Estimates Before Satellite Measurements 6

    2.2 Satellite Measurement of Planetary Radiation Flux .. 6

    2.3 Cloud Free Flux 10
        2.3.1 Cloud Free Albedo 12
        2.3.2 Cloud Free Emitted Flux 25

3. CLOUD EFFECTS ON THE PLANETARY RADIATION BUDGET 36

    3.1 Zonal Mean Cloud Effect 38

    3.2 Global and Hemispherical Mean Cloud Effect 44

    3.3 Seasonal Variations in the Cloud Effect 47
        3.3.1 Zonal Variations 47
        3.3.2 Global Variations 50
        3.3.2.1 Indirect Analysis Method 51
        3.3.2.2 Direct Analysis Method 66

4. SENSITIVITY TO A UNIFORM CHANGE IN CLOUD AMOUNT 74

    4.1 Zonal Sensitivity 75
        4.1.1 Cloud Amount 75
        4.1.2 Absorbed Flux Sensitivity 78
        4.1.3 Emitted Flux Sensitivity 80
        4.1.4 Net Flux Sensitivity 83
        4.1.5 Atmospheric Transport Sensitivity 85

    4.2 Global and Hemispherical Sensitivity 96

5. CONCLUSIONS AND RECOMMENDATIONS 107

REFERENCES 110

APPENDIX A 116

APPENDIX B 119

APPENDIX C 127

LIST OF TABLES

Page

2.1 Chronological list of earth-orbiting satellites from which the radiation measurements were taken.............8

2.2 Uncertainty in mean monthly net radiation...............9

2.3 Nimbus 3 MRIR semi-monthly data sets...................11

2.4 Cloud-free albedo.....................................24

3.1 Cloud effect in net flux (ΔN) for land-plus-ocean.......46

3.2 Cloud effect in net flux (ΔN) for oceans...............46

3.3 Cloud effect in net flux (ΔN) for semi-monthly periods..67

3.4 Cloud effect in albedo (Δα) for land-plus- ocean........67

3.5 Cloud effect in emitted flux (ΔI) for land-plus-ocean....67

3.6 Cloud effect in emitted flux (ΔI) for oceans...........70

4.1 Zonal values of $\frac{\partial N}{\partial Ac}$...................................89

4.2 Sensitivities associated with removal of stratus-type clouds from the Eastern Pacific Ocean in the 15N-35N latitude zone...92

4.3 Sensitivity of the atmospheric energy transport out of the 0-30N latitude zone to interannual variations of cloud amount in the 0-15N latitude zone.............95

4.4 Annual global statistics (90N-90S)....................96

4.5 Summary of satellite derived statistics................97

4.6 Annual sensitivities (65N-65S).........................98

4.7 Annual global sensitivities............................99

4.8 Annual global longwave sensitivity derived from models .104

A.1 Directional reflectance relative to the value at solar zenith angle of zero degrees for the Nimbus 3 ocean and cloud models...118

Page

B.1 Regression coefficients (A) and standard error of estimate (e) for equation (B.1)......................121
B.2 Infrared spectral channels of the MRIR of the Nimbus 3 satellite...121
B.3 Spectral broadband empircial, broadband model and spectral model radiances calculated for a model atmosphere...123
C.1 Mean monthly global planetary radiation budget.......128

LIST OF FIGURES

Page

2.1 Albedo and cloud-free albedo over land-plus-ocean........16

2.2 Albedo and cloud-free albedo over oceans. 17

2.3 Photograph from aircraft showing partial cloud cover above Greenland's ice sheets on 22 June 1975 at 1600G.M.T. 20

2.4 Annual albedo and cloud-free albedo over land-plus-ocean, ocean and land. 22

2.5 Longwave flux and cloud-free longwave flux over land-plus-ocean. 28

2.6 Longwave flux and cloud-free longwave flux over oceans...29

2.7 Annual longwave flux and cloud-free longwave flux over land-plus-ocean, ocean and land. 33

3.1 Cloud effect on net flux for land-plus-ocean. 39

3.2 Cloud effect on net flux for oceans. 40

3.3 Annual cloud effect on net flux over land-plus-ocean, ocean and land. 41

3.4 Time-latitude analysis of zonal mean profiles from the 29 month set: (a) albedo, (b) longwave flux, (c) net flux and (d) cloud amount. 48

3.5 Annual variation in global net flux. 52

3.6 Annual variation in global albedo. 56

3.7 Annual variation in global longwave flux. 59

3.8 Annual variation in global net flux with just an annual wave in longwave flux. 65

Page

3.9 Annual variation in net flux and in the cloud effect on net flux for four semi-monthly periods. 73

4.1 Cloud amount from TIROS nephanalyses. 77

4.2 Absorbed flux sensitivity to changes in cloud amount. 79

4.3 Longwave flux sensitivity to changes in cloud amount. 81

4.4 Net flux sensitivity to changes in cloud amount. 84

4.5 Atmospheric mean meridional energy flux divergence for the 30N-to-90N polar cap. 87

4.6 Atmoshperic mean meridional energy flux divergence for the equator-to-30N latitude zone. 87

4.7 Atmospheric mean meridional energy flux divergence for the equator-to-90N polar cap. 88

4.8 Longwave flux emitted by the earth-atmosphere system as a function of cloud amount for various heights of radiometrically black clouds. 101

1. INTRODUCTION

The objective of this study is to quantitatively determine the effect of clouds on the planetary radiation exchange with space. This effect is examined on spatial scales from zonal mean to global and temporaly from months to an annual mean.

This study was undertaken to satisfy a need for quantitative information on the role of cloudiness in maintaining or changing climate regimes. Present climate study models cannot adequately incorporate clouds and cloud effects in an interactive mode because of the lack of observational and diagnostic studies of cloudiness at the larger planetary scale. Schneider (1972) clearly stated the problem... the global distribution of cloudiness is itself a consequence of the general circulation which, in turn, is driven by virtue of the latitudinal radiative imbalance between the incoming solar (minus the reflected flux) and the outgoing atmospheric IR (emitted longwave flux) radiation. Thus, in a study of the sensitivity of the global climate to changes in cloudiness, it is first necessary to determine the initial magnitude of such changes in cloudiness on the radiation balance. Simpson (1928) discussed the same problem but more from a point of view of required changes in cloud amount to offset changes in incoming solar radiation. Studies of this type have been more recently undertaken by Schneider (1972) and Cess (1976). Schneider found that a uniform change in global cloud amount has a significant effect on the globally integrated planetary radiation budget while Cess (1976) found it to have an insignificant effect. Cess went on to conclude that clouds may not provide a significant climate feedback mechanism.

Cloudiness has traditionally been specified by cloud type, amount and base height above the ground. Even if these cloudiness specifications were exactly determined over the entire planet, they would not be sufficient for determining radiative properties of the clouds. Additional information needed are the cloud top height and temperature, the absorptance, emittance and reflectance or transmittance of the clouds. These are minimum requirements. Specification of microphysical processes and properties within the clouds would aid the specification of some of the cloud properties. The measurement of all aforementioned cloud properties is difficult to perform at the small scale (mesoscale 2 to 200 km). The technology has not been and may never be implemented or totally developed to make such measurements on the global scale. Yet such information is needed for the specification of the radiative properties of clouds.

The present study short-circuits the very detailed measurements of individual cloud properties by determining with satellite measurements the bulk effect of cloudiness on the planetary radiation budget. By bulk is meant a taking together of all the properties without discriminating the effect of any one property. The importance of the present study is in the need for the information, the simplicity and accuracy of the method, and that the measurements are now available to quantitatively implement the method.

The joint Organizing Committee (JOC) of the World Meteorological Organization (WMO) and the International Council of Scientific Unions (ICSU) in a plan for advancing our knowledge of the climate and its variations (GARP No. 16, 1975) proposed observational efforts in three categories. Basically the three categories were directed at describing processes relevant for modeling, testing and validating models, and long-term monitoring programs of diagnostic variables for the detection of possible future climatic variations. A requirement for knowing the effect of the appearance and disappearance of various forms of extended cloudiness on the radiation budget is identified in their report (Chapters 5 and 6). Studies of the present type have applicability to all three categories but are most relevant to the latter two categories in testing and validating models, and monitoring diagnostic variables of a changing climate. Besides the immediate application to climate study models for initialization, constraint and validation of model output, the results of the study will be available to validate the radiative effect of clouds from detailed measurements as they become available.

The planetary radiation exchange with space is partitioned into incoming solar flux, reflected and scattered solar flux back to space, and emitted terrestrial flux. The incoming minus the other two component fluxes is the net flux. The components, other than solar flux, have been determined from measurements by earth orbiting satellites and are indicative of the fluxes at satellite height, or at some lower height above which the earth's atmosphere has no radiative properties significant to this study.

The effect of cloudiness on the radiation exchange with space is determined by measurements of the radiation budget components from space of a cloudy and cloud-free planet earth. The difference between the two states is the cloud effect for the present climate. Given the cloud effect for our present cloud cover, an extrapolation is made to other cloudiness states of both lesser and greater cloud cover.

The development of the satellite measured radiation budget components is discussed followed by development of the method and its application to zonal and global space scales. Finally, a discussion of the sensitivity of the planetary radiation budget to changes in cloudiness is given so that its significance as a climate feedback mechanism may be assessed.

2. DATA COLLECTION, PROCESSING AND ANALYSIS

Radiative energy flux between space and planet Earth, including its atmosphere, has been determined both through model calculations and direct measurement by earth orbiting satellites. Previous model calculations which normally relied on ground base measurements, some aircraft measurements and theory gave reasonable values for the fluxes. Since the middle 1960's earth orbiting satellites have been measuring the fluxes. A considerable number of satellite measurements collected since then have permitted the development of a planetary radiation budget climatology.

The planetary net radiation budget is composed of incoming solar flux, reflected solar flux to space and emitted terrestrial flux. It is mathematically defined at top of the earth-atmosphere boundary as:

$$N = (1-\alpha)\ S-I \tag{2.1}$$

where:

α = the ratio of reflected solar flux summed over all angles to the incoming solar flux

S = incoming solar flux based on a solar constant (SC) of 1360 wm^{-2} (after Drummond et.al. 1968)
$S = SC(\frac{\bar{d}}{d})^2$ cosine ξ

I = emitted flux by earth-atmosphere system.

2.1 Flux Estimates Before Satellite Measurements

Prior to the availability of a planetary radiation budget climatology from satellite measurements, planetary heat budget studies required estimates of the radiation budget. Several extensive works published then computed the radiative energy fluxes by the application of theory to a combined set of ground based and aircraft measurements.

Two such studies include that of London (1957) for just Northern Hemisphere and that edited by Budyko (1963) for the entire planet. In both studies, the cloud effect on solar and terrestrial fluxes had to be incorporated into cloud-free planetary calculations. These cloud effects were estimated from ground based observations of cloud amount and type and aircraft and ground measurements of cloud radiative characteristics.

2.2 Satellite Measurement of Planetary Radiation Flux

Data from satellite measurements of reflected shortwave and emitted longwave radiances have been compiled into global radiation budget climatologies. They are in chronological order as follows: Bandeen et al. (1965), Raschke and Pasternak (1967), Winston and Taylor (1967), Vonder Haar and Suomi (1971), Raschke et al. (1973a), Vonder Haar and Ellis (1974), and Ellis and Vonder Haar (1976). The last two publications are the most extensive including as many as six separate satellite measuring systems. The last publication, Ellis and Vonder Haar

(1976), is a compilation of 29 months of measurements summarized into mean month, season and annual zonal mean-meridional profiles. This satellite data base is used for the present study.

The 29 month set is a selective compilation including many, but excluding some of the satellite measurements available at that time. Table 2.1 is a list of all measurements comprising the set. Analyzed measurements from the later two satellites, ITOS 1 and NOAA 1 are from Flanders and Smith (1974). All measurements are from polar orbiting satellites in sun synchronous orbits. Local daylight sampling time at the equator is also given in the table. There is considerable daytime diurnal variability in sampling with Experimental in the morning, Nimbus 2 and 3 near noon and ESSA7, ITOS 1 and NOAA 1 in the afternoon.

The publication by Ellis and Vonder Haar (1976) gives a complete discussion of the data set and treats in detail uncertainties in the measurements. Uncertainty in the monthly means of net radiation summarized from that publication are shown in Table 2.2. The uncertainties are generally less than $10wm^{-2}$ with smallest values near polar regions of the winter hemisphere.

In the present study measurements from Nimbus 3 are used separately and as a part of the 29 month set. A complete description of the medium resolution infrared radiometer (MRIR) aboard the satellite is given in the NIMBUS III USER'S GUIDE (1969). It is a 5 channel

Table 2.1 Chronological list of earth-orbiting satellites from which the present radiation measurements were taken. The approximate local time at which each satellite crossed the equator during daylight hours is given in parentheses. EX = Experimental, N2 = Nimbus 2, N3 = Nimbus 3, E7 = ESSA 7, I1 = ITOS 1 and NO1 = NOAA 1.

	YEAR								
MONTH	1964	1965	1966	1967	1968	1969	1970	1971	SAMPLE SIZE
Jan		EX (10:30)				E7 (13:00)	N3 (11:30)		3
Feb		EX (10:35)				E7 (14:30)			2
Mar		EX (10:40)				E7 (14:30)			2
Apr						N3 (11:30)	I1 (15:00)		2
May			N2 (11:30)			N3 (11:30)	I1 (15:00)	NO1 (15:00)	4
Jun			N2 (11:30)			N3 (11:30)	I1 (15:00)		3
Jul	EX (08:30)		N2 (11:30)			N3 (11:30)			3
Aug	EX (08:55)					N3 (11:30)			2
Sep	EX (09:15)								1
Oct	EX (09:40)				E7 (14:30)	N3 (11:30)			3
Nov	EX (10:05)				E7 (14:30)				2
Dec	EX (10:30)				E7 (14:30)				2
ANNUAL	6	3	3	0	3	9	4	1	29

Table 2.2 Uncertainty in mean monthly net radiation (wm^{-2})

Latitude	Jan	Feb	Mar	Apr	May	Jun	Jul	Aug	Sep	Oct	Nov	Dec
North 85°	4	5	7	8	8	11	12	14	8	5	6	5
75	5	8	8	9	8	10	11	13	9	9	6	6
65	8	8	7	9	8	9	9	9	10	7	9	8
55	6	9	8	9	7	9	9	10	11	8	10	9
45	7	8	8	10	7	9	9	10	13	7	11	10
35	7	9	9	10	8	9	9	11	14	8	9	8
25	8	10	10	11	8	9	9	11	15	8	10	9
15	8	10	10	11	8	9	8	10	14	8	10	10
5	8	10	10	11	7	8	8	10	14	8	10	10
South 5	8	10	10	10	7	9	8	10	15	9	10	10
15	9	10	10	11	8	9	9	11	15	9	11	11
25	9	10	10	10	7	8	8	10	15	9	11	11
35	9	10	10	10	7	7	7	9	13	8	11	11
45	9	10	9	9	6	7	8	8	12	8	10	11
55	9	10	9	8	5	10	7	10	11	7	11	11
65	9	10	8	7	10	5	5	6	9	7	11	12
75	10	10	7	9	4	4	4	4	5	6	12	14
85	10	14	9	6	4	4	3	4	4	7	12	14

instrument with one shortwave channel (0.2 to 4.8 μm) and four longwave channels spanning the spectral range 6.0 to 23.9 μm). Total outgoing longwave radiance was computed by Raschke et al. (1973) through application of a multiple least-square regression formula to radiances in each of the four longwave channels. The field of view (FOV) of the instrument varied from 50 km of geocentric arc distance at satellite nadir to 110 km at an angle of 40° from nadir. The measurements were mapped to polar stereographic and mercator projections at 500 km to 200 km earth located grid spacing. This gridding allows grid scale to global scale studies.

Wide angle measurements by flat plate radiometers comprise 19 months of the 29 month set. Measurement resolution at the earth's surfaces varies with height of the satellite. For satellite heights in this set, the ground resolution of the wide angle sensors is 5900 km to 7770 km of geocentric arc distance in diameter. These data have been mapped on a 10 degree latitude-longitude grid. It is preferable to use these data for spatial scale studies of the 6000 km to global scale.

2.3 Cloud Free Flux

The satellite data set is composed of individual measurements of flux from cloud-free and cloudy atmospheres. To assess the effect of cloudiness on the components of the planetary radiation budget it is necessary to know the flux components over a cloud free earth-atmosphere system. Cloud free reflected and emitted flux may be determined from satellite measurements. The small grid scale mapping, small FOV, and daily sampling during all seasons of the year by the Nimbus 3 MRIR permit a cloud-free determination. These gridded data are archived as 10 semi-monthly sets (table 2.3).

Table 2.3 - Nimbus 3 MRIR semi-monthly data sets*

April 16 to 30, 1969
May 1 to 15, 1969
May 16 to 31, 1969
June 1 to 15, 1969
June 16 to 30, 1969
July 1 to 15, 1969
July 16 to 31, 1969
August 1 to 15, 1969
October 3 to 17, 1969
January 21 to February 3, 1970

Four semi-monthly sets were selected from the 10 sets, one within each season of the year, to approximate the variation of the planetary radiation budget with season. The four periods having the best temporal and spatial sampling are: May 1-15, July 15-31, October 3-17, 1969 and January 21-February 3, 1970. The last period, representing winter in the Northern Hemisphere, is inadequate poleward of 45N due to large data void regions, particulary over the North Pacific Ocean (Raschke et al., (1973b) shows global maps).

---

* From Raschke, et al, (1973b)

2.3.1 Cloud Free Albedo

Cloud free albedoes may be determined at each horizontally spaced grid area by selecting the smallest measured albedo value from a time series of measurements at that grid area. The concept assumes that a cloudy grid area has a higher albedo value than does a grid area which is cloud-free. This minimum method of obtaining cloud-free measurements in the shortwave portion of the solar spectrum has previously been applied by Coburn (1971) and Miller and Feddes (1971) to satellite measured brightness values. Coburn found that a time series of 7 days was sufficient to observe most grid areas as cloud-free. In the present study a time series extending the duration of each semi-monthly period has been used.

One may conceive of partly cloudy cases with the albedo as seen from space being less than the cloud-free albedo. Two such cases could occur with scattered clouds over wet soil or a vegetated region versus cloud-free, dry soil or desertificated soil. Instances of this type are considered to be within the noise of the cloud effect study.

The minimum albedo is not a cloud-free albedo at all grid areas because of residual cloudiness not removed by the minimum method. Persistent stratus cloudiness over oceans east of subtropical high pressure centers are not always removed. Chen (1975) using data from a higher spatial resolution instrument, the NOAA 4 scanning radiometer, also observed this. Some grid areas in regions of frequently occuring extratropical cyclones, such as the Aleutian Islands and Icelandic region, are not observed cloud-free during a semi-monthly period. Furthermore, in the intertropical convergence zone with frequent and persistent cloudiness, which are often smaller than the spatial gridding of Nimbus 3 MRIR measurements, clouds are not removed from all grid areas by minimum compositing.

To "clean-up" minimum albedo maps so as to obtain cloud free zonal mean meridional profiles, further processing was required. The initial data reduction of the MRIR measurements required application of models to account for anisotropic reflections from various surfaces in the FOV (Raschke et al, (1973)). There were three models called cloud-land, snow, and ocean models. All three models accounted for the directional dependence of reflectance on solar zenith angle and bi-directional reflectance dependence on position of observer and solar zenith angle. A criterion for applying the ocean model, a model applicable to cloud-free ocean reflectances only, was that the measured reflectance be 0.10 or less. Presumably, one should be able to use the solar zenith angle dependence part of this model (the directional reflectance part) to compute an upper limit reflectance cut off value. All reflectance values above the cut off are cloudy values, and thus should be eliminated from the minimum albedo maps. (See Appendix A for ocean and cloud-land models.)

Conover (1965) determined cloud-free albedoes over the Gulf of Mexico to be 0.09 and over the Pacific Ocean to be 0.07. The values were taken as an average from the TIROS VII satellite measurements at solar zenith angles between 3 and 42 degrees. If 0.09 is taken as the instantaneous directional reflectance at a zero solar zenith angle ($\xi=0$), then application of the ocean directional reflectance model will overestimate the daily mean cloud-free albedo. The model calculations give a daily average albedo of 0.115 at the latitude of solar declination, which is significantly larger than Conover's 0.09. However, using the 0.09 value as an upper limit cloud-free reflectance value (at $\xi=0$) allows for varying ocean surface characteristics which may have larger planetary albedoes than an ocean with a smooth and homogeneous surface. It also allows for uncertainty in the ocean model itself. For the most part, albedoes in the tropics of the minimum albedo maps, before application of the upper limit cutoff value, were 0.08 to 0.10. The lowest values were observed in May over the North Indian Ocean as 0.06. This lowest value is at the limit of what molecular scattering theory predicts for a daily mean shortwave albedo over a black background with just molecular scattering (after Joseph, 1971).

Over land surfaces a simple reflectance model was not used to eliminate residual cloudiness because the spatial and temporal variability of cloud-free albedo is not directly dependent on the solar zenith angle. Results of the combined ocean and land cloud-free albedoes have been reported on before without the reflectance cut off value over oceans by Vonder Haar and Ellis (1975) and with the cut off value by Ellis (1975).

Zonal mean profiles of albedo and cloud-free albedo for land-plus-ocean, and ocean are shown in Figures 2.1 and 2.2, respectively. For the most part, the large spike in albedo in the intertropical convergence zone (ITCZ) does not appear in the cloud-free albedo of the ocean profile; over the oceans the ITCZ cloudiness effect has been completely removed. Albedo and cloud-free albedo is smaller over the ocean than over the land-plus-ocean. However, differences between cloudy and cloud-free albedo, $\Delta\alpha$, are largest over the oceans, particulary in the middle to high latitudes of each hemisphere. The land surface being brighter than the oceanic surface gives a smaller difference between the cloudy and cloud-free land-plus-ocean profiles than is observed in the ocean profile.

Positions of the mean zonal albedo maxima in the tropics are in agreement with mean brightness composites of Kornfield and Hasler (1969) and relative cloud cover derived from satellite brightness of Miller and Feddes (1971). A narrow spike in albedo at 6N for May is from cloudiness of the ITCZ at 8N in the Pacific and 5N in the Atlantic. In July the peak is located at 9N with the base of the peak spreading north to 30N and south to the equator. This July albedo feature is characteristic of the cloudiness

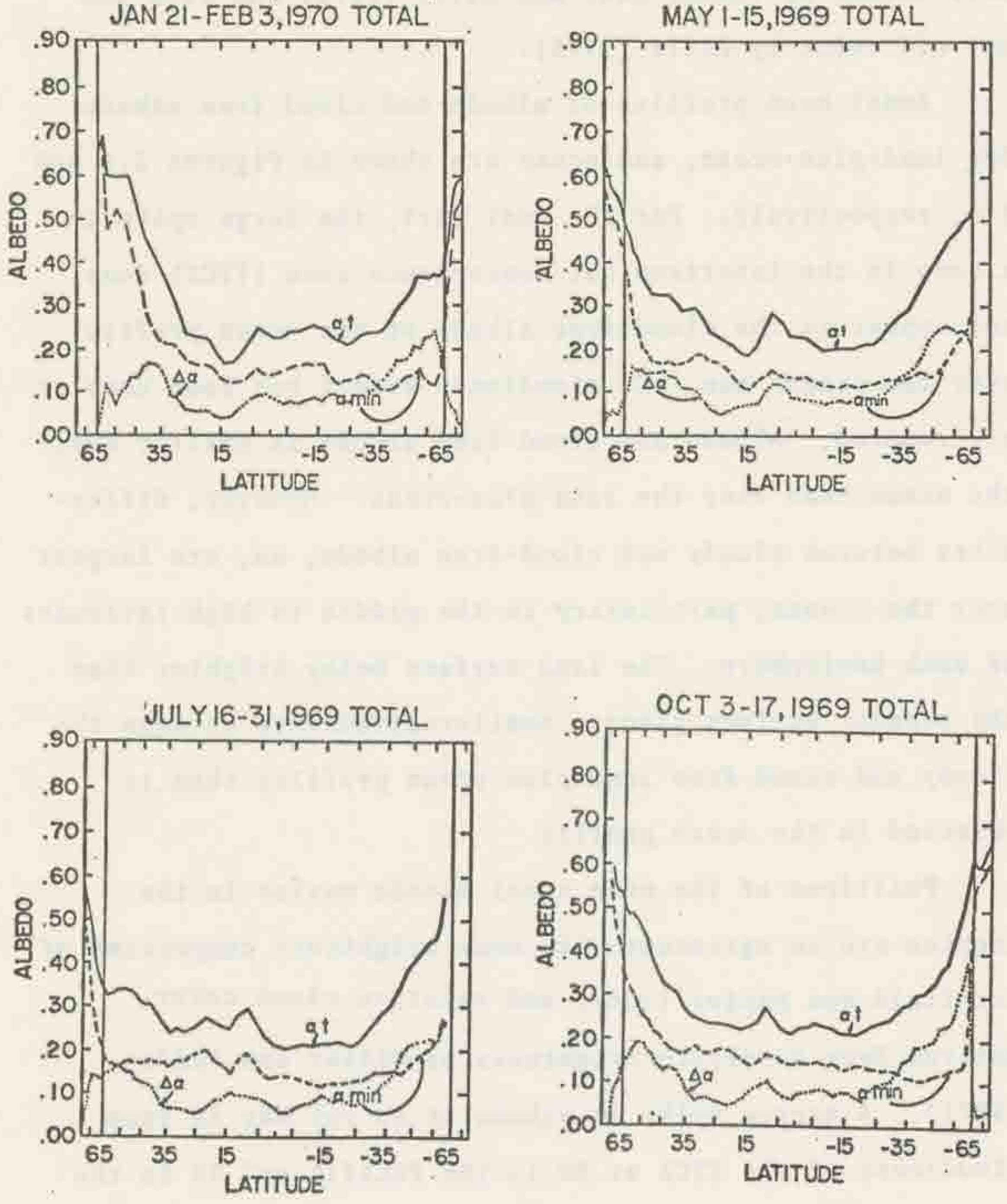

Figure 2.1.: Albedo (α_t) and cloud free albedo (α min) over land-plus-ocean.

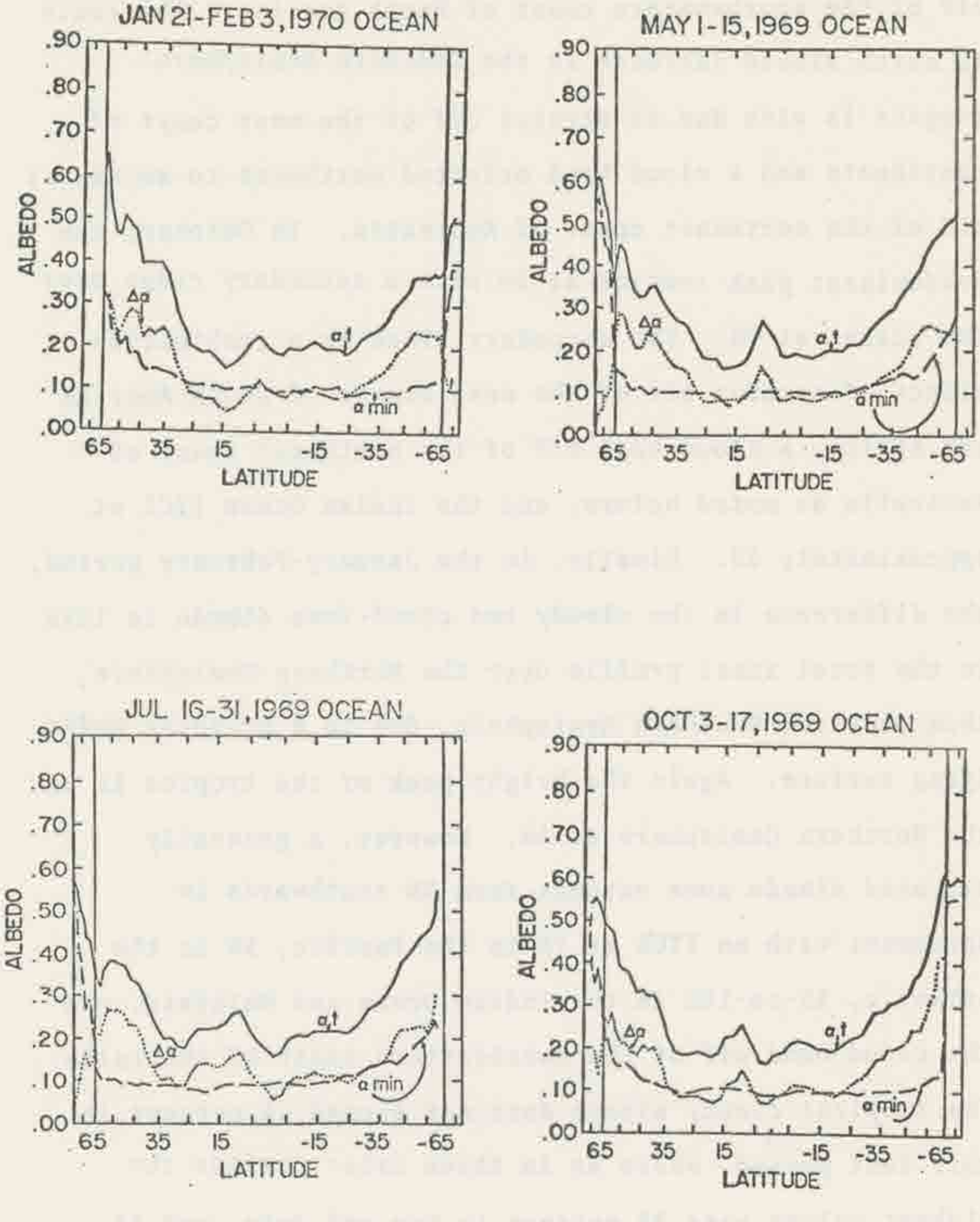

JAN 21-FEB 3, 1970 OCEAN

MAY 1-15, 1969 OCEAN

JUL. 16-31, 1969 OCEAN

OCT 3-17, 1969 OCEAN

Figure 2.2.: Albedo (α_t) and cloud-free albedo (α min) over ocean.

associated with the ITCZ at 9N in the Pacific, and at 10N in the Atlantic, the Southwestern Asian Monsoon and the stratus off of the southwestern coast of North America. The south to north albedo increase in the Southern Hemisphere tropics is also due to stratus off of the west coast of continents and a cloud band oriented northwest-to-southeast off of the northeast coast of Australia. In October, the predominant peak remains at 9N with a secondary ridge over the oceans at 9S. The secondary ridge is a combination effect of stratus off of the west coasts of South America and Africa, a cloud band off of the northeast coast of Australia as noted before, and the Indian Ocean ITCZ at approximately 5S. Finally, in the January-February period, the difference in the cloudy and cloud-free albedo is less in the total zonal profile over the Northern Hemisphere, than over the Southern Hemisphere, due to a brighter underlying surface. Again the bright peak of the tropics is in the Northern Hemisphere at 5N. However, a generally elevated albedo zone extends from 5N southwards in agreement with an ITCZ at 7N in the Pacific, 5N in the Atlantic, 5S-to-10S in the Indian Ocean and Malaysia, and the cloud band off of the Northeastern coast of Australia. The tropical cloudy albedo does not exceed 25 percent in this last period, where as in three other periods the highest values were 28 percent in May and July, and 26 percent in October.

The minimum albedo method as a tool for obtaining a cloud-free albedo is not valid over bright snow and ice surfaces at large solar zenith angles. As was shown by Hauth and Weinman (1968), using visible channel measurements from the Nimbus II MRIR in June 1966 over the Greenland ice cap, bidirectional reflectances from thick clouds were less than from the background surface for relative azimuth angles between sun and satellite greater than 90 degrees. The difference increased at larger satellite zenith angles.

The bidirectional reflectance from clouds has been observed to be less than the background ice cap even at relative azimuth angle less than 90 degrees. Figure 2.3 is a photograph taken from an aircraft over Southern Greenland within one hour of local noon on 22 June, 1975[1]. The slope of the ice cap in the area of the photograph is toward the sun and observer. The relative azimuth angle between sun and observer is approximately 30 degrees. The clouds cast a shadow which are the darkest areas; clouds are brighter; the background ice sheet is brightest.

In latitude zones poleward of 65 degrees in each hemisphere a snow model was applied during the initial data reduction of all Nimbus 3 measured reflectances greater than 0.50 (Raschke et al., 1973b). That model assumed diffuse reflection over bright snow and ice surfaces.

---

[1] Photograph taken by Dr. Stephen Cox, Department of Atmospheric Science, Colorado State University.

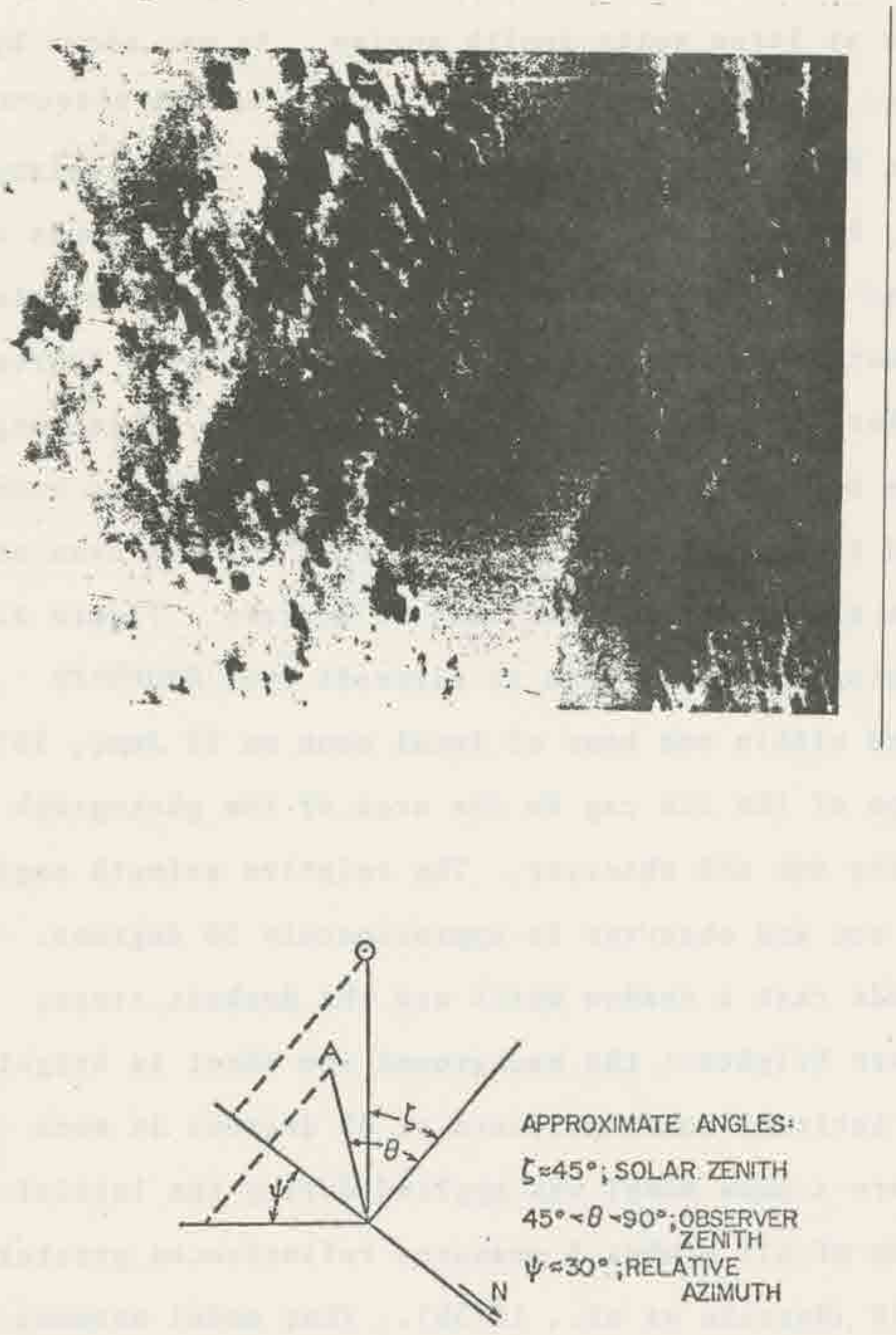

Figure 2.3.: Photograph from aircraft showing partial cloud cover above Greenland's ice sheets on 22 June 1975 at 1600 GMT.

Cloud reflectances were not distinguishable from background reflectances. If such a model could isolate clouds over the bright surface, it is quite likely that these cloud albedoes would, after angular corrections, be lower than the cloud-free albedoes. Thus all cloud-free albedoes poleward of 65 degrees in latitude in each hemisphere derived by the minimum method are not to be considered as cloud-free albedoes.

Annual profiles of albedo and cloud-free albedo were computed from the four semi-monthly profiles by assuming each period to be representative of a season and weighting it in the annual average by the mean season solar insolation. Annual profiles for total (land-plus-ocean), ocean and land from Nimbus 3 data are shown in Figure 2.4. The mean position of the cloudiness associated with the ITCZ at 7N-to-10N is apparent in both the total and ocean albedo profiles. An albedo of 23 percent in the ITCZ of the ocean albedo profile and the larger area of land surface in the Northern Hemisphere contribute to a brighter Northern Hemisphere. Oceanic albedo is essentially the same in corresponding latitude zones of each hemisphere except at the latitude of the ITCZ.

The annual land albedo profile shows a general increase in cloudy albedo from 35S to 65N latitudes. The cloud-free land albedo profile shows a lesser albedo increase from south-to-north, except for the 15N-to-30N zone, which shows a larger albedo increase. This zone includes the Sahara

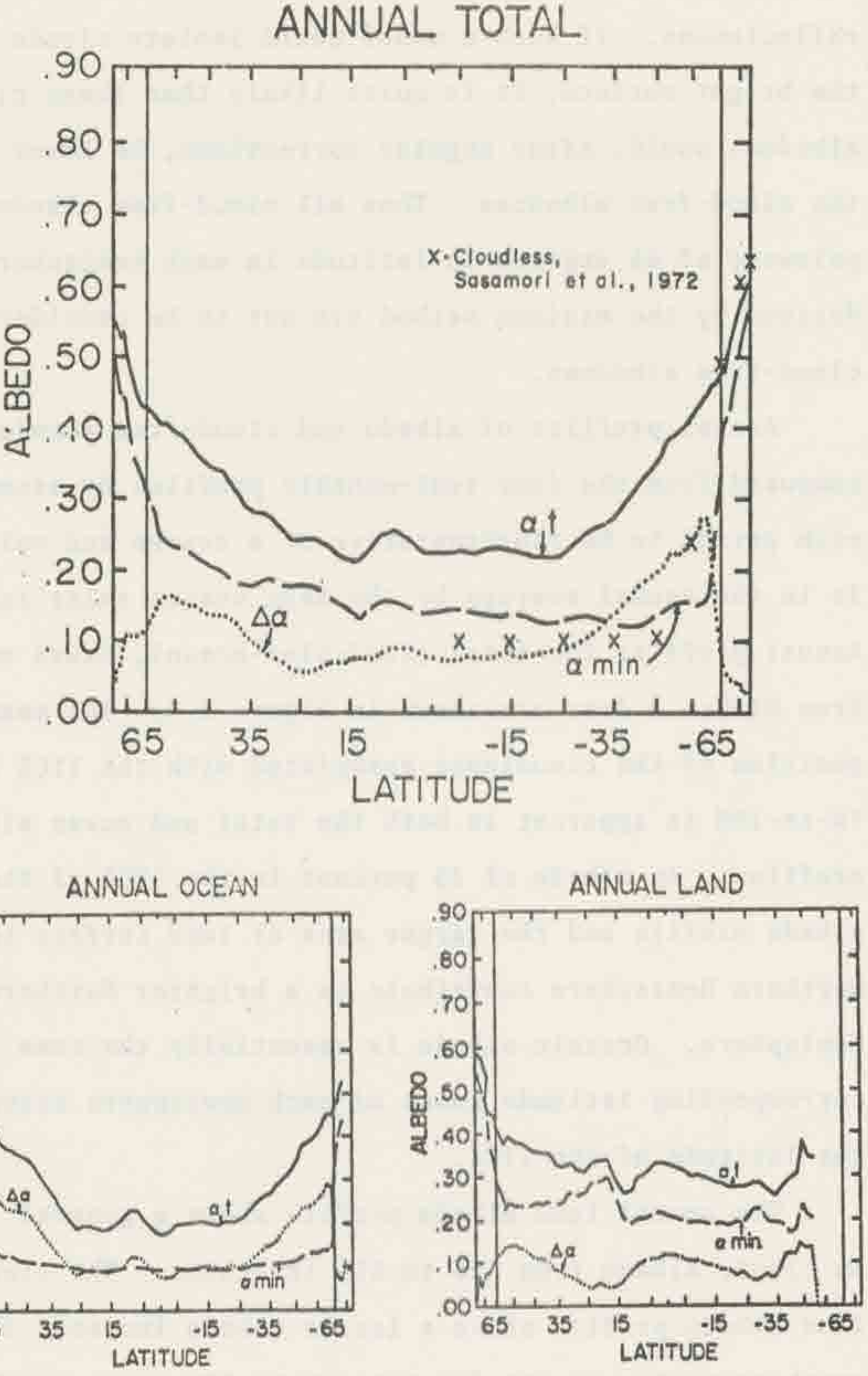

Figure 2.4.: Annual albedo (α_t) and cloud-free albedo (α min) over land-plus-ocean, ocean and land.

Desert and Saudi Arabia, which are bright land surfaces. The latitude of largest cloud-free albedo occurs at 20N. The difference between cloudy and cloud-free albedoes over land ($\Delta\alpha$) is smallest in the 15N-to-25N zone, a zone of subtropical deserts which are nearly cloud-free, except during the period of the summer monsoon.

Cloudless albedo of the Southern Hemisphere from Sasamori et al (1972) is plotted on the land-plus-ocean albedo profile of Figure 2.4. The Nimbus 3 cloud-free albedo is greater by 2 to 3 percent from the equator-to-50S latitude zone. In the 50S-to-South Pole zone their values are considerably larger than the Nimbus 3 values. Undoubtedly this difference is due to differences between the two results in the equatorward extension of the sea ice around the Antarctica Continent and the albedo of the ice sheets.

Northern and Southern Hemisphere cloud-free albedoes from Nimbus 3 data are compared to cloudless albedo values of London (1957) and Sasamori et al (1972) for the Northern and Southern Hemisphere, respectively, in Table 2.4. The Nimbus 3 cloud-free values are larger in all seasons except for the Southern Hemisphere winter value which is identical to the value of Sasamori et al. Annual global cloud-free albedo from Nimbus 3 data is 16.9 percent as compared to a global value of 14.1 percent from their combined hemisphere values. London and Sasamori (1971) give an annual global value of 15 percent. This suggests that the 14.1

Table 2.4 - Cloud free albedo (percent)

	Winter	Spring	Summer	Fall	Annual
London, 1957 (90N-0)	17.3	15.0	13.5	13.4	14.7
Nimbus 3 (90N-0) (65N-0)	19.1 19.1	18.7 16.9	18.2 16.9	17.4 17.0	18.3 17.2
Sasamori et al (1972) 90S-0	13.8	14.0	14.8	11.1	13.6
Nimbus 3 (90S-0) (65S-0)	13.8 13.8	16.3 13.6	16.6 13.7	13.7 13.4	15.5 13.7

percent value should be considered as being too low. The difference between the Nimbus 3 data results and results of these other studies might be attributed to inadequate aerosol scattering to space and inaccurate land and ocean surfaces albedoes in the other studies, and residual cloudiness in the cloud-free albedoes of the present study. The true value of the annual global cloud-free albedo most likely falls between their value and the value of the present study.

2.3.2 Cloud Free Emitted Flux

The cloud-free emitted flux may be obtained in a fashion similar to cloud-free albedo by selecting the largest flux value at each grid area over each semi-monthly period. The concept assumes that without clouds a larger flux is measured from space with a standard atmosphere of decreasing temperature with increasing height above ground. Clouds are taken to be more opaque to terrestrial infrared and near infrared flux (3 to 30 μm) than other constituents are, and thus less terrestrial flux is emitted to space with clouds than without them.

It seemed prudent to test the empirical formula, used by Raschke et al (1973b) to extract total longwave radiance from the four Nimbus 3 IR channel radiances, for bias error with and without cloud cover. The four IR channels measure radiances in the 11μm window, the 15 um CO_2 absorption band and two water vapor absorption bands, one of which detects emission largely from lower tropospheric water vapor. In the presence of middle and upper tropospheric opaque cloud cover the spectral composition of emitted flux to space will be different than cloud-free emission, principally because of the absence of emission from lower tropospheric water vapor. If the regression formula did not adequately consider this, then a bias error will be present in the difference between cloudy and cloud-free total longwave radiances.

A spectral IR model of Cox et al., (1976) was applied to a model atmosphere to compute channel radiances. The regression formula of Raschke et al., was applied to each model computed channel radiance to determine total broadband longwave radiance. The regression formula results were compared with broadband results of total longwave radiance. This comparison showed that the least squares regression formula handled the spectral radiances adequately both with and without middle tropospheric clouds, so that no significant bias error was introduced into the total longwave flux. (The model analysis appears in Appendix B).

An exception to using a "maximum" IR value at each grid point within a semi-monthly period is the case of clouds at the top of a lower tropospheric temperature inversion overlaying a cold surface. According to Vowinckel and Orvig (1970) such a condition is frequent and persistent over large areas of the Arctic particularly during winter. Large anticyclonic areas show a substantial increase in radiation loss to space when clouds of this type are present because of higher temperature at cloud top than at the earth's surface. During the winter, in absence of appreciable solar flux, overcast low and middle clouds contribute to a larger radiation flux loss to space in the Arctic than during cloud-free conditions. As in the cloud-free albedo portion of this study, determining cloud-free IR by a "maximum" method will be limited to the latitude zone 65N-to-65S, inclusive.

Besides limiting the cloud-free zonal emitted flux profile to being the zonal average of "maximum" IR values at each grid area, all maximum IR values over ocean regions were excluded from the zonal mean whenever the ocean reflectance model, as applied to minimum albedoes, indicated the presence of clouds. This "throw out" criterion follows from a consideration that if, over some time interval, the minimum albedo is not a cloud-free albedo, then the maximum IR over the same time interval is not a cloud-free IR.

Zonal mean meridional profiles of cloudy and cloud-free IR are shown for each semi-monthly period in Figures 2.5 and 2.6 for land-plus-ocean and ocean, respectively. Notable in the May and July cloud-free profiles is the dip in flux values at the ITCZ. The dip in the July ocean profiles amounts to 25 wm^{-2}. This dip over the oceans at the mean position of the ITCZ may be a result of colder ocean surface temperature, or increased absorption and emission at a lower temperature due to abundant water

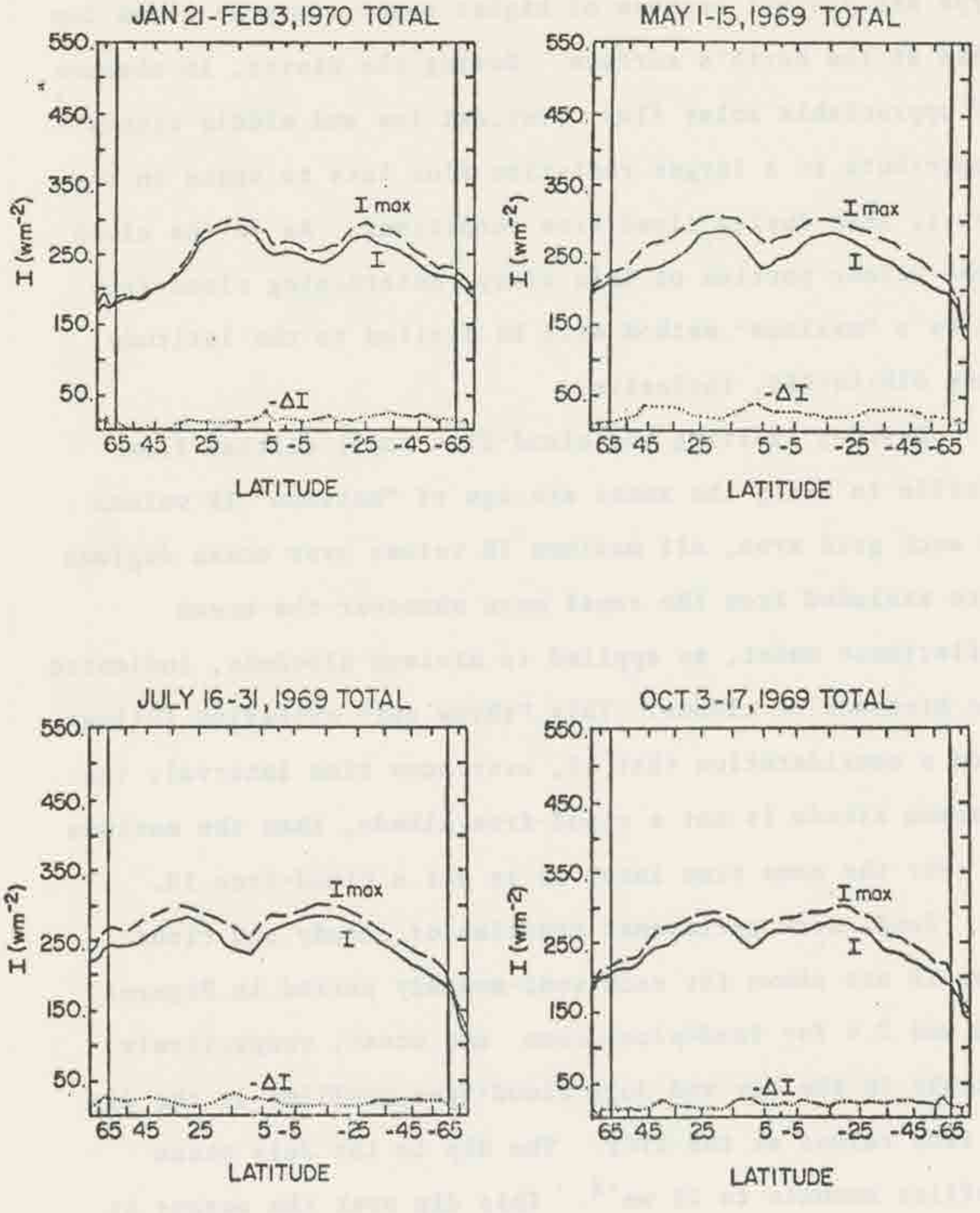

Figure 2.5.: Longwave flux (I) and cloud-free longwave flux (I max) over land-plus-ocean.

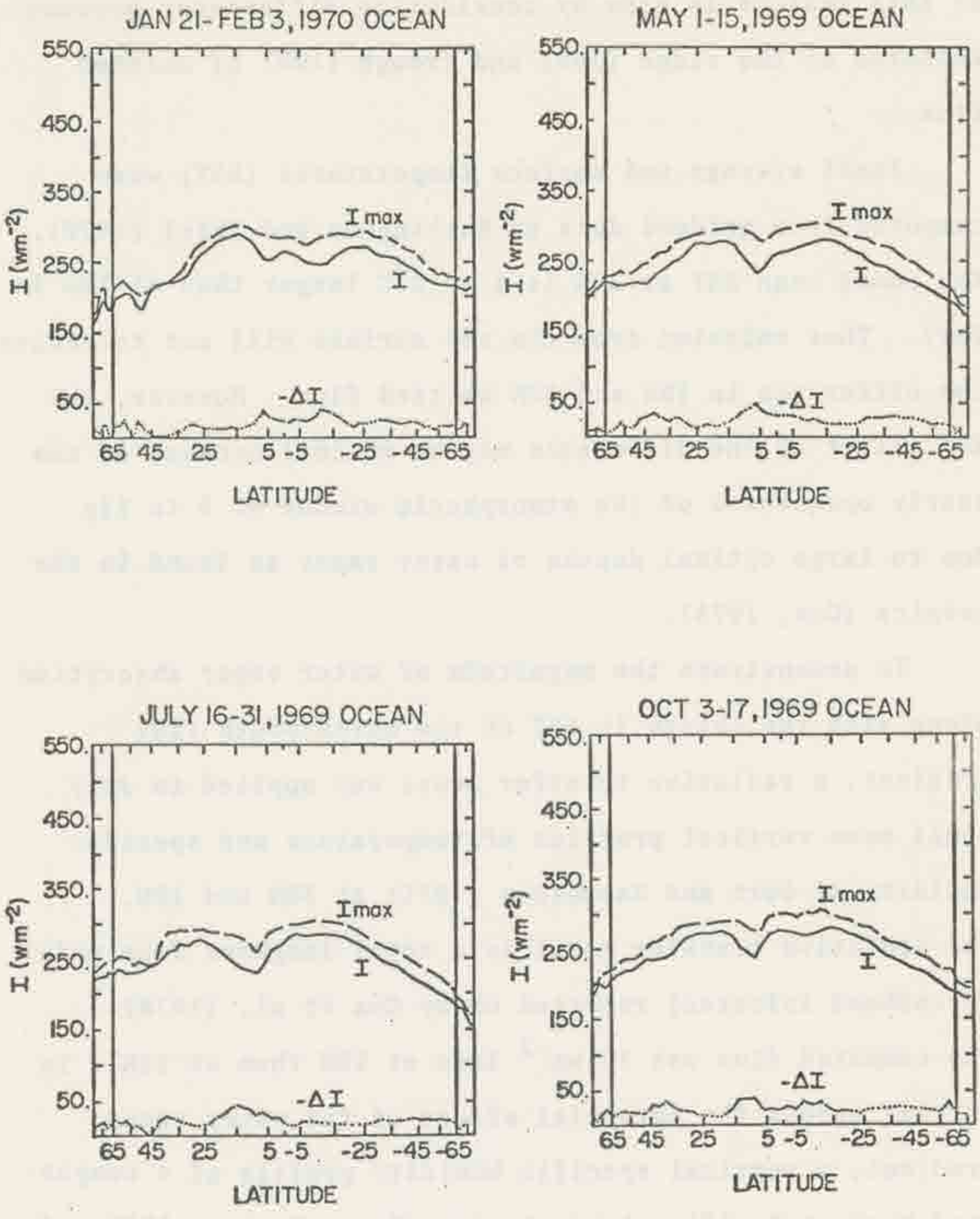

Figure 2.6.: Longwave flux (I) and cloud-free longwave flux (I max) over oceans.

vapor, or cloudiness remaining in the profile. An analysis of this feature is made by considering differences between features at the ridge (30N) and trough (10N) of emitted flux.

Zonal average sea surface temperatures (SST) were computed from gridded data of Washington and Thiel (1970). The zonal mean SST at 10N is 1 to 2°C larger than at 30N in July. Thus emission from the sea surface will act to reduce the difference in 10N and 30N emitted flux. However, the SST effect on the difference may be minimal because of the nearly opaqueness of the atmospheric window at 8 to 12μ due to large optical depths of water vapor as found in the tropics (Cox, 1975).

To demonstrate the magnitude of water vapor absorption along with the change in SST on the north-south flux gradient, a radiative transfer model was applied to July zonal mean vertical profiles of temperature and specific humidity of Oort and Rasmusson (1971) at 30N and 10N. The radiative transfer model is a total longwave flux model (broadband infrared) reported on by Cox et al. (1976). The computed flux was 10 wm^{-2} less at 10N than at 30N. To further assess the potential effect of the water vapor gradient, a vertical specific humidity profile of a composited Western Pacific cloud cluster (Gray et al ., 1975 and Frank, 1976) was inserted into the radiative calculations. This profile is to be considered an extremely moist atmosphere with a good portion of the water vapor excess being in the upper troposphere. This new computed value was 23 wm^{-2} less than the previously computed flux value at 30N. Thus the water vapor absorption-emission contribution to the north-to-south flux decrease appears to lie somewhere between 10 wm^{-2}, a space-time mean and zonal mean for land-plus-ocean, and 23 wm^{-2}, a time mean of very moist cloud clusters.

Finally, the existence of residual cloudiness, which was not removed by application of this maximum IR method, must be considered. Effects of optically thin cirrus cloudiness, which is not significantly detectable in the shortwave portion of the solar spectrum but is detectable in the IR, may not have been eliminated over the ITCZ. Theoretical work of Zdunkowski et al., (1965 and 1971) indicates that cirrus-cloud, invisible from the ground (or haze), can reduce the total longwave flux emitted to space by 10 percent (25 wm^{-2}). He further states that his results are consistent with those from radiometer measurements made in tropical regions (the radiometer measurements show a sudden decrease in the infrared total net outgoing flux in the upper troposphere). The extent and persistence of such cloudiness is not known but its presence could add to the magnitude of flux decrease in the cloud free profile. It is reasonable to assume that as much 10 wm^{-2} of the cloud-free flux profile dip at the ITCZ is caused by residual "haze" or thin cirrus cloudiness.

The cloud-free profile nearly coincides with the cloudy profile in the latitude zone 37N-to-55N for January-February. Even though the span is 13 days, at many grid areas there are less than 8 samples in time. Also the greater portion of the Pacific Ocean poleward of 45N was not sampled at all. Thus, the utility of the January-February period for this type of study certainly must be questioned. Over cold land surfaces the coincidence or near coincidence of the two profiles is entirely reasonable but not over an ocean surface.

Annual mean profiles for land-plus-ocean, ocean, and land were computed by averaging the four semi-monthly periods (Figure 2.7). As in the cloudy albedo, the cloudy IR shows the mean position of the ITCZ to be at 7N. The magnitude of the ITCZ dip is considerably reduced in the annual mean because of averaging the north-south migration of the zone with season. It is halved in the annual profiles from July values. Similarly, the albedo increase due to the ITCZ over oceans is halved in the annual mean from a magnitude of 5 to 2.5 percent.

The validity of the cloud-free emitted flux can only be suggested by radiative transfer calculations. Schneider (1972) applied radiative transfer calculations to a model atmosphere of the globe to obtain a cloud-free total infrared flux of 279 wm^{-2}. Using the same model atmosphere and applying a radiative transfer model as discussed in Cox et al., (1976), the cloud-free flux was

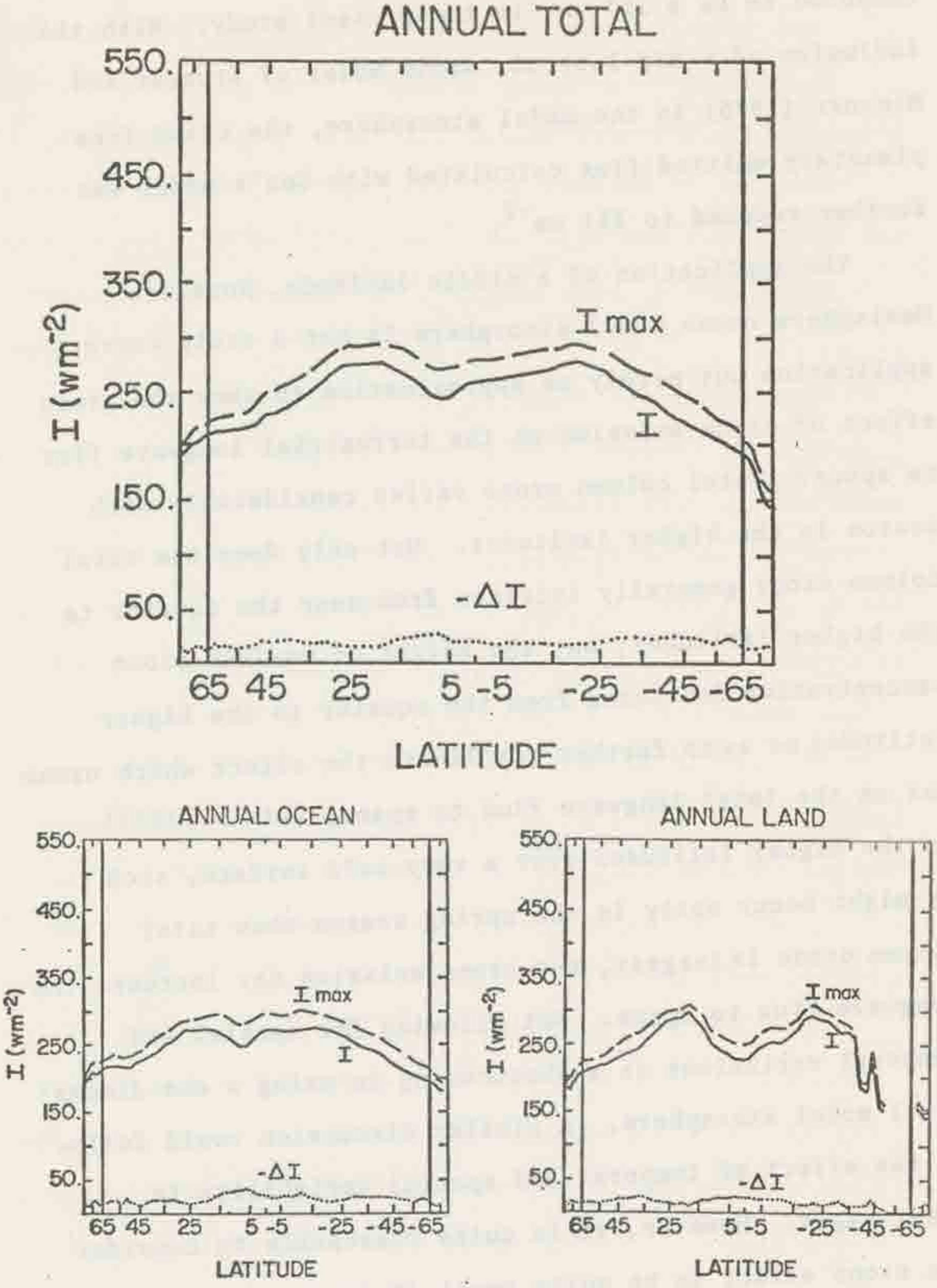

Figure 2.7.: Annual longwave flux, (I) and cloud-free longwave flux, (I max) over land-plus-ocean, ocean and land.

computed to be a 257 wm^{-2} in the present study. With the inclusion of a mid-latitude ozone model of Krueger and Minzner (1976) in the model atmosphere, the cloud-free planetary emitted flux calculated with Cox's model was further reduced to 251 wm^{-2}.

The application of a middle latitude, Northern Hemisphere ozone model atmosphere is not a truly correct application but merely an approximation to show the gross effect of ozone emission on the terrestrial longwave flux to space. Total column ozone varies considerably with season in the higher latitudes. Not only does the total column ozone generally increase from near the equator to the higher latitudes, but the height of maximum ozone concentration decreases from the equator to the higher latitudes so as to further complicate the effect which ozone has on the total longwave flux to space, Dutsch (1971). In the higher latitudes over a very cold surface, such as might occur early in the spring season when total column ozone is largest, the ozone emission may increase the longwave flux to space. Not allowing for spatial and temporal variations is a shortcoming in using a one-dimensional model atmosphere. A similar discussion could follow on the effect of temporal and spatial variability in water vapor. However, it is quite reasonable to consider the ozone effect to be quite small (3 percent or less) in light of what will later be shown to be the cloud effect.

The global and annual mean value derived from the "maximum IR" method is 261 wm^{-2}. This value is within 4 wm^{-2}, or 1.5 percent, of the model atmosphere calculations using Cox's model without an ozone profile. The semi-monthly global satellite determined values range from 268 wm^{-2} in May to 251 wm^{-2} in the January-February period. Again a severe sampling limitation both in space and time of the latter period places that value in question. The next lowest value is 261 wm^{-2} in October. A recomputation of the mean, excluding the January-February period, yields a global mean value of 265 wm^{-2}. This new value is 14 wm^{-2} less than Schneider's, 8 wm^{-2} larger than results with Cox's model using the same model atmosphere, and 14 wm^{-2} larger than results computed from Cox's model with inclusion of a mid-latitude ozone profile. Quite apparent is that results of the "maximum IR" method are in the middle of the theoretical calculations. Thus it is concluded that the maximum IR method gives results which are reasonable.

3. CLOUD EFFECTS ON THE PLANETARY RADIATION BUDGET

In this section the effects of "todays" cloudiness in "todays" planetary radiation budget are examined. By "today" is meant the period for which satellite radiation budget measurements have been composited in this study, 1964 through 1971.

The heat budget of the planet is the long term control of the planet's climate. The planetary radiation budget is a part of the global heat budget. The role that clouds play in the radiation budget partially defines their role in the global heat budget. A discussion of the cloud role in the global heat budget should go concurrently with, or be preceeded by a discussion of its role in the planetary radiation budget. Furthermore, the role of cloudiness in climate change, commonly referred to as cloud feedback processes, can be considered only after gaining thorough knowledge of its role in the global heat budget. This section will examine the single role of cloudiness in today's planetary radiation budget.

The cloud amount sensitivity may be defined as equation 3.1:

$$\frac{\partial N}{\partial Ac} = \frac{\partial Ab}{\partial Ac} - \frac{\partial I}{\partial Ac} \qquad (3.1)$$

by operating on equation (2.1) with $\frac{\partial}{\partial Ac}$, a local derivative taken with respect to fractional cloud amount, Ac.

This derivative, or sensitivity factor, has been discussed in theoretical studies by Schneider (1972) and more recently by Cess (1976). This sensitivity factor, derived from the present diagnostic study, is compared to their theoretical results in the next major section. The cloud effect in the planetary radiation budget, ΔN, for "todays" radiation budget climatology is examined by differencing "todays" planetary radiation budget with a cloud-free, non-equilibium radiation budget. It is mathematically defined as:

$$\Delta N = \Delta Ab - \Delta I \qquad (3.2)$$

where: $\Delta N \equiv \Delta Ac \frac{\partial N}{\partial Ac}$

or from equation (2.1)

$$\Delta N = -(S\ \Delta\alpha + \Delta I) \qquad (3.3)$$

with a consideration that the solar constant does not vary with changes in cloudiness. The ΔN should be thought of as the radiative forcing in the heat budget which would exist with an instantaneous removal of all clouds. It will be examined on the zonal mean and global space scales, and on a seasonal time scale.

3.1 Zonal Mean Cloud Effect

The $\Delta\alpha$ and ΔI profiles, where Δ indicates cloudy minus cloud-free, were shown in Figures 2.1, 2.2, 2.4, 2.5, 2.6, and 2.7. Resulting profiles of ΔN, the cloudy planetary radiation budget minus the cloud-free radiation budget, are Figures 3.1 and 3.2 for total land-plus-ocean and ocean, respectively, for each semi-monthly period. Figure 3.3 shows the mean annual ΔN profile of total land-plus-ocean, ocean, and land.

All of the profiles show that ΔN is less than or equal to zero in all latitude zones except for occasional positive values in polar zones, zones comprising 10 percent or less of the global area. A negative ΔN indicates that clouds have a larger effect on ΔAb, the absorbed solar flux, than on ΔI, the emitted terrestrial flux. Largest negative values are in the hemisphere of solar declination. The values become more negative going from equator to approximately 60 degrees latitude in each hemisphere.

Contribution to ΔN from the two terms on the right side of equation (3.3) may be determined by examining the zonal profiles of $\Delta\alpha$ and ΔI in the previous section. Now $\Delta\alpha$ of Figures 2.1 and 2.2 increases away from the equator in each hemisphere in all seasons except for the Northern Hemisphere winter total land-plus-ocean profile. The profiles of ΔI, Figures 2.5 and 2.6, show no systematic change from equator poleward. Therefore, the negative increase in ΔN with latitude in the hemisphere of solar declination is

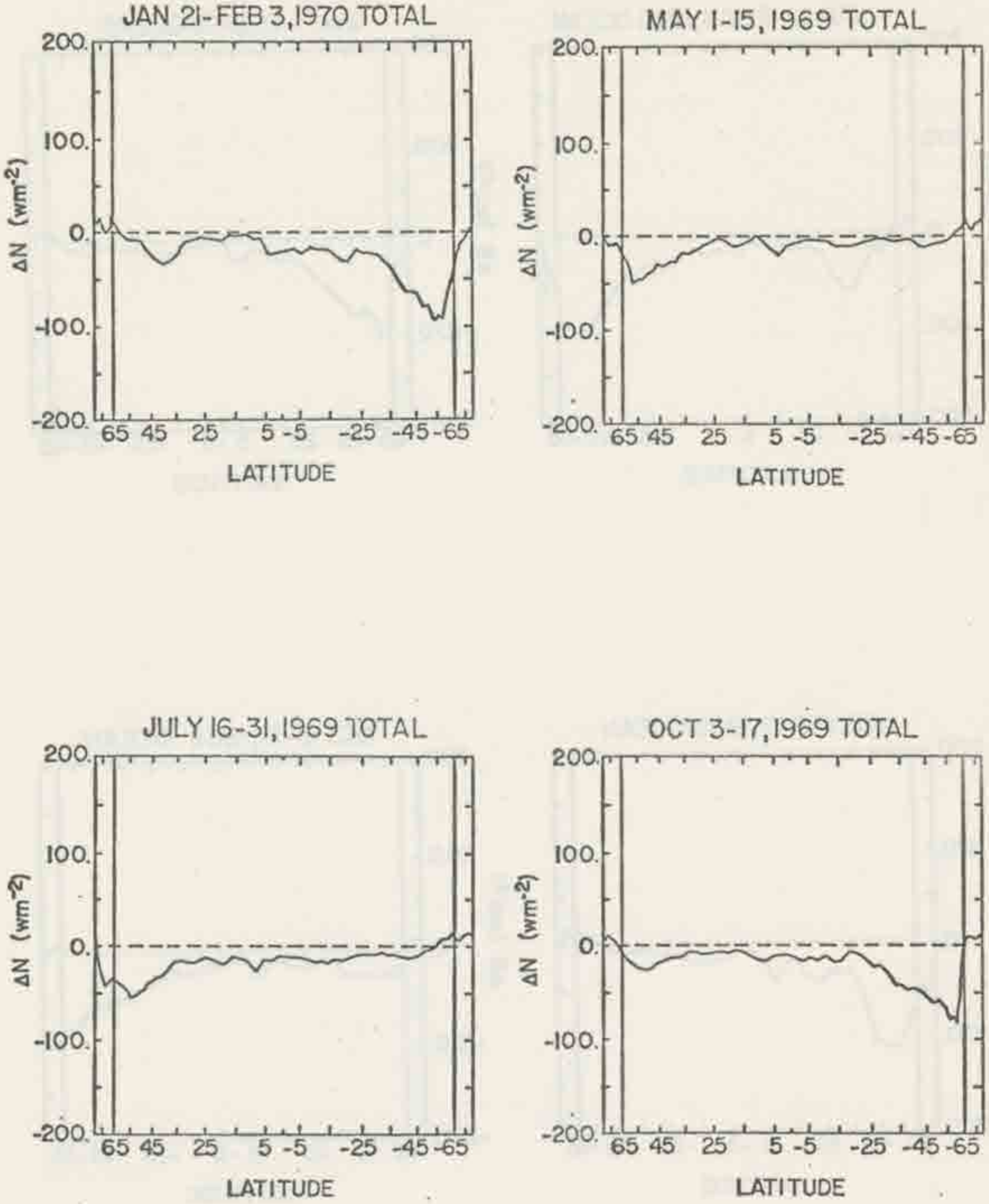

Figure 3.1.: Cloud effect on net flux for land-plus-ocean.

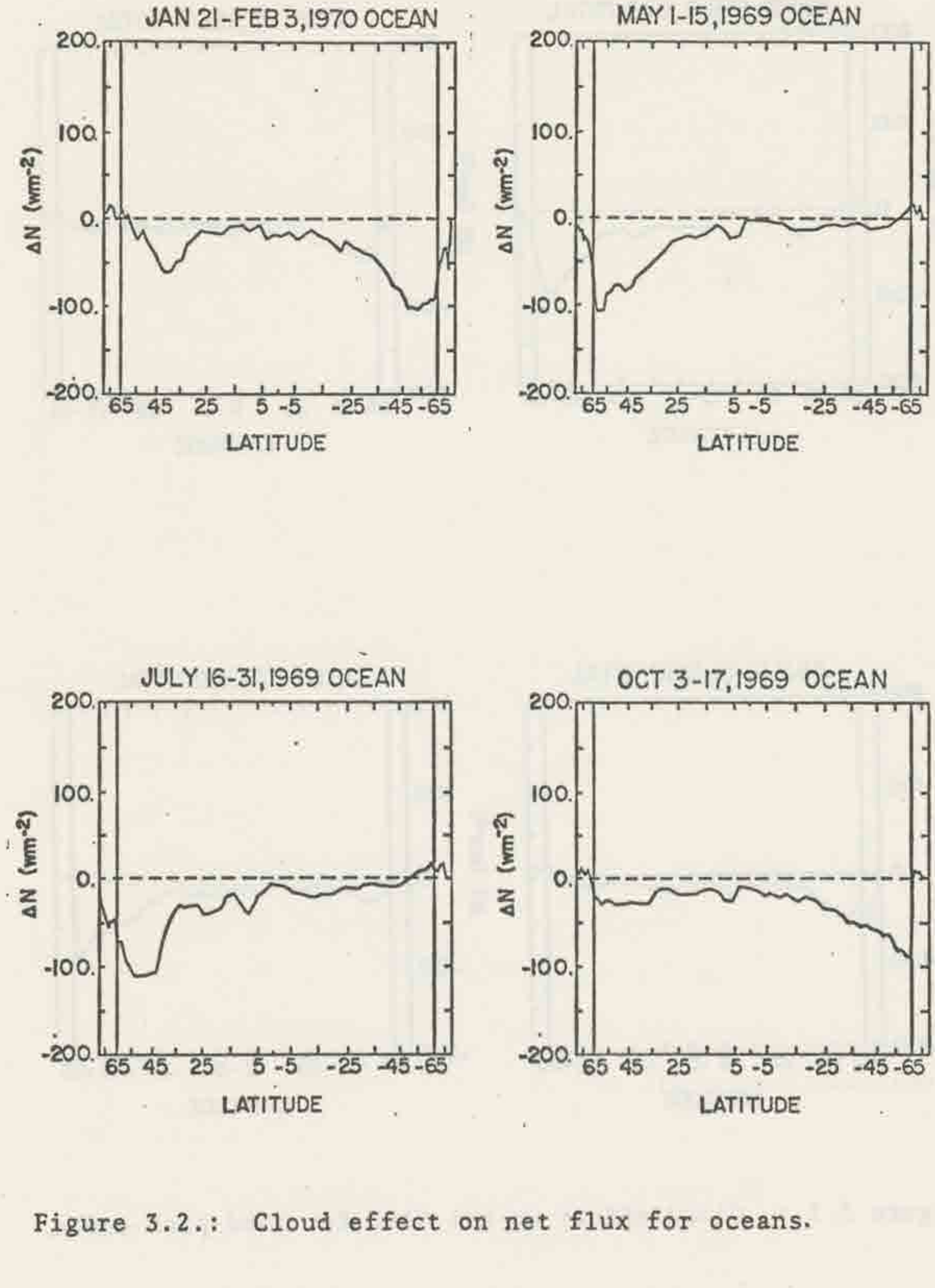

Figure 3.2.: Cloud effect on net flux for oceans.

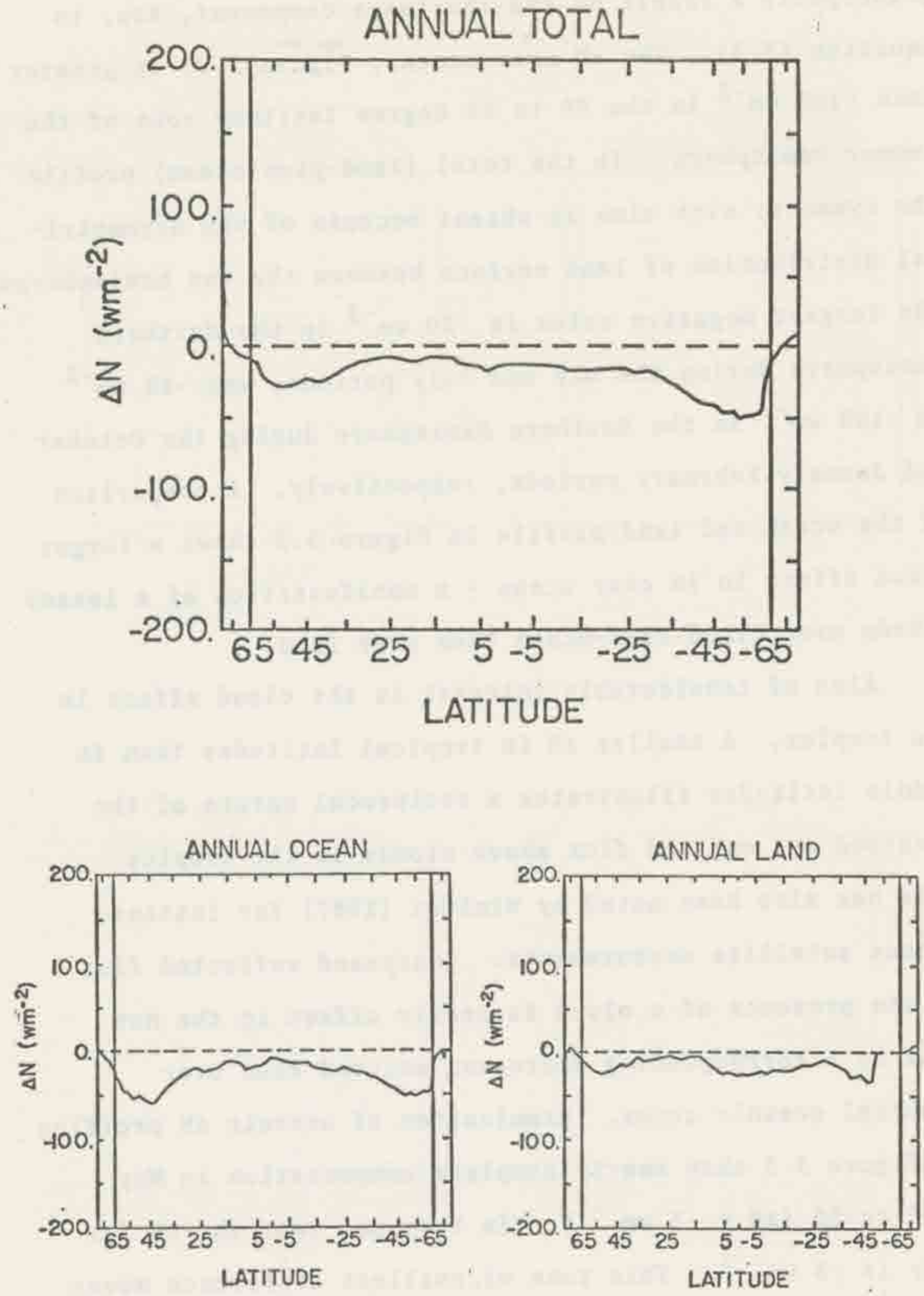

Figure 3.3.: Annual cloud effect on net flux over land-plus-ocean, ocean and land.

principally a result of the shortwave component, $s\Delta\alpha$, in equation (3.3). The ΔN over oceans, Figure 3.2, is greater than -100 wm^{-2} in the 50 to 60 degree latitude zone of the summer hemisphere. In the total (land-plus-ocean) profile the symmetry with time is absent because of the asymmetrical distribution of land surface between the two hemispheres. The largest negative value is -50 wm^{-2} in the Northern Hemisphere during the May and July periods, and -80 wm^{-2} to -100 wm^{-2} in the Southern Hemisphere during the October and January-February periods, respectively. A comparison of the ocean and land profile in Figure 3.3 shows a larger cloud effect in ΔN over ocean - a manifestation of a lesser albedo over cloud-free-ocean than over land.

Also of considerable interest is the cloud effect in the tropics. A smaller ΔN in tropical latitudes than in middle latitudes illustrates a reciprocal nature of the absorbed and emitted flux above clouds in the tropics. This has also been noted by Winston (1967) for instantaneous satellite measurements. Increased reflected flux in the presence of a cloud is nearly offset in the net flux by a corresponding decreased emitted flux over tropical oceanic zones. Examination of oceanic ΔN profiles in Figure 3.3 show nearly complete compensation in May at 0-to-5S (ΔN = -3 wm^{-2}). In the same zone the ΔN for July is -8 wm^{-2}. This zone of smallest difference moves northward to 0-to-5N in October (-8 wm^{-2}); in January-

February it is at 5N-to-15N. All of these minimum differences occur in the hemisphere opposite the solar declination where incoming solar flux and $S\Delta\alpha$ decrease to nearly balance ΔI.

Adjoining the minimum ΔN is a rather abrupt increase to a larger negative ΔN value. The position of this increase is precisely the mean position of the ITCZ as identified in the preceeding section. The largest increase in the ITCZ anomaly, over what would exist with a smooth north-to-south profile across the zone, occurs in July. It is approximately $25\ \mathrm{wm}^{-2}$. Now this value is of the same magnitude as the observed decrease in cloud-free IR over the ITCZ (Figure 2.6). As discussed in the previous section, this anomalous dip in cloud-free IR may be accounted for by both the presence of abundant water vapor and a haze type, or nearly invisible type, of cirrus cloudiness which affects only the cloud-free IR.

In polar zones during the polar night, ΔN is positive. The presence of clouds act to decrease the emitted flux loss to space. This holds true except for low and middle cloudiness formed just above a surface inversion in which case the opposite may be true. If the vertical lapse of temperature from the ground to some height above ground is greater than zero, $\frac{\partial T}{\partial T} > 0$, then clouds at the inversion top will increase the emitted flux loss to space. Over ice free oceans, such an inversion may not be present because the free air temperature is most often lower than the temperature of the ocean surface. A crossover to positive ΔN occurs, as a valid result, at latitudes 52S and 57N in the July and January-February ocean profiles, respectively. It cannot be ascertained that ΔN should remain positive all the way to the polar night pole because of the possible existence of strong surface inversions overlying ice and snow surfaces. If the effective cloud tops are warmer than the ground, then ΔN would be negative in the polar night zone.

The annual mean profiles in Figure 3.3 show that for all latitudes within the 65N-to-65S zone, ΔN is negative. The minimum cloud effect in the total land-plus-ocean profile is -7 wm^{-2} at 12N with a maximum value of -49 wm^{-2} at 55S. Asymmetry in ΔN between the two hemisphere's is largely the result of asymmetry in land mass distribution. The annual mean ocean profile is quite symmetrical about the equator. Thus, the cloud effect on the planetary radiation budget over oceans appears to be the same in both hemispheres. The annual mean ΔN profile over land surface lacks symmetry between hemispheres largely because of differences in land surface albedo. In the zone 30N-to-15N, ΔN is less than 10 wm^{-2} because of bright and relatively cloud-free land surfaces.

3.2 Global and Hemispherical Mean Cloud Effect

The global and hemispherical mean cloud effects are summarized in Table 3.1. Seasonal ΔN values were computed by applying a seasonal solar insolation to equation (3.3) with the semi-monthly albedo and emitted flux values both taken as being representative of seasonal values. The annual value is merely the average of the four seasonal values. The values in Table 3.1 are not quite global and hemispherical, but are limited to 65N-65S and 0-65 degrees latitude, respectively, because of uncertainty in the cloud effect polewards of 65 degrees latitude.

The annual mean global value is -20 wm^{-2} indicating that global cloudiness has a larger effect on absorbed solar flux than on emitted terrestrial flux. Instantaneous removal of clouds over the 65N-65S latitude zone would have an immediate effect of a net gain of 20 wm^{-2} in the global planetary radiation budget. The cloud effect is 9.5 wm^{-2} larger in the Southern Hemisphere than the Northern Hemisphere or, in other words, the Northern Hemisphere's cloud effect is only 62 percent of the Southern Hemisphere's.

The cause of the asymmetry between the values of the two hemisphere's is elucidated by Table 3.2. Each latitude zone is considered to be composed entirely of ocean so that over a 65N-65S oceanic zone an annual mean ΔN of -30.6 wm^{-2} would be observed. This value is 1.5 times larger than the land-plus-ocean value of Table 3.1. Thus, whether clouds are over land or water is of significant concern in studying the cloud effect on the planetary radiation budget. Furthermore, the difference in annual means of the two hemispheres in Table 3.2 is less than 4 wm^{-2} and of

Table 3.1 - Cloud effect in net flux (ΔN) for land-plus-ocean (wm^{-2})

	MAM	JJA	SON	DJF	ANNUAL
65N-65S	-14.0	-16.0	-23.5	-26.7	-20.0
65N-0	-14.2	-23.5	-12.0	-11.3	-15.3
65S-0	-13.8	- 8.5	-34.9	-42.0	-24.8

Table 3.2 - Cloud effect in net flux (ΔN) for oceans (wm^{-2})

	MAM	JJA	SON	DJF	ANNUAL
65N-65S	-30.1	-29.2	-30.0	-33.2	-30.6
65N-0	-44.8	-48.2	-18.0	-19.1	-32.5
65S-0	-15.3	-10.2	-42.0	-47.2	-28.7

opposite sign to the difference in annual mean hemispherical totals of Table 3.1. The difference between ocean values is most likely not significant or real in light of limited ocean sampling in higher latitudes of the Northern Hemisphere, but the difference in annual hemispherical values of Table 3.1 is undoubtedly due to differences in land-ocean distribution between the hemispheres. Also of interest is the variation in global values with season. For the land-plus-ocean values this variation amounts to 12.7 wm^{-2} whereas over oceans it is 4 wm^{-2} indicating that seasonal variations in ΔN are principally a result of asymmetry in land and ocean distribution. The season with largest global cloud effect is DJF. Largest negative values appear in the summer season with the southern summer value being nearly twice as large as the northern summer value.

3.3 Seasonal Variations In the Cloud Effect

Seasonal variations, are examined both qualitatively and quantitatively in zonal profiles and global mean values.

3.3.1 Zonal Variations

Time-latitude displays of zonal mean profiles of albedo, longwave emitted flux and net flux are shown in Figure 3.4. These are from the composited 29 months set of satellite measurements discussed in Ellis and Vonder Haar (1976). Also shown in Figure 3.4d is a time-latitude

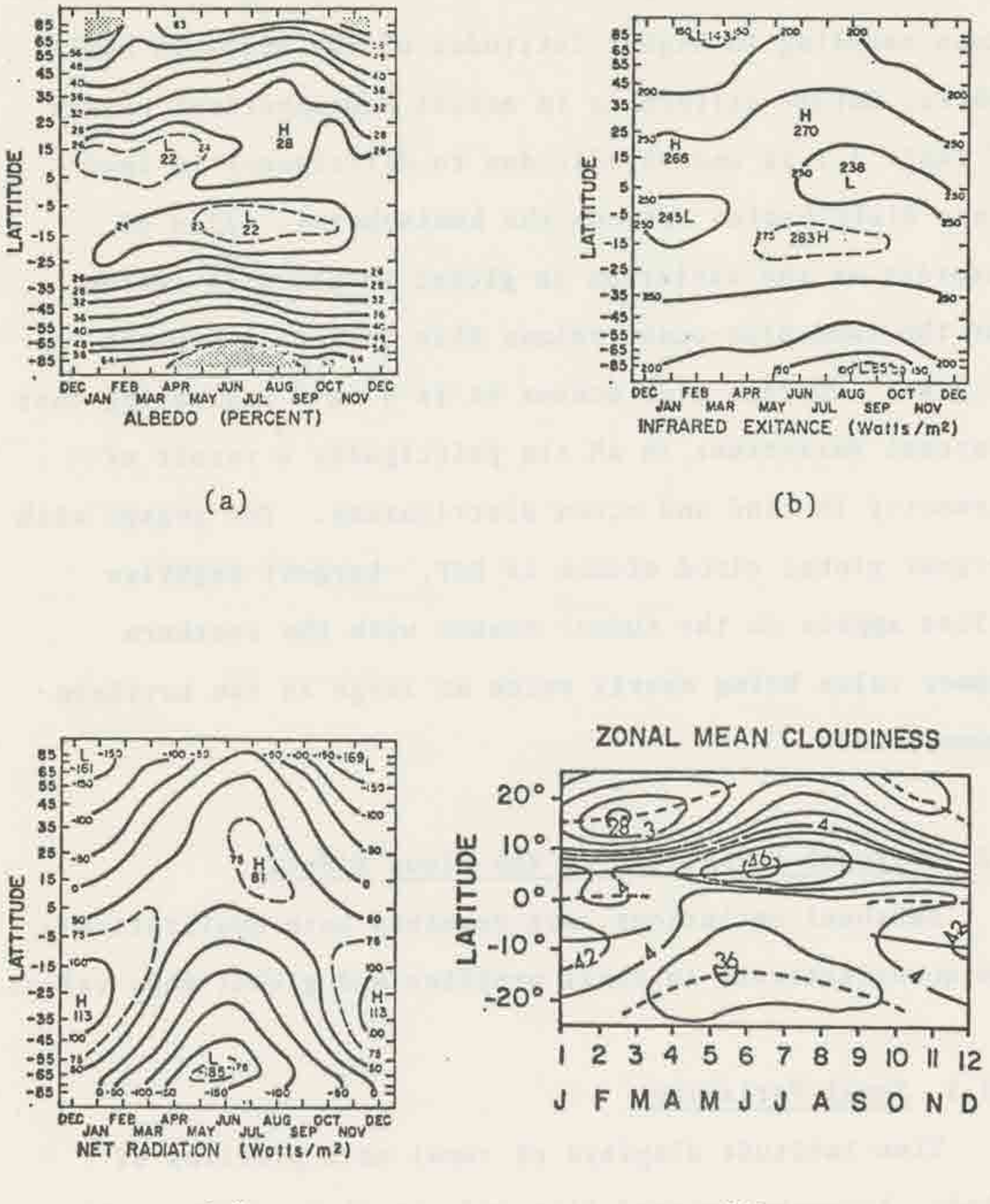

(a)

(b)

(c)

(d)

Figure 3.4.: Time-latitude analysis of zonal mean profiles from the 29 month set: (a) albedo, (b) long-wave flux, (c) net flux and (d) cloud amount.

display of tropical cloud amount from Murakami (1975). Large seasonal variations in albedo and longwave flux occur in the 30N-30S latitude zone. Of particular interest is the albedo increase in the Equator-to-20N zone from a low value of 24 percent in May to 28 percent in August, followed by an abrupt decrease in October to 25 percent (Figure 3.4a). Undoubtedly the variation is associated with the cloudiness change during the Southwest Asian Monsoon. The same seasonal variation appears in cloud amount. Similarly, south of the equator in the tropics, a variation of lesser magnitude and of opposite sign takes place.

In latitude zones both north and south of the tropics, large changes in albedo take place throughout the year. By August and September the extratropical zones of the Northern Hemisphere attain their minimum albedo. Undoubtedly, this is an effect of a minimum in ice-snow and cloud coverage associated with the northward retreat of the polar front and a decrease in cyclogensis. At 45N latitude the seasonal variation amounts to 17 percent while at 45S latitude the variation is but 7 percent.

It must be recalled that these profiles are greatly smoothed in the north-south direction because the individual measurements were resolved at a geocentric arc distance at the earth's surface as large as 7770 km for some satellites, while as small as 50 km for others (Ellis and Vonder Haar, 1976). Some of the smaller wiggles in the isolines are artifacts of the satellite sampling. The emitted longwave flux of Figure 3.4b shows seasonal variation but of opposite sign to the albedo at corresponding temporal and spatial positions.

Net flux time-latitude depiction, derived from the albedo, emitted longwave flux and solar insolation, does not show the tropical zone anomalies as previously discussed (Figure 3.4c). To a large extent, the albedo and longwave anomalies largely cancel each other in the net. The overwhelming seasonal varying pattern in the net follows closely the pattern of extraterrestrial solar flux as shown in Sellers (1965). Seasonal variations due to cloud effects in net radiation as observed in zonal mean profiles are apparently quite small compared to the effect of the north-south march of extraterrestrial solar flux with time.

3.3.2 Global Variations

The effect of clouds in the annual (intra-annual) variation of the global net radiation budget is assessed by two methods. The first is an indirect method which evaluates contributions to the annual variation from other than the cloud contribution. The residual variation not explained by the other than cloud contribution is taken to be the cloud contribution. The second method, a direct method, examines the annual variation of the globally integrated values from the four semi-monthly zonal profiles of cloud effects. Each of the methods are discussed in order, first the indirect and then the direct.

3.3.2.1 Indirect Analysis Method

The radiation budget components of incoming solar flux and outgoing reflected shortwave and longwave flux were globally integrated and composited into monthly mean values from the 29 month satellite data set compiled by Ellis and Vonder Haar (1976). A discussion of the integration method along with a monthly mean tabulated listing of the global incoming solar insolation, albedo, reflected shortwave flux, outgoing longwave flux and net flux are given in Appendix C.

Global values of the planetary net radiation flux, the composited mean values (N) and the individual monthly values, are plotted in Figure 3.5a. There is a considerable amount of month-to-month variability in both the composited mean curve and in the envelope of all values. Even though the uncertainty in the global values is as large as 10 wm^{-2} (Ellis and Vonder Haar, 1976), which is more than one half the amplitude of the annual variation, the fact that the shape of the envelope and the composite curve are so very similar gives credibility to the phase and amplitude of the annual variation. Another way of looking at the credibility of the annual variation is to observe that the variability of the individual monthly values about the composite curve does not exceed ± 12 wm^{-2} for any monthly period, while the variability of the individual monthly values about the annual mean value is greater than ± 25 wm^{-2}. The difference, 13 wm^{-2}, can be attributed to annual variation. The credibility of annual variation in global net radiation

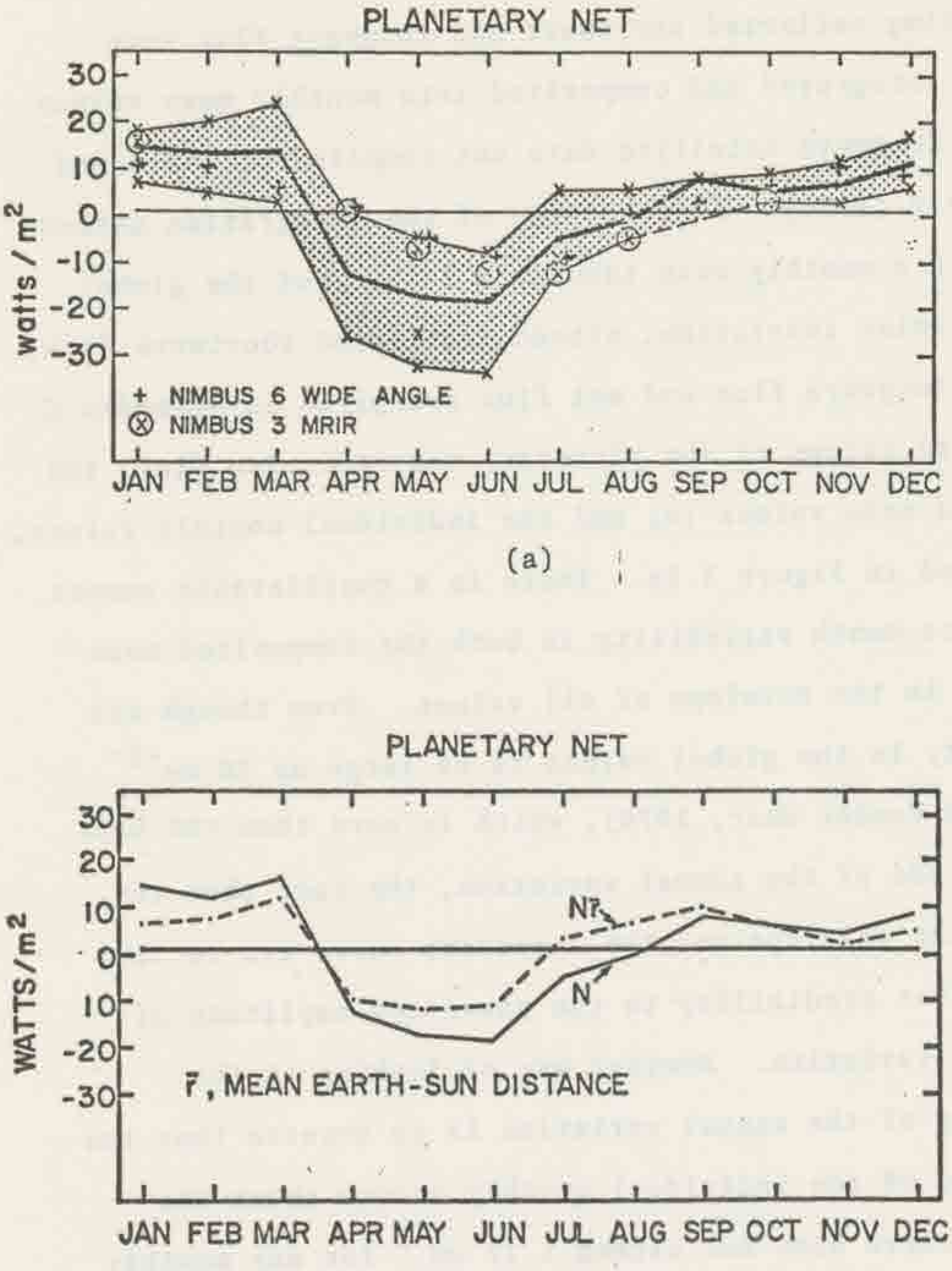

(a)

(b)

Figure 3.5.: Annual variation in global net flux.

is further validated by planetary heat budget studies. Annual variation in the rate of change in heat content (storage) of the planet Earth was shown by Ellis et al, (1978) to be of the same amplitude and phase as the seasonal variation in the planetary net radiation budget. The global heat storage had been computed from independant, in situ measurements of temperature.

That there should be an annual variation in the global planetary net radiation budget was discussed from a theoretical viewpoint by Simpson (1929) prior to the advent of artificial earth satellites for its measurement. Raschke (1973) concluded from the data of the medium resolution infrared radiometer (MRIR) onboard the Nimbus 3 satellite, that during the ten semi-monthly periods examined, there was appreciable annual variation. The Nimbus 3 values, which are included in the composite profile, are uniquely identified in Figure 3.5a. Also identified are preliminary values from the wide angle earth radiation budget sensor aboard the Nimbus 6 satellite (Smith et al, 1977). The Nimbus 6 data have not been included as part of the composite data set, since they are preliminary values. The agreement between the Nimbus 3 and Nimbus 6 value is suprisingly good.

Annual variation in the planetary radiation budget is hypothesized to receive principal contributions from the following:

1. Annual variation in the earth-sun distance.

2. A semi-annual cycle in the global albedo because of enhancement from the highly reflective polar regions near the time of solstice.
3. Annual variation in the global albedo because of the seasonal advance and retreat of sea ice and continental snow cover.
4. Annual variation in the longwave emission to space because of unequal temperature response between the land and water surfaces and the assymetrical distribution of these surfaces between the Northern and Southern Hemispheres.
5. Seasonal variation in the distribution and amount of global cloud cover.

The orbit of the planet Earth about the Sun is eccentric. The solar flux received by the planet as it moves in its orbit varies as a sine wave with a period of one year because of the eccentric orbit. The amptitude in annual variation of globally integrated solar flux received by the earth is approximately 11 wm^{-2} (assuming a solar constant equivalent to 1360 wm^{-2}). The annual cycle was removed from the incoming flux and the global net radiation was recomputed. These artificial global net radiation values are plotted as a composited mean curve, Nr, in Figure 3.5b. The difference between the N and Nr curves illustrates the contribution to the annual variation in net radiation flux from the annual variation in incoming solar flux. The contribution is slightly less than one half the amplitude of annual variation of the globel net flux. Therefore the annual variation in global net radiation is only partially explained by the contribution from solar flux.

The other two components of the global net radiation balance, the global albedo and global outgoing longwave flux, will be examined for annual variation. The global albedo composited mean profile and the envelope of individual monthly values are plotted by month in Figure 3.6a. There is but one value plotted for five of the monthly periods, because the albedo values from the ESSA 7 satellite data were excluded from this analysis (discussed in Appendix C). The global albedo values from the preliminary Nimbus 6 data set are plotted, but are not included in the composite curve. The Nimbus 6 albedo values are systematically larger than the composite curve, but generally show phase agreement with the composite. Largest discrepancies in month-to-month variation between the two curves appear in the months of March and November.

The contribution to the annual variation in the global albedo due to north-to-south differences in the earth-atmosphere planetary albedo can be assessed, ie. the snow and ice covered polar latitude zone in each hemisphere (60 to 90 degrees) has a larger zonal mean albedo than the tropical latitude zone (20N to 20S degrees latitude) (Vonder Haar, 1968; Vonder Haar and Soumi, 1971; Ellis and Vonder Haar, 1976).

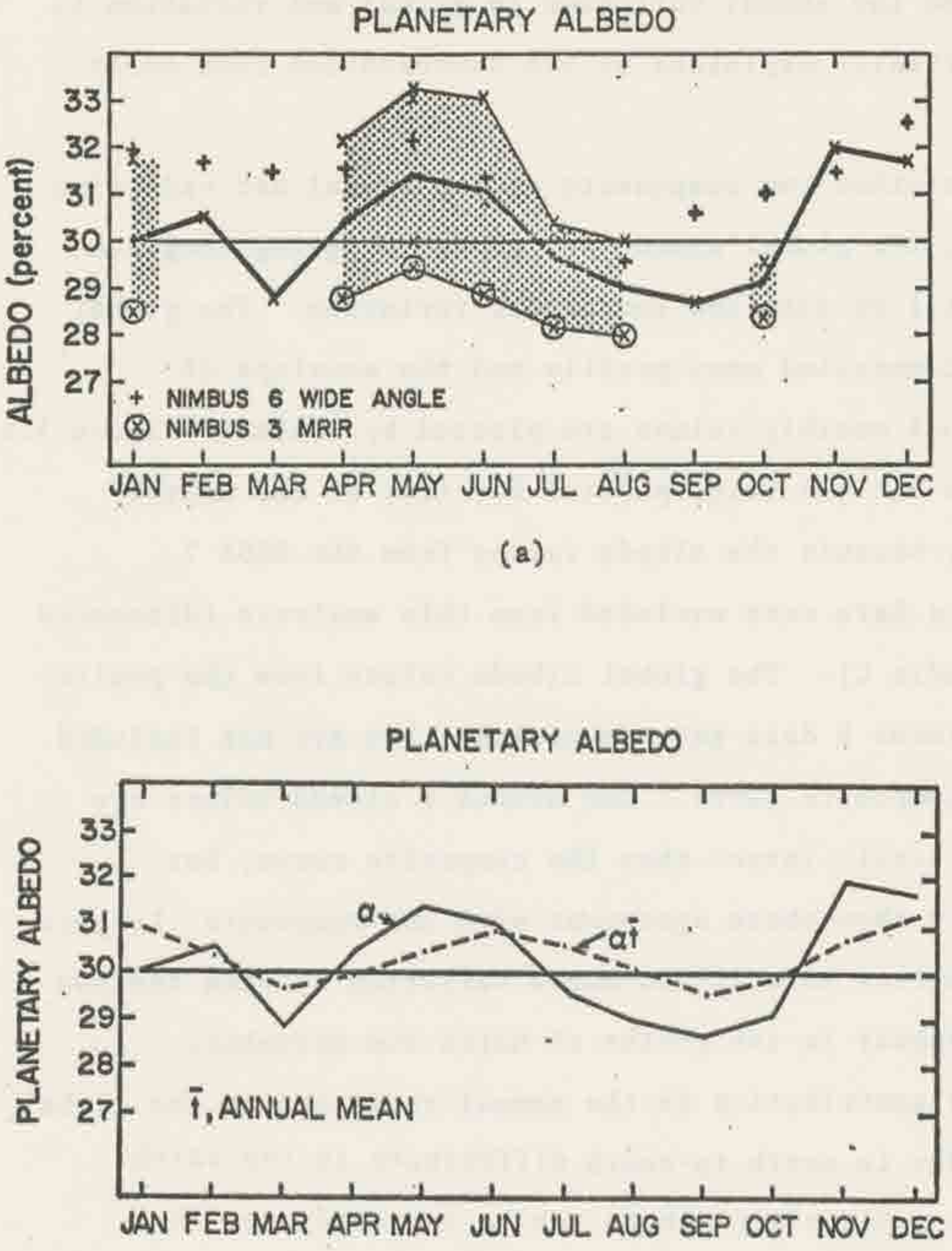

(a)

(b)

Figure 3.6.: Annual variation in global albedo.

The annual albedo in each latitude zone ($\alpha(\phi)$) can be computed with equation (3.4)

$$\alpha(\phi) = \frac{\int^{12\ \text{months}} \bar{\alpha}(\phi,t)s(\phi,t)dt}{s(\phi,t)dt} \tag{3.4}$$

where:

$\bar{\alpha}$ = the zonal mean planetary albedo

s = incoming solar flux

t = time in months

ϕ = latitude

The global albedo may now be computed for each month, assuming that the annual albedo in each latitude zone prevails for that month,

$$\alpha_{\bar{t}} = \frac{\int_{-\pi/2}^{\pi/2} \alpha(\phi)s(\phi,t)d(\sin\phi)}{s(\phi,t)d(\sin\phi)} \tag{3.5}$$

The $\alpha_{\bar{t}}$ values are plotted by month along with the actual composite global albedo values (α) in Figure 3.6b. The $\alpha_{\bar{t}}$ curve shows semi-annual periodicity with maxima at the summer and winter solstice and minima at the vernal and autumnal equinox. The largest maxima occurs at winter solstice. The difference between maximum and minimum values amount to 1.5 percentage values. The $\alpha\bar{t}$ annual variation contributes approximately 4 wm^{-2} to the annual variation in the absorbed shortwave flux.

The $\alpha_{\bar{t}}$ contribution to the variation in absorbed shortwave flux is negative near winter solstice. The earth is nearest to the sun several weeks later (perihelion) when the solar flux contribution is greatest. Six months later, when the earth is farthest from the sun, the $\alpha_{\bar{t}}$ contribution is again negative. Thus, the positive solar contribution to the absorbed shortwave flux (+8 wm^{-2}) is diminished by 2 wm^{-2} near winter solstice, while the negative solar contribution to absorbed shortwave flux (-8 wm^{-2}) is amplified by an additional 2 wm^{-2}.

The annual variation in $\alpha_{\bar{t}}$ accounts for one half the variation in α. The residual albedo variation, 1.5 percentage values (4 wm^{-2}), can be attributed to varying albedo within the latitude zones. Sampling bias, directional reflectance properties of an earth-atmosphere column, changes in cloud, snow, ice and vegetation cover contribute to the temporal albedo variation within latitude zones, and thus to the residual variation in global albedo. The cloud effect appears to be less than 4 wm^{-2} in the annual variation of the global shortwave component of net radiation provided that the other temporally varying contributors are not masking the cloud effect.

The global integrated emitted longwave flux composite curve (I) is plotted in Figure 3.7a. Also shown is the range of values within each month and the individual Nimbus 3 values. The Nimbus 3 values fall along a curve which can be fitted with an annual wave. Raschke (1973)

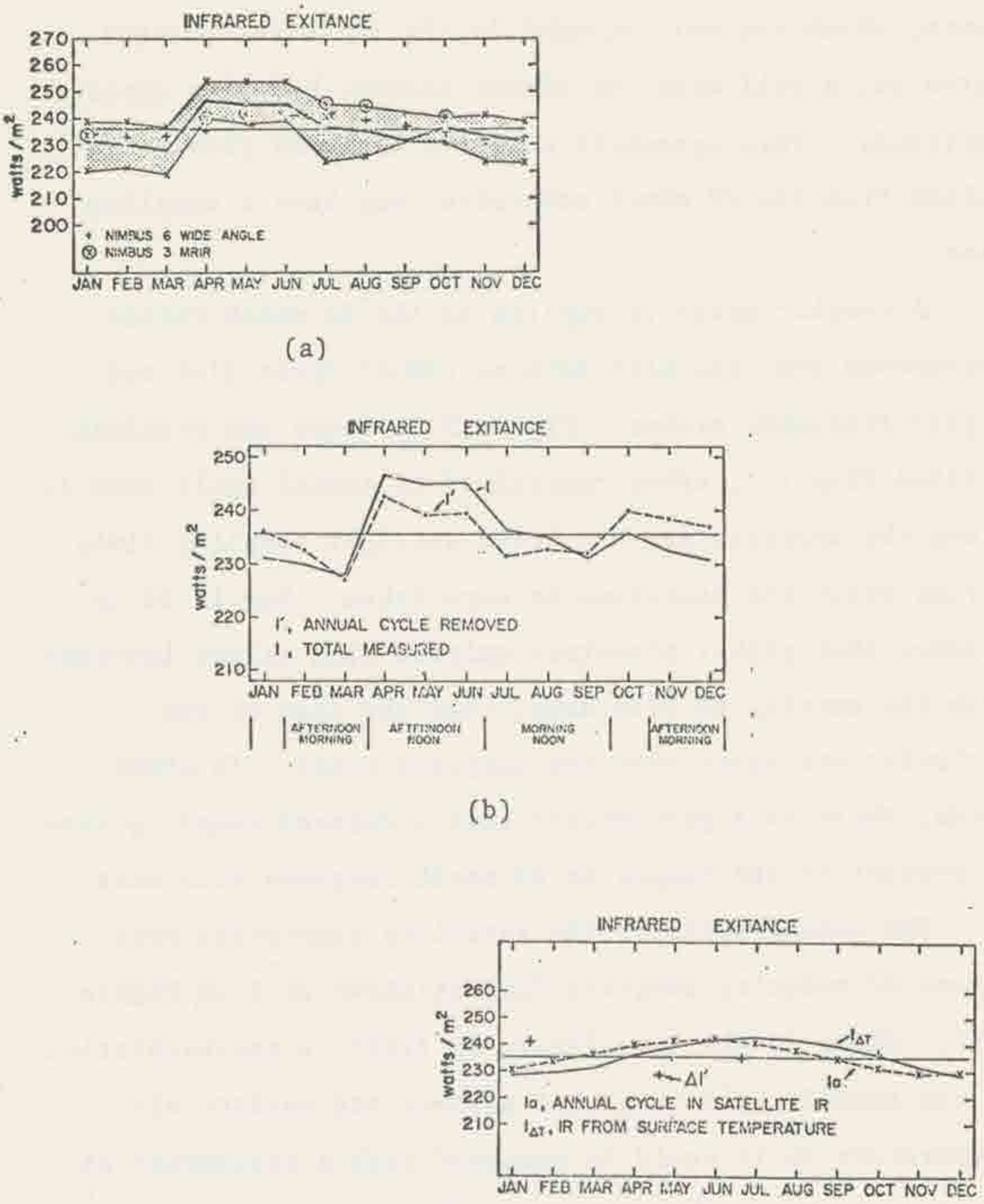

(a)

(b)

(c)

Figure 3.7.: Annual variation in global longwave flux.

has also shown the annual wave in Nimbus 3 measurements. Preliminary results from Nimbus 6 ERB wide angle measurements, which are not included in the 29 month averages, agree quite well with the Nimbus values, but with smaller amplitude. This agreement suggests that the global mean values from the 29 month composite may have a sampling bias.

A fourier analysis applied to the 29 month values decomposed the time plot into an annual cycle (Ia) and higher frequency cycles. Figure 3.7b shows the residual emitted flux (I') after removal of an annual cycle from I. Along the abscissa are bracketed daylight sampling times during which the measurements were taken. Now if it is assumed that global planetary emitted flux values increase from the morning to afternoon, then the sign of the I' perturbations agree with the sampling times. In other words, there is a possibility that a duirnal sampling bias is present in the composite 29 month longwave flux data.

The annual cycle in the satellite composited mean values of outgoing longwave flux is shown as I in Figure 3.7c. Shown in the same figure is $I(\Delta T)$, a representation of the annual cycle in global surface and surface air temperature as it would be measured with a radiometer at the top of the earths atmosphere in the absence of compensations by the earths atmosphere.

Global integration of the combined ocean surface temperature (Washington and Thiel, 1970) data and land surface air temperature data (Crutcher et al., 1970 and Taljaard et al., 1969) showed an annual cycle in the global surface temperature with amplitude of ±2°c. The effect of the annual cycle in global surface temperature on the outgoing longwave flux to space was assessed with the aid of the radiative transfer equation. The equation in a broadband flux form for an atmosphere in thermodynamic radiative equilibrium containing no scattering is,

$$F(Tr) = \varepsilon\sigma Ts^4\tau + \int_0^{z_t} \left[\alpha T(z)^4 \frac{\partial\tau(z)}{\partial z} dz\right] \qquad (3.6)$$

where ε, the surface emissivity will be assumed to be equal to unity, σ is the Stefan-Boltzmann contact, T is temperature, τ_s is the transmittance of the atmosphere to upwelling surface flux, z is height and z_t is the height of the top of the radiating atmosphere. Equation (3.6) may be represented by,

$$F(Tr) = F(Ts)\tau_s + F(Ta) \qquad (3.7)$$

where F is the upward directed longwave flux at the top of the atmosphere at the effective blackbody radiating temperature of the earth-atmosphere system (Tr), the surface temperature (Ts) and the atmospheric temperature (Ta). Divide equation (3.7) by F(Ts) to get,

$$\frac{F(Tr)}{F(Ts)} = \tau_S + \frac{F(Ta)}{F(Ts)} \qquad (3.8)$$

It will be assumed, as a first order approximation to the radiative processes, that τ_S and the ratio $\frac{F(Ta)}{F(Ts)}$ do not change with small changes in surface temperature. Call the right hand side of equation (3.8) K, and differentiate with respect to surface temperature,

$$\frac{dF(Tr)}{dTs} = K4\sigma Ts^3 \qquad (3.9)$$

where:

$$K = \frac{Im}{\sigma Ts^4} \qquad (3.10)$$

with Im defined as F (Tr). Combine equations (3.9) and (3.10) so that,

$$\frac{dIm}{dTs} = \frac{4Im}{Ts} \qquad (3.11)$$

The annual global longwave flux to space, Im, from the 29 month satellite data set is 235.7 wm^{-2}, while the annual global surface temperature is 288^{o}K. Thus,

$$\frac{dIm}{dTs} = 3.3 \text{ wm}^{-2} \qquad (3.12)$$

and K is equal to 0.60.

It is known that T^4 is approximately linear in T for the normal range of atmospheric and surface temperatures, so that no serious error is introduced by applying equation (3.12) over the 4°K range of global surface temperatures. If ε in equation (3.6) were taken to be 0.9 rather than 1.0, then $\frac{dI}{dTs}$ would be 3.7 wm^{-2} rather than 3.3 wm^{-2}. Either value is sufficient for the purpose of this discussion.

The effect of the annual wave in global surface and surface air temperature was inserted into the annual global longwave flux at monthly time intervals (t) by,

$$I(t) = Im + \frac{dIm}{dTs} \Delta Ts(t) \qquad (3.13)$$

where ΔTs is the algebraic difference between monthly mean Ts and the annual mean Ts. I(t) is plotted as $I(\Delta T)$ in Figure 3.7c. Both $I(\Delta T)$ and Ia are of the same amplitude but differ in phase by one month. It should be noted that $I(\Delta T)$ has the same phase as the annual profiles of I for the Nimbus 3 and 6 satellites (Figure 3.7a). The equivalence in phase between the $I(\Delta T)$ and the Nimbus satellite profiles and the phase difference between $I(\Delta T)$ and Ia further supports the argument that the composited mean profile in Figure 3.7a may contain temporal sampling bias. If one concludes that all of the I'(Figure 3.7b) and the phase shift in wave number one of I are due to sampling bias, then one must also conclude that there is no apparent effect on the annual variation of I which is due to an annual variation in cloudiness, ie. month-to-month variations in cloud amount, and/or effective radiating temperatures. However, cloudiness modulates the amplitude of I even though cloudiness may not show a month-to-month effect on I. It is evident from equation (3.6) that τ_s, the tramissivity of the atmosphere to the net upward longwave flux from the earth's surface, varies directly with large changes in cloud amount and changes in the transparency of the clouds to the upwelling flux. If the effect of cloudiness on Ts and on the second term of equation (3.6) is neglected, then the elimination of all cloudiness will increase τ_s and thus increase the magnitude of response in F(Tr), or I, to an annual wave in global surface temperature. The converse argument with an increase in cloud amount (all other cloud properties held constant) shows that the annual amplitude in I will be less. The magnitude of the cloud effect on the amplitude of the annual wave quantitatively will be shown as part of the discussion on the direct method for resolving the effects of clouds on the global planetary radiation balance (Section 3.3.2.2).

The planetary net radiation curve has been reconstructed in Figure 3.8 using just the annual cycle of the longwave flux (Ia) from Figure 3.7c as the longwave contribution to the net radiation flux. (Note: the phase of the net radiation curve in Figure 3.8 would be shifted one half month later into the year if the I (ΔT) curve were used rather than

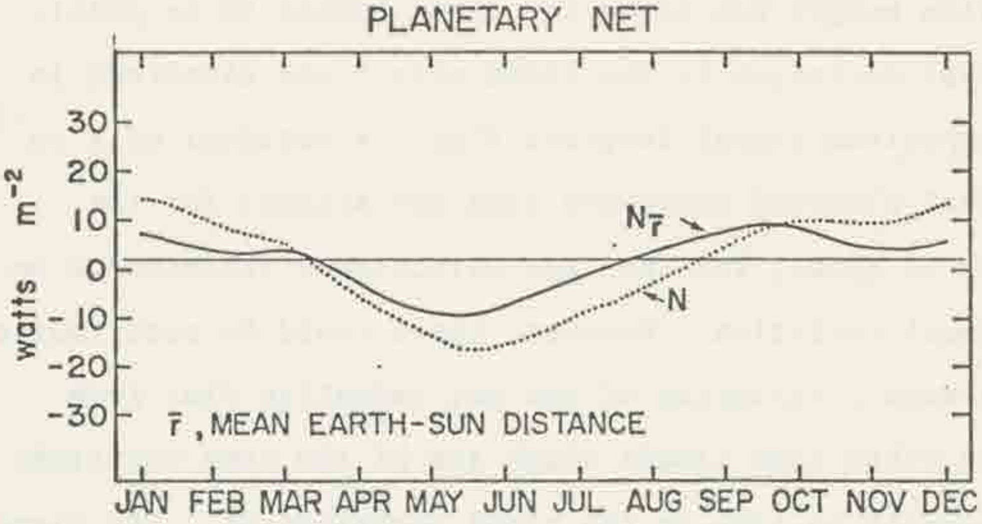

Figure 3.8.: Annual variation in global net flux with just an annual wave in longwave flux.

the Ia curve). A comparison of the curves of Figure 3.5b and 3.8 reveals that the principal differences occur in the months of March and April. Both curves have the same general shape over the other monthly periods.

The indirect method of examining the month-to-month variations in the cloud effect on the global planetary radiation budget has shown the cloud effect to be small. No annual variation in the cloud effect was discerned in the composited global longwave flux. A residual of 4 wm^{-2} in global absorbed shortwave flux may account for the effects of cloud, ice-snow and directional reflectance on the annual variation. However, there could be contributions to the annual variation of the net radiation flux from sources other than clouds which are of the same magnitude but opposite in sign to the cloud contribution. The cloud effect would be masked in such cases.

3.3.2.2 Direct Analysis Method

A second method, a direct analysis of the globally and hemispherically integrated cloud effects, will be used to assess the cloud effect on the annual variation of the net radiation budget. Global and hemispherical values of the cloud effect on the albedo ($\Delta\alpha$) longwave flux (ΔI) and net radiation flux (ΔN) were derived by integrating the zonal profiles of the cloud effects from Figures 2.1, 2.5 and 2.8, respectively. The integrated values are shown in Tables 3.3, 3.4 and 3.5. The cloud effect on the net

Table 3.3 - Cloud effect in net flux (ΔN) semi-monthly periods for land-plus-ocean (wm^{-2})

	MAY	JULY	OCT.	JAN-FEB
65N-65S	-12.0	-15.8	-23.1	-26.7
65N-0	-18.6	-23.8	-13.1	-11.7
65S-0	- 5.3	- 7.8	-33.2	-41.6

Table 3.4 - Cloud effect in albedo (ΔN) for land-plus-ocean

	MAY	JULY	OCT.	JAN.-FEB.	ANNUAL
65N-65S	+0.112	+0.105	+0.118	+0.112	+0.112
65N-0	+0.108	+0.105	+0.093	+0.084	+0.100
65S-0	+0.119	+0.105	+0.137	+0.127	+0.125

Table 3.5 - Cloud effect in emitted flux (ΔI) for land-plus-ocean (wm^{-2})

	MAY	JULY	OCT.	JAN.-FEB.	ANNUAL
65N-65S	-27.1	-19.9	-19.5	-14.1	-20.1
65N-0	-28.5	-22.6	-17.5	-10.6	-19.8
65S-0	-25.7	-17.3	-21.5	-17.6	-20.5

radiation is related to the cloud effect on the radiation budget components (the albedo and longwave flux) by equation (3.3).

The cloud effect on the albedo increases in both hemispheres going from the winter season to the spring season (Table 3.4). This increase is probably related to the increase in illumination of the clouds and the ice-snow areas of the higher latitudes. A decrease, similar in magnitude to the increase, occurs in both hemispheres going from the summer season to the fall season. The decline in the cloud effect on the albedo continues into the winter season of each hemisphere. The sign of the change in the cloud effect on the albedo is the same for the globe and the Southern Hemisphere. Thus, the cloud effect on the albedo of the Southern Hemisphere is predominant in the global integral over the same effect of the Northern Hemisphere. The predominance of the Southern Hemisphere cloud effect is most apparent in the annual mean values.

The annual variation in $\Delta\alpha$ may be expressed as a departure from the annual mean ($\overline{\Delta\alpha}$),

$$\Delta\alpha' = \Delta\alpha - \overline{\Delta\alpha} \tag{3.14}$$

so that $\Delta\alpha'$ varies as ±0.007, or ±2.4 wm^{-2} in reflected flux. This variation is small, and does not significantly differ from the residual value of ±4 wm^{-2} derived by the indirect method. Thus the annual variation in the global albedo due to cloud effects appears to contribute less than ±3 wm^{-2} to the annual variation in the net radiation flux.

The annual variation in emitted longwave flux due to clouds can be expressed in the same fashion as,

$$\Delta I' = \Delta I - \overline{\Delta I} \qquad (3.15)$$

where $\overline{\Delta I}$ is the annual mean cloud effect in the longwave flux. The $\Delta I'$ variation is slightly less than ±7 wm^{-2}. The $\Delta I'$ values have been added to the Ia value and are plotted on Figure 3.7c as plus signs for a comparison with the annual variation of the longwave flux. Notice that the $\Delta I'$ values are of the same magnitude as the annual variation (Ia) but are generally of opposite sign. Of course, the four points along the curve are hardly sufficient to evaluate the annual variation in $\Delta I'$. Since $\Delta I'$ is of opposite sign to Ia, the cloud effects act to reduce the amplitude of Ia.

Table 3.6 shows ΔI values for a globe hypothetically covered entirely by ocean. The table values were generated by globally integrating the zonal ΔI ocean profiles of Figure 2.6. Note that a global average $\Delta I'$ from Table 3.6 has an annual amplitude of less than ±2.5 wm^{-2} and is not in phase with the $\Delta I'$ of ±7 wm^{-2} derived from Table 3.5. The larger $\Delta I'$ of Table 3.5 is largely a result of the asymmetry of the land-ocean distribution between the Northern and Southern Hemispheres. Indeed, it is reasonable

Table 3.6 - Cloud effect in emitted flux (ΔI) for oceans (wm^{-2})

	MAY	JULY	OCT.	JAN-FEB
65N-65S	-20.9	-21.7	-23.1	-18.8
65N-0	-15.6	-23.6	-22.4	-14.2
65S-0	-26.2	-19.8	-23.9	-23.5

to conclude that the removal of clouds over the continental regions would increase the amplitude of Ia due to an increase in the atmospheric transmittance (τ_s in equation 3.6) to thermal radiation upwelling from the earth's surface, ie. an increase in K of equation (3.9). It is not suprising that clouds act to dampen the annual variation in emitted longwave flux. The ΔI' variation derived from Table 3.5, may be actually less than 7 wm^{-2} because of a data sampling deficiency in the January-February data. Elimination of that semi-monthly period from the study will reduce the variability of ΔI' to less than ±4 wm^{-2}. This 4 wm^{-2} added to the 6 wm^{-2} amplitude of Ia is equivalent to 10 wm^{-2} amplitude. This is the total annual variation which would be obtained apparently with an instantaneous removal of all clouds. This is the same annual variation which would be computed by equation (3.9) with K equal to 1.0. Thus, the annual variation of the longwave flux (in the absence of all clouds) is nearly equivalent to the upwelling longwave flux at the earth's surface. The results of this direct analysis indicate that as much as ±4 wm^{-2} of the I' annual variation shown in Figure 3.7b can be accounted for by annual variations in cloud effect on Ia.

Annual variations in the planetary net flux due to annual variations in cloudiness can be elucidated by plotting N', the departure of semi-monthly values from the annual mean net flux ($\bar{N}$) with ΔN' for the four semi-monthly periods.

The symbols are defined as:

$$\Delta N' = \Delta N - \overline{\Delta N} \tag{3.16}$$

and

$$N' = N - \overline{N} \tag{3.17}$$

Figure 3.9 shows that the two plots are nearly 180 degrees out of phase. The difference between N' and ΔN' in the January-February period is 18.3 wm^{-2}, while it is -18.1 wm^{-2} in the July period. The near equivalency in absolute magnitude illustrates an element of symmetry during the year. It also illustrates that the amplitude in N', ±13 wm^{-2}, could be increased to ±18 wm^{-2} with an instantaneous removal of all clouds (without a simultaneous adjustment to a condition of radiative equilibrium).

In summary (for the 29 month period studied) the annual variation in the global planetary net radiation budget due to the effect of clouds is small. The cloud effect on the annual variation of shortwave absorbed flux is less than ±3 wm^{-2}, on the emitted longwave flux it is less than ±6 wm^{-2} (and most probably less than ±4 wm^{-2} in the longwave component). Clouds generally act to reduce the amplitude of the annual variation in the net radiation budget.

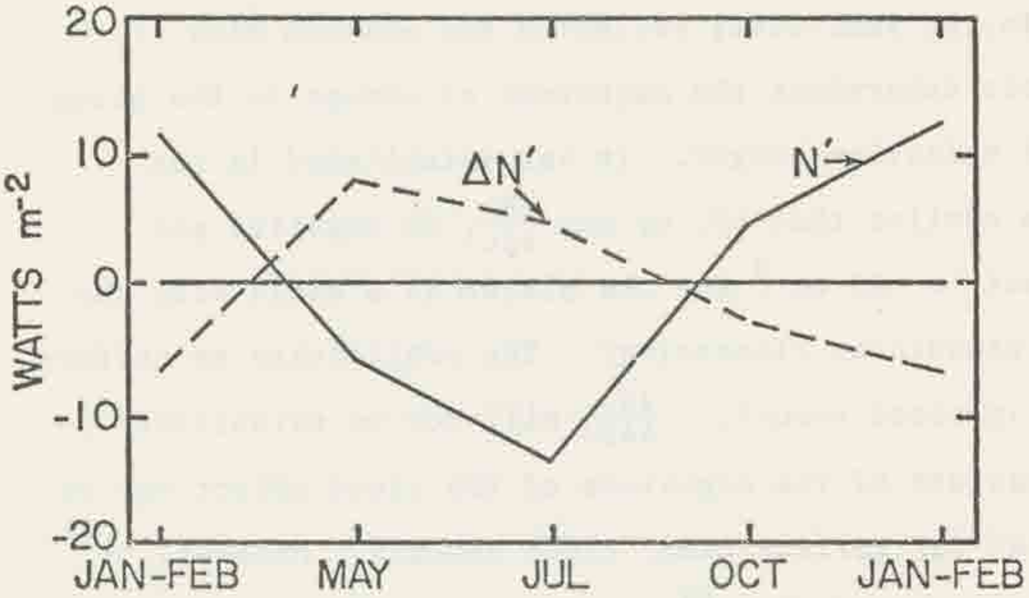

Figure 3.9.: Annual variation in net flux (N') and in the cloud effect in net flux (ΔN') for four semi-monthly periods.

4. SENSITIVITY TO A UNIFORM CHANGE IN CLOUD AMOUNT

A local uniform increase in cloud amount at all altitudes without a change in other cloud characteristics, including cloud top height, will give rise to an increase in the shortwave flux reflected to space and a decrease in the longwave flux emitted to space. The magnitude of change in the individual reflected and emitted flux components determines the magnitude of change in the planetary net radiation budget. It was established in the previous section that ΔN, or $\Delta Ac \frac{\Delta N}{\Delta Ac}$, is negative and equivalent to -33 wm^{-2} for the planet as a whole with the present cloudiness climatology. The sensitivity to uniform changes in cloud amount, $\frac{\partial N}{\partial Ac}$, will now be established so that a measure of the magnitude of the cloud effect may be determined for various other cloud amounts. However, it must be remembered that $\frac{\partial N}{\partial Ac}$ may not be valid for other climate states which have a mix of clouds with radiative characteristics different than "today's". These characteristics include: height, the vertical and horizontal distribution of finite clouds, the land-ocean spatial distribution, the cloud reflectance, transmittance and emittance. Given the same radiative characteristics as "today's" clouds, then $\frac{\partial N}{\partial Ac}$ is a constant over the full range of Ac values. The $\frac{\partial N}{\partial Ac}$ will be examined at both zonal and global mean scales.

4.1 Zonal Sensitivity

The net flux sensitivity to cloud amount, $\frac{\partial N}{\partial Ac}$, has been written as δ by both Schneider (1972) and Cess (1976) so that equation (3.1) is simply,

$$\delta = \frac{\partial Ab}{\partial Ac} - \frac{\partial I}{\partial Ac} \tag{4.1}$$

The denominator in equation (4.1) is equivalent to Ac, if the derivatives are taken as the difference between "today's" cloud amount and cloud-free conditions. Since ΔN of equation (3.3) was derived as the difference between the cloud-free and "today's" cloudy net radiation budget, equation (4.1) is equivalent to equation (4.2) for uniform changes in cloud amount,

$$\delta = \frac{\Delta N}{Ac} \tag{4.2}$$

4.1.1 Cloud Amount

Zonal mean profiles of Ac are available from a number of studies; profiles have been deduced from satellite measurements and ground based observations. In keeping with a study based on satellite measurements, Ac is taken from the former source. The global coverage of satellites permit measurements in remote regions, where surface observations are not routinely available. Values of Ac determined satellite data, may not be accurate in an absolute sense, however, they are potentially more accurate in a relative sense (such as a north-south zonal mean profile).

Values of Ac have been taken from studies of Sadler (1969) and Clapp (1964). Both authors collected their statistics from TIROS satellite nephanalyses. Clapp's statistics are drawn from just one year of data (March 1962 through February 1963) while Sadler's are from two years of data (February 1965 through January 1967). Sadler's values are restricted to the 30N-to-30S latitude zone at a 2.5 degree latitude-longitude gridding. Clapp's values are in the 60N-to-60S latitude zone (except for the winter hemisphere in which the poleward limit is 55 degrees latitude) and are at 5 degrees latitude-longitude gridding. Values of Ac were selected from Sadler in the 30N-to-30S zone, from Clapp poleward of the tropical zone and from the ground based observations of Landsberg (as shown by Clapp) in the 65-to-60 latitude zone (65-to-55 latitude zone in the winter hemisphere). Clapp (1964) suggested that the cloudiness derived from the TIROS nephanalyses "tends" to underestimate the amount of scattered cloudiness but to overestimate cloud amount in the broken to overcast range of cloud cover. His values are seasonal averages while values taken from Sadler are averages for the February, May, July and October months. The blended profiles are shown for the four periods and for the annual mean in Figure 4.1. Note that the cloudiness associated with the ITCZ is distinctly shown as a spike in all periods. This spike can be identified with the spike in the total albedo of Figures 2.1 and 2.2. Plotted along with the annual

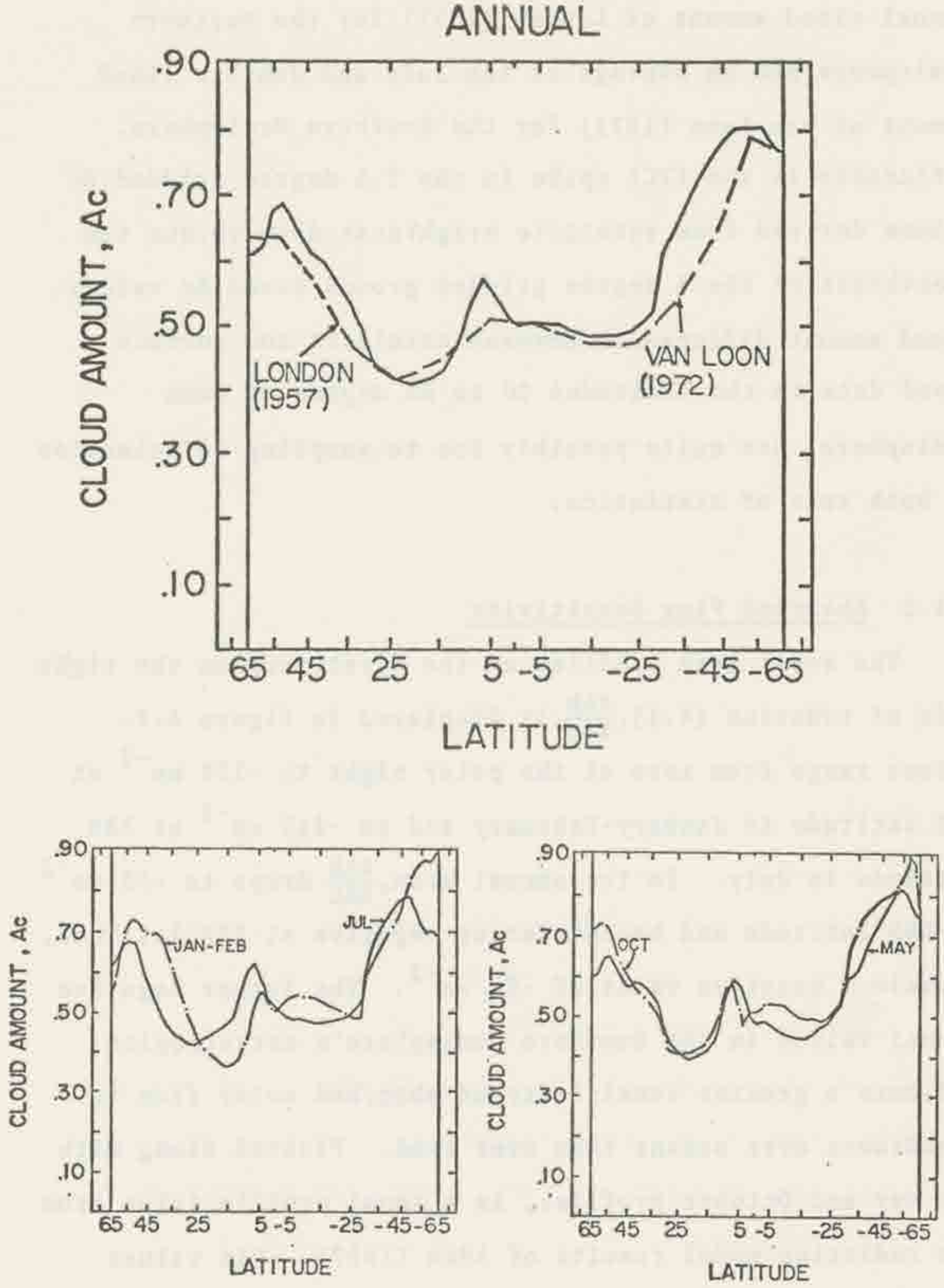

Figure 4.1.: Cloud amount from TIROS nephanalyses.

mean Ac curve derived from the satellite data, is the annual cloud amount of London (1957) for the Northern Hemisphere and an average of the July and January cloud amount of van Loon (1972) for the Southern Hemisphere. Noticeable is the ITCZ spike in the 2.5 degree gridded Ac values derived from satellite brightness data versus the smoothness of the 5 degree gridded ground based Ac values. Cloud amount differences between satellite and surface based data in the latitudes 30 to 65 degree of each hemisphere, are quite possibly due to sampling deficiencies in both sets of statistics.

4.1.2 Absorbed Flux Sensitivity

The zonal mean profiles of the first term on the right side of equation (4.1), $\frac{\partial Ab}{\partial Ac}$, is displayed in Figure 4.2. Values range from zero at the polar night to -128 wm^{-2} at 58S latitude in January-February and to -110 wm^{-2} at 58N latitude in July. In the annual mean, $\frac{\partial Ab}{\partial Ac}$ drops to -65 wm^{-2} at 50N latitude and becomes larger negative at 58S latitude, a maximum negative value of -86 wm^{-2}. The larger negative annual values in the Southern Hemisphere's extratropics indicate a greater sensitivity of absorbed solar flux to cloudiness over oceans than over land. Plotted along with the May and October profiles, is a zonal profile taken from the radiation model results of Adem (1967). His values are more than twice the satellite results in the tropical zones.

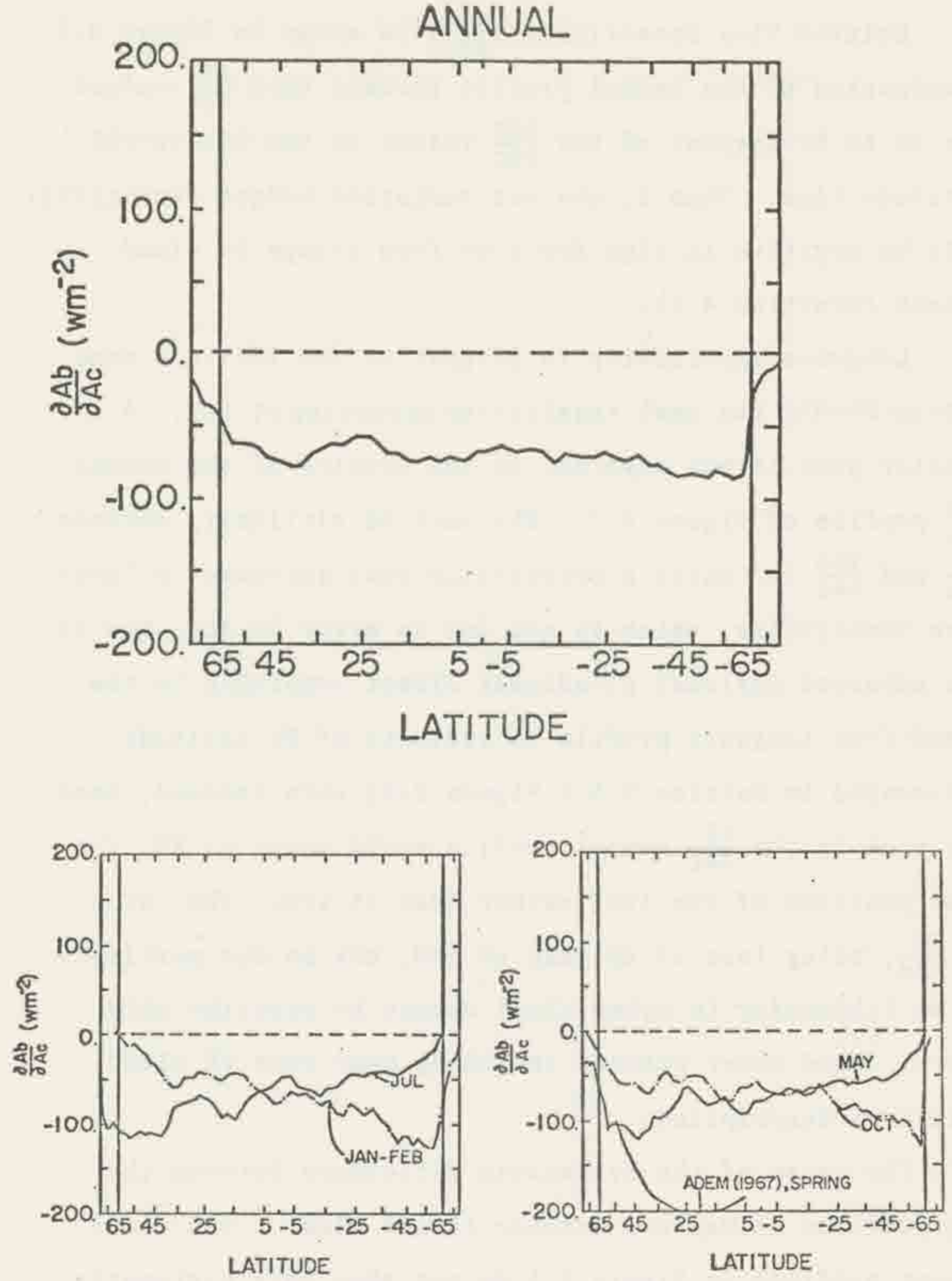

Figure 4.2.: Absorbed flux sensitivity to changes in cloud amount.

4.1.3 Emitted Flux Sensitivity

Emitted Flux Sensitivity ($\frac{\partial I}{\partial Ac}$) is shown in Figure 4.3. Examination of the annual profile reveals that $\frac{\partial I}{\partial Ac}$ values are 30 to 60 percent of the $\frac{\partial Ab}{\partial Ac}$ values in the 65N-to-65S latitude zone. Thus δ, the net radiation budget sensitivity, will be negative in sign for a uniform change in cloud amount (Equation 4.1).

Longwave sensitivity is largest in the latitude zone 17N-to-5N with the peak sensitivity occurring at 14N. A similar peak is not apparent in the tropics of the annual $\frac{\partial Ab}{\partial Ac}$ profile of Figure 4.2. The lack of similarity between $\frac{\partial I}{\partial Ac}$ and $\frac{\partial Ab}{\partial Ac}$ indicates a potentially real increase in longwave sensitivity, which is not due to error in Ac. Now if the apparent residual cloudiness effect remaining in the cloud-free longwave profile in vicinity of 8N latitude (discussed in Section 2.3.2 Figure 2.6) were removed, then the peak in the $\frac{\partial I}{\partial Ac}$ annual profile would occur at 8N, the mean position of the ITCZ rather than at 14N. The value of $\frac{\partial I}{\partial Ac}$, being less at 8N than at 14N, may be due partially to an inadequacy in using cloud amount to describe thin cirrus cloud cover without including some type of cloud emittance description.

The cause of the systematic difference between the $\frac{\partial I}{\partial Ac}$ profiles in May and October is not clear. The cloud amount profiles in Figure 4.1 do not show this systematic difference. One may conclude:

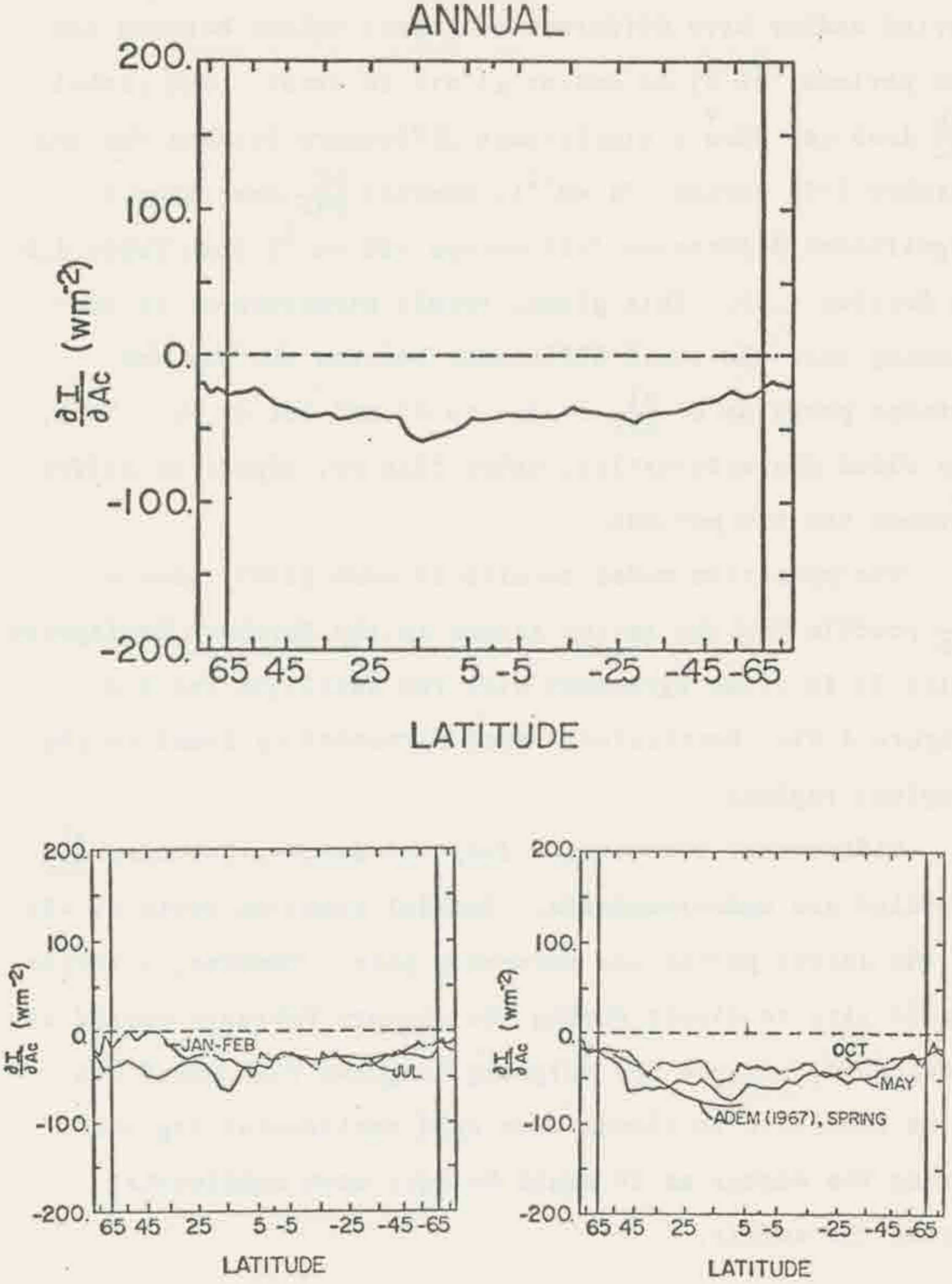

Figure 4.3.: Longwave flux sensitivity to changes in cloud amount.

1) Clouds, in general, are higher during the October period and/or have different emittance values between the two periods, or 2) Ac and/or ΔI are in error. The global $\frac{\partial Ab}{\partial Ac}$ does not show a significant difference between May and October (-72 versus -71 wm^{-2}), whereas $\frac{\partial I}{\partial Ac}$ does show a significant difference (-51 versus -35 wm^{-2}) (See Table 4.5 in Section 4.2). This global result gives support to confirming that the zonal difference between the May and October profiles of $\frac{\partial I}{\partial Ac}$ is due to ΔI and not to Ac. Thus, the cloud characteristics, other than Ac, appear to differ between the two periods.

The radiation model results of Adem (1967) gave a $\frac{\partial I}{\partial Ac}$ profile for the spring season in the Northern Hemisphere which is in close agreement with the satellite results (Figure 4.3). Particularly good agreement is found in the tropical regions.

Differences between the July and January-February $\frac{\partial I}{\partial Ac}$ profiles are understandable. Spatial sampling north of 45N in the latter period was extremely poor. However, a lesser sensitivity to clouds during the January-February period is acceptable, because the outgoing longwave flux would not be as sensitive to clouds over cold continental regions during the winter as it would be over warm continents during the summer.

4.1.4 Net Flux Sensitivity

The annual mean $\frac{\partial Ab}{\partial Ac}$ values were larger negative than the $\frac{\partial I}{\partial Ac}$ values between 65N and 65S latitude, so that application of equation 4.1, yields negative values for δ over the same latitude zones (Figure 4.4). The magnitude of the annual δ values decrease from a maximum in the Northern Hemisphere of -42 wm^{-2} at 55N to a minimum of -16 wm^{-2} at 11N. From 11N δ again increases to a maximum value in the Southern Hemisphere of -60 wm^{-2} at 55S. The minimum value appearing at 11N would appear at 8N (the mean ITCZ position in the Nimbus 3 data) if $\frac{\partial I}{\partial Ac}$ were to be adjusted for apparent residual cloud effects as previously discussed. The δ profile does not show perfect symmetry between hemispheres. A comparison of corresponding latitude zones between hemispheres show greater cloud sensitivity in all zones of the Southern Hemisphere.

An examination of the semi-monthly profiles reveals a negative δ at all latitudes, except at latitudes in and near the polar night. The region of the polar night comprises less than 10 percent of the global area, so that small positive values of δ have little effect on the globally integrated δ value.

Plotted along with the July and January-February profiles are Northern Hemisphere values which were computed by Schneider (1972). As he stated, his values ... are not intended to be taken as quantitatively realistic ... However, they are qualitatively realistic as for the sign

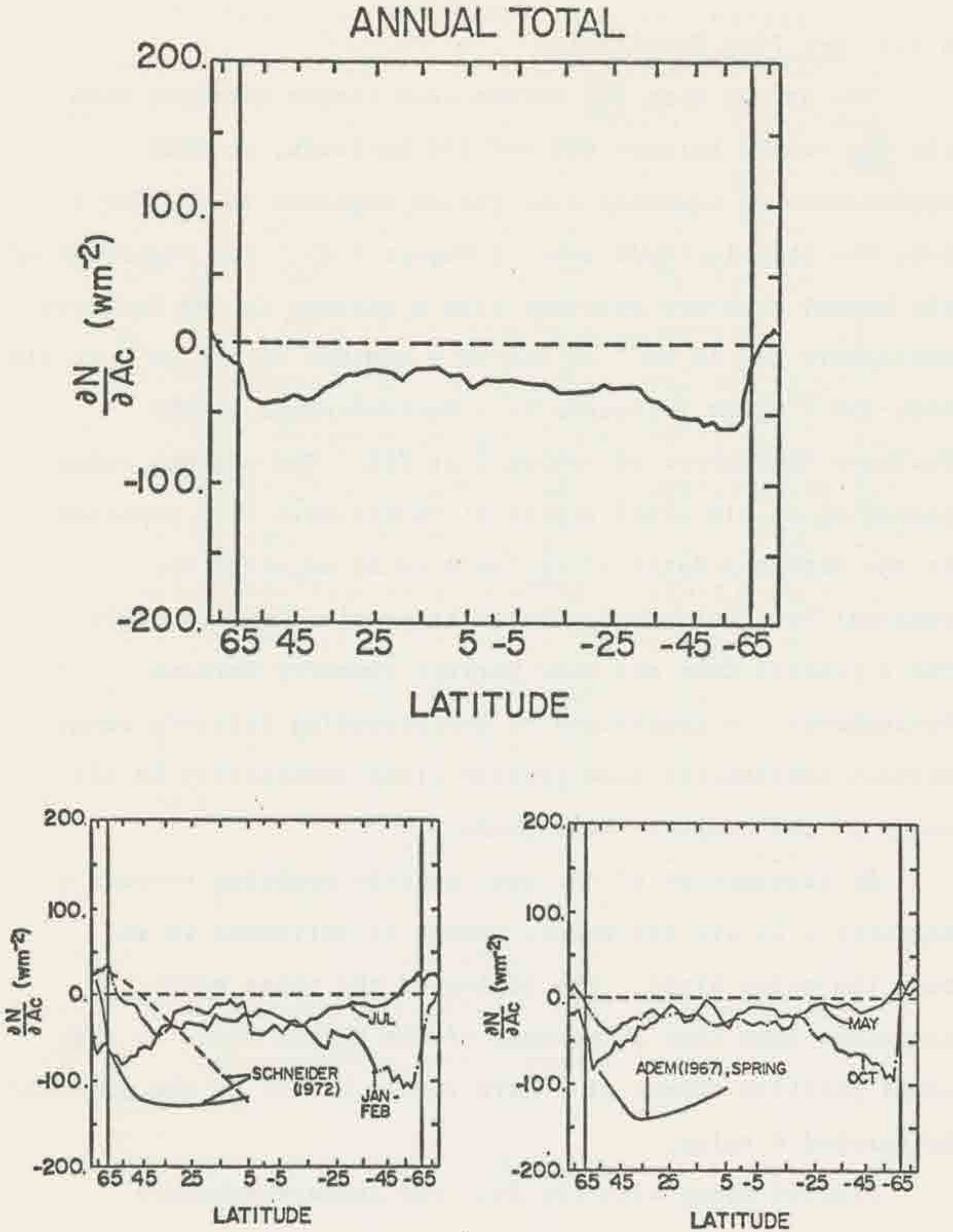

Figure 4.4.: Net flux sensitivity to changes in cloud amount.

on δ. The difference at 5N between Schneider's value and the "quantitatively realistic" value of this study is approximately 100 wm^{-2}. The difference is large because of the near cancellation between the satellite absorbed and longwave flux sensitivities in the tropical latitude zones.

Plotted on the May and October profiles are the results from Adem's (1967) radiation model calculations for the spring season. His values derived from a quantitative parameterized radiation model, compare no better with the results of the present study than did Schneider's qualitative results.

4.1.5 Atmospheric Transport Sensitivity

The sensitivity of the horizontal flux divergence in various latitude zones to changes in cloud amount may be investigated. The energy balance equation integrated throughout the vertical extent of the earth-atmosphere system is written for each latitude zone as:

$$N = \frac{\partial E}{\partial t} + \mathrm{divFa} + \mathrm{divFo} \qquad (4.3)$$

where: N = the net radiation flux at the top of the atmosphere.

$\frac{\partial E}{\partial t}$ = the time rate of change of energy content within the zone, or rate of heat storage by atmosphere, land, ocean and cryosphere.

divFa = meridional atmospheric energy flux transported out of the zone, or flux divergence.

divFo = meridional oceanic energy flux transported out of the zone, or flux divergence

Now just the atmospheric flux divergence term, divFa, will be permitted to respond to changes in cloud amount. All rate of heat storage terms, $\frac{\partial E}{\partial t}$ and the oceanic flux divergence, divFo, are assumed not to vary with cloud amount changes. This assumption has some validity only if the immediate or near simultaneous response of the system to a change in cloud amount is considered. Thus, the ocean transport and heat storage terms are permitted to respond only at some later time. This type of analysis permits one to observe the atmosphere response as an upper limit type of response.

Under the assumed conditions, the sensitivity to a cloud amount change, ΔAc, may be expressed as:

$$\frac{\partial N}{\partial Ac} \Delta Ac = \frac{\partial \, divFa}{\partial Ac} \Delta Ac \qquad (4.4)$$

or in simpler notation as:

$$\Delta N = \Delta divFa \qquad (4.5)$$

Figures 4.5, 4.6 and 4.7 show the response in $\Delta divFa$ for three different latitude zones with a $\Delta Ac = \pm .1$. The mean curves for divFa are taken from Oort and Vonder Haar (1976). The vertical bars represent a $\pm \Delta divFa$ response to a $\pm \Delta Ac$. They were computed from the tabulated $\frac{\partial N}{\partial Ac}$ in Table 4.1. They show that a change in cloud amount,

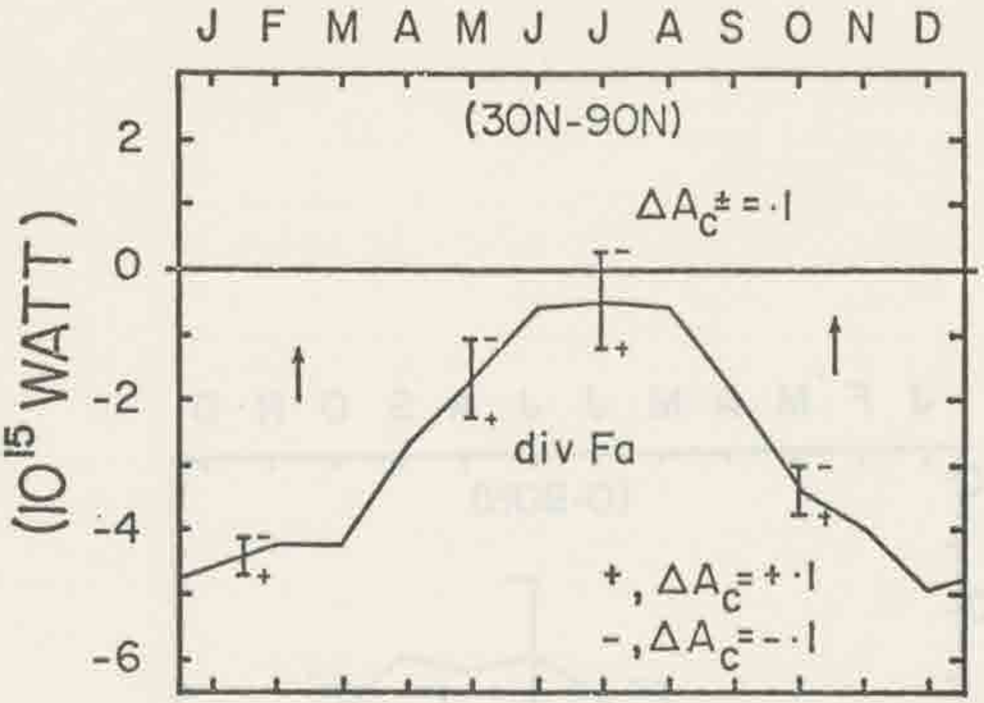

Figure 4.5. Atmospheric mean meridional energy flux divergence for the 30N-to-90N polar cap.

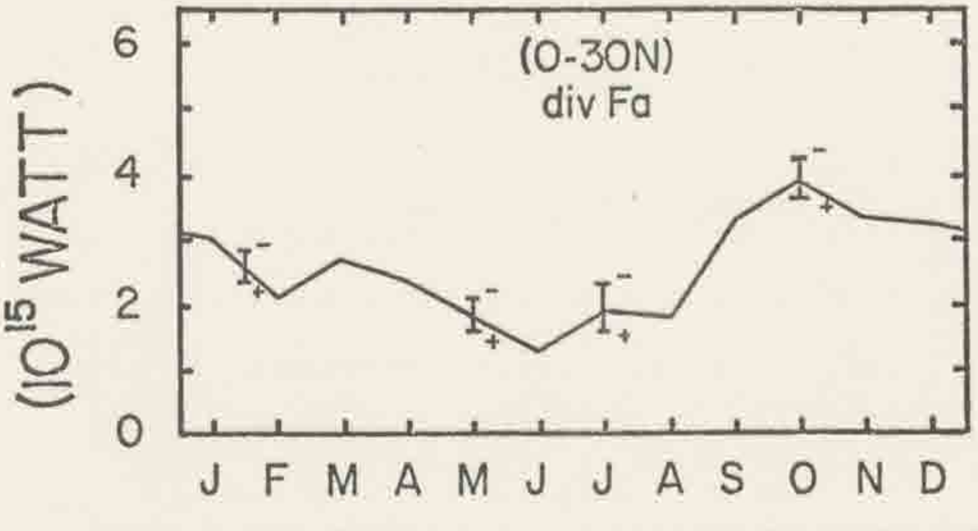

Figure 4.6.: Atmospheric mean meridional energy flux divergence for the equator-to-30N latitude zone.

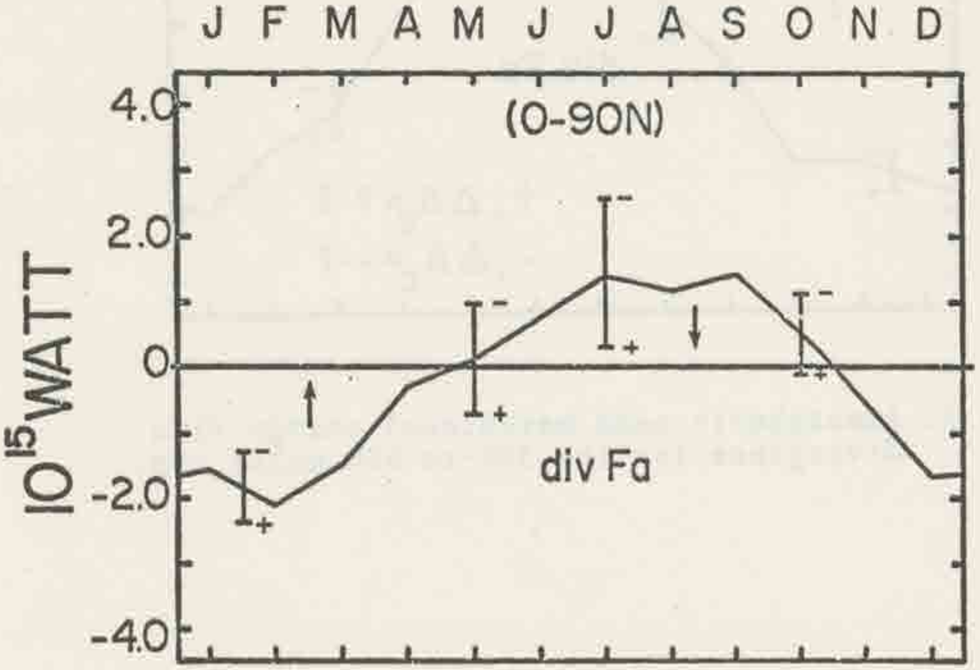

Figure 4.7.: Atmospheric mean meridional energy flux divergence for the equator-to-90N polar cap.

Table 4.1: Zonal Values of $\frac{\partial N}{\partial Ac}$ (wm^{-2})

North Latitude	May 1-15	July 16-31	Oct. 3-17	Jan. 21-Feb. 3
60-70	-34.3	-60.5	-5.6	+21.6
50-60	-72.8	-81.5	-32.6	-9.1
40-50	-54.1	-64.0	-31.5	-30.1
30-40	-33.4	-35.4	-20.3	-41.9
20-30	-11.1	-33.8	-19.7	-14.8
10-20	-18.8	-26.8	-19.4	-10.9
0-10	-29.1	-24.8	-27.4	-27.9

which is quite large in magnitude, will not change the basic shape of the annual divFa profile.

The northward energy transport (Tn) by the atmosphere is opposite in sign to divFa for the polar cap 30N-90N and 0-90N in Figures 4.5 and 4.7, respectively; a positive divergence is an outflow from the cap and a negative divergence is an inflow to the cap, or a convergence. For the polar cap,

$$Tn = -divFa \tag{4.6}$$

A $\Delta Ac = +.1$ in the 30N-90N cap of Figure 4.5 will require of the atmosphere, as an upper limit, a Tn increase of $.3 \times 10^{15}$ watt in January-February and $.75 \times 10^{15}$ watt in July. Likewise, for a $\Delta Ac = -.1$ a response in Tn of the same magnitude and opposite in sign would be required. Note that in July the sign of Tn changes with $\Delta Ac = -.1$ so that a southward energy transport is required of the atmosphere.

A similar analysis for the entire north polar cap, 0-90N, for a $\Delta Ac = \pm.1$ uniformly distributed over 0-90N is shown in Figure 4.7. The sign of Tn would change during the equinoxes with a $+\Delta Ac$ change; however, the overall shape of the divFa or Tn profile with time throughout the year would not change even with such a large change in cloud amount.

The effect on atmospheric transport of removing stratus and stratocumulus clouds east of the subtropical high pressure center in the Eastern Pacific Ocean along the coast of North America is examined. However, in this case the contribution of $\frac{\partial I}{\partial Ac}$ to $\frac{\partial N}{\partial Ac}$ is ignored, so that

$$\frac{\partial N}{\partial Ac} = \frac{\partial Ab}{\partial Ac} \tag{4.7}$$

Ignoring $\frac{\partial I}{\partial Ac}$ is a reasonable assumption in light of this cloud type which prevails near the top of a temperature inversion in the subtropical high pressure regions over a relatively cold ocean surface. Thus, $\frac{\partial I}{\partial Ac}$ would be quite small compared to $\frac{\partial Ab}{\partial Ac}$.

Shown in Table 4.2 is the cloud amount fraction of the type associated with the eastern Pacific high in the latitude zone, 15N-35N (after Miller and Feddes, 1971). The ΔAc for each semi-monthly period is negative which indicates a removal of the cloud. The persistence and area of coverage of the stratus type cloud is largest in July and smallest in January of the four periods. Similarly, $\frac{\partial Ab}{\partial Ac}$ is largest in July, which may be associated with the high, bright clouds of the southwestern Indian Monsoon, as much as with the lower stratus type clouds. The zonal mean sensitivities of the present work do not permit distinguishing sensitivity by cloud type and by longitude. For the most part, the change in $\frac{\partial Ab}{\partial Ac}$ with season is due to seasonal solar radiation weighting on the cloud albedo. The January solar

Table 4.2: Sensitivities associated with removal of stratus-type clouds from the Eastern Pacific Ocean in the 15N-35N latitude zone.

	Jan.-Feb.	May	July	Oct.
ΔAc	-.017	-.022	-.045	-.028
$\frac{\partial Ab}{\partial Ac}$ $(10^{15}W)$	-3.84	-6.42	-6.46	-4.02
$\Delta divFa$ $(10^{15}W)$	.07	.14	.29	.11
Tn (40N) $(10^{15}W)$	3.7	2.4	1.6	3.5
%Tn (40N)	1.8	5.9	18.2	3.2

weighting in the 15N-35N zone is approximately 65 percent of the July solar weighting; it accounts for 85 percent of the difference in $\frac{\partial Ab}{\partial Ac}$ between the two periods.

Application of equations (4.7), (4.4) and (4.5) yields ΔdivFa as shown in Table 4.2. The ΔdivFa is four times larger in July than in the January-February period. The present day Northward transport of energy by the atmosphere across the 40N latitude circle (shown in Table 4.2 as Tn) was taken from Oort and Vonder Haar (1976). Inspection of their Table 9 reveals that all of the divFa in the 15N-35N zone goes into positive northward transport across the 40N latitude circle. If it is assumed that the direction of energy transport by the atmosphere remains identical to that of the present climate regime with a removal of the subtropical high pressure stratus type clouds in the eastern Pacific Ocean, then the percent increase in required energy transport may be calculated. (It must be assumed under a global radiative equilibrium constraint that a ΔN of equal magnitude but opposite in sign takes place north of 40N, so that this energy transport may occur). These percentages range from 1.8 in January-February to 18.2 in July (Table 4.2).

A more realistic study than has been discussed in the previous case studies is to determine the sensitivity of divFa in the 0-30N latitude zone to year-to-year changes in cloud amount which are associated with the intertropical convergence zone (ITCZ). Cloud amount interannual variability for various latitude zones within the 30N-30S zone has been determined by Murakami (1975). He derived it from 7 years of gridded TIROS nephanalyses. The variability of ΔAc in the 0-15N latitude zone for each of the four semi-monthly periods was taken from his Figure 6. This zone was selected as being representative of the variability in cloud amount associated with the ITCZ. These ΔAc values are shown in Table 4.3. Cloud amount variability in the July period is twice that in the January-February and October periods.

The ΔdivFa has been computed for the entire 0-30N latitude zone for a ΔAc in the 0-15N latitude zone with equations (4.4) and (4.5). As expected, ΔAc and ΔdivFa are opposite in sign and divFa is two or more times larger in July than in any other period. Using the same reasoning as used in the previous case on stratus clouds in partitioning ΔdivFa into northward energy transport in the same proportion as the divFa of today's climate regime, the percent change in northward energy transport at both 30N and the equator were computed as shown in Table 4.3. A decrease in cloud amount by 0.05 in the 0-15N zone during July may be balanced by both a northward energy transport across 40N and a southward energy transport across the equator, which are nearly equal in magnitude. A similar argument holds for the other periods in which the sensitivities are condiderably less.

Table 4.3: Sensitivity of the atmospheric energy transport out of the 0-30N latitude zone to interannual variations of cloud amount in the 0-15N latitude zone.

	Jan.-Feb.	May	July	Oct.
ΔAc	±.025	±.040	±.050	±.025
$\frac{\partial N}{\partial Ac}$ (10^{15}w)	-1.10	-1.15	-1.81	-1.67
$\Delta divFa$ (10^{15}w)	∓.028	∓.046	∓.090	∓.042
fn	1.00	.94	.26	.87
Tn(30N)(10^{15}w)	4.4	1.7	0.5	3.4
% Tn (30N)	∓0.6	∓2.5	∓4.6	∓1.1
Tn (Eq.) (10^{15}w)	1.9	-.1	-1.4	-.5
% Tn (Eq.)	0	±3.0	±4.8	±1.0

The foregoing hypothetical cases were presented to demonstrate what may be considered as an upper limit to the immediate response of the atmosphere energy transports to changes in cloud amount. The significance of the atmospheric response should be determined through climate model sensitivity studies.

4.2 Global and Hemispherical Sensitivity

Global and hemispherical intergrated values of various parameters appear in Table 4.5. The poleward limits of integration used were 65N and 65S latitude. The 29 month set of measurements because of the large sample size, allows for better global integrated mean statistics than the Nimbus 3 data set. If global (90N-90S) annual mean cloudy statistics are compared between the Nimbus 3 and the 29 month data sets, one sees that the 29 month set shows a planet which is both brighter and colder than the Nimbus 3 set. This comparison is shown in Table 4.4.

Table 4.4 - Annual Global Statistics (90N-90S)

	ALBEDO	LONGWAVE (wm^{-2})
29 month	.301	235.7
Nimbus 3	.280	242.0

Table 4.5 - Summary of satellite derived statistics.

		MAY	JULY	OCT.	JAN-FEB	NIMBUS 3 ANNUAL	29 MONTHS ANNUAL
65N-65S	$\frac{\partial Ab}{\partial Ac}$	-72.0	-65.8	-70.9	-67.5	-69.8	-83.8
	$\frac{\partial I}{\partial Ac}$	-50.5	-36.4	-34.8	-26.0	-36.6	-46.7
	$\frac{\partial N}{\partial Ac}$	-21.5	-29.4	-36.1	-41.5	-33.2	-37.1
	αc	0.359	.347	0.355	0.350	0.354	0.389
	Ac	0.553	0.557	0.579	0.578	0.568	0.568
	αT	0.268	0.263	0.269	0.268	0.268	0.288
	αm	0.156	0.158	0.151	0.156	0.155	0.155
65N-0	$\frac{\partial Ab}{\partial Ac}$	-88.3	-87.1	-58.1	-43.3	-66.2	
	$\frac{\partial I}{\partial Ac}$	-55.3	-43.4	-34.1	-22.4	-38.5	
	$\frac{\partial N}{\partial Ac}$	-33.0	-43.7	-24.0	-20.9	-27.7	
	αc	0.376	0.369	0.345	0.348	0.360	
	Ac	0.522	0.525	0.530	0.534	0.528	
	αT	0.277	0.274	0.263	0.275	0.271	
	αm	0.169	0.169	0.170	0.191	0.172	
65S-0	$\frac{\partial Ab}{\partial Ac}$	-55.6	-44.5	-83.7	-91.6	-73.4	
	$\frac{\partial I}{\partial Ac}$	-45.7	-29.3	-35.5	-29.5	-34.8	
	$\frac{\partial N}{\partial Ac}$	- 9.9	-15.2	-48.2	-62.1	-38.6	
	αc	0.337	0.316	0.354	0.341	0.346	
	Ac	0.585	0.590	0.629	0.622	0.608	
	αT	0.253	0.243	0.273	0.264	0.264	
	αm	0.134	0.138	0.136	0.137	0.137	

The annual mean global albedo and longwave flux of the 29 month data set is 7.5 percent higher and 2.6 percent lower, respectively, than that of the Nimbus 3 data set. These differences are assumed to result from the effects of cloudiness differences between the two data sets. Therefore, the sensitivity of the radiation budget to cloud amount within the 65N to 65S latitude zone may be estimated for the 29 month data from the Nimbus 3 statistics within that latitude band. The Nimbus 3 cloudy albedo and cloudy longwave flux values are increased by 7.5 percent and decreased by 2.6 percent, respectively. Nimbus 3 cloud-free statistics are taken together with the cloudy statistics to derive radiation budget sensitivity values for the 29 month set. Table 4.6 compares sensitivity factors derived from both sets of data.

Table 4.6 - Annual Sensitivities (65N-65S)(wm^{-2})

	$\frac{\partial Ab}{\partial Ac}$	$\frac{\partial I}{\partial Ac}$	$\frac{\partial N}{\partial Ac}$
29 month	-83.8	-46.7	-37.1
Nimbus 3	-69.8	-36.6	-33.2

Sensitivities from the 29 month data set are larger than those from the Nimbus 3 data set in all radiation budget components, ie. larger by 14 wm^{-2}, 10 wm^{-2}, and 4 wm^{-2} in absorbed shortwave, emitted longwave, and net flux, respectively.

Global sensitivity factors have been derived in theorectical studies by others. Annual global cloud amount used in this study is 0.568 (Table 4.5, Ac = 0.568 for 65N-to-65S). The global mean value of Ac is quite uncertain. Schneider (1972) used Ac = 0.500, Hoyt (1976) in his model used Ac = 0.532, and Cess used Ac = 0.540. So that a comparison might be made on an equal base cloud amount, all sensitivity factors have been adjusted to an Ac = 0.500, and to a solar constants of 1360 wm^{-2}. These normalized sensitivity values are shown in Table 4.7.

Table 4.7 - Annual Global Sensitivities (wm^{-2})

	$\frac{\partial Ab}{\partial Ac}$	$\frac{\partial I}{\partial Ac}$	$\frac{\partial N}{\partial Ac}$
29 Month** (present study)	-95.2	-53.1	-42.4
Nimbus 3** (present study)	-79.3	-41.6	-37.7
Adem (1967)*	-178.1	-58.4	-119.7
Schneider (1972)	-129.2	-74.6	-54.6
Cess (1976) NH	-88.4	-91.0	+2.6
SH	-81.6	-81.0	-0.6
Hoyt (1976)		-36.7	
Wang & Dimoto (1974)		-66.2	

* Equator to 60N

** 65N-to-65S

The $\frac{\partial AB}{\partial Ac}$ computed by Cess agrees well with results of the present study; they should be in agreement since both studies used cloud-free planetary albedo data, which were derived from the same four Nimbus 3 semi-monthly periods. The $\frac{\partial I}{\partial Ac}$ values in Table 4.7 increase from Hoyt's -36.7 wm^{-2} to the largest value, -91.0 wm^{-2} of Cess. The larger $\frac{\partial I}{\partial Ac}$ of Cess is quite interesting since it nearly cancels $\frac{\partial Ab}{\partial Ac}$ thus giving virtually no global net flux sensitivity to cloud amount. The net flux sensitivities, $\frac{\partial N}{\partial Ac}$, of all other studies are large negative values.

As discussed in Section 2, radiative transfer calculations with models of Schneider (1972) and Cox et al., (1976) did not give a global mean value of cloud free longwave flux equivalent to that derived from the satellite measurements. The global atmospheric temperature and moisture vertical profiles used in the model calculations were undoubtedly not identical to the global atmospheric conditions existing at the time of the Nimbus 3 measurements. However, large descrepancies did exist between the two model results; the satellite measurements fell between them. Given identical model atmospheres and an opaque cloud top at 5.5 km, the model results discussed by Schneider gave $\frac{\partial I}{\partial Ac} = -74.6$ wm^{-2}, while the model discussed by Cox et al. (1976) gave $\frac{\partial I}{\partial Ac} = -52.3$ wm^{-2}. These values differ significantly. The principle difference between the model results may be seen in Figure 4.8. Longwave flux out the top of the atmosphere for a cloud-free

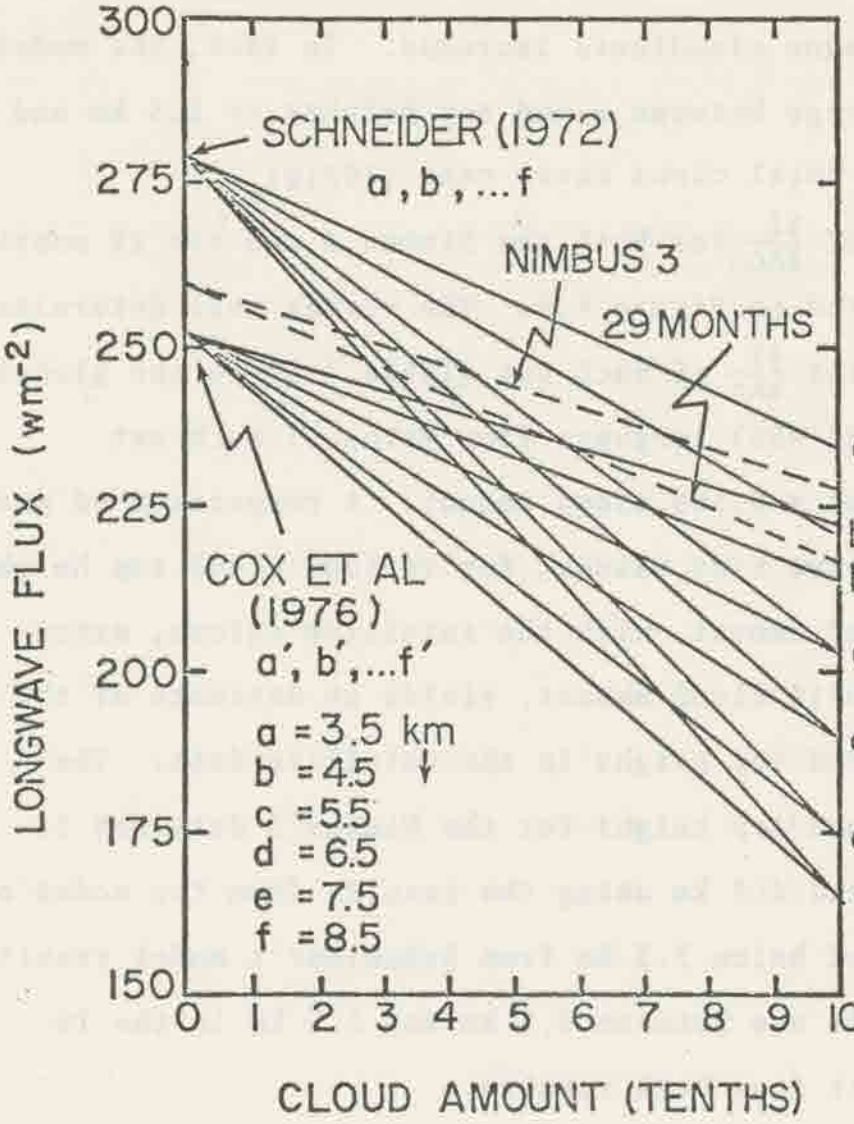

Figure 4.8.: Longwave flux emitted by the earth-atmosphere system as a function of cloud amount for various heights of radiometrically black clouds.

atmosphere differs between the models by 28 wm^{-2}. Differences decrease as both cloud amount and cloud top height of opaque cloudiness increase. In fact, the model results converge between cloud top heights of 5.5 km and 6.5 km for a total cloud cover case (10/10).

Curves of $\frac{\partial I}{\partial Ac}$ for both the Nimbus 3 and the 29 month set are plotted in Figure 4.8. The curves were determined by applying the $\frac{\partial I}{\partial Ac}$ of each set (Table 4.6) to the global integrated (90-90S) longwave flux value of each set (Table 4.5) at a 0.568 cloud amount. A comparison of model derived longwave flux values, for various cloud top heights at 10/10 cloud amount, with the satellite values, extrapolated to 10/10 cloud amount, yields an estimate of the effective cloud top height in the satellite data. The effective cloud top height for the Nimbus 3 data set is between 3.5 and 4.5 km using the results from the model of Cox et al, and below 3.5 km from Schneider's model results. The cloud tops are between 4.5 km and 5.5 km in the 29 month data set from both results.

Schneider (1972) found that he could obtain a zero net radiation balance at the top of the atmosphere by inserting into his longwave transfer calculations opaque cloud tops at a 5.5 km height. The satellite results indicate that effective opaque cloud top heights are at some height below 5.5 km. However, if global cloud amount is taken as 0.500 rather than 0.568, the slope of the satellite curves in Figure 4.8 will increase. Under this condition, the 29 month curve will indicate effective opaque cloud top heights to be at 5.5 km.

The difference in $\frac{\partial I}{\partial Ac}$ between Schneider's and the 29 month satellite values (Table 4.7) might be largely attributed to uncertainty in the global model atmosphere used in the radiative transfer calculations to compute cloud-free longwave flux. Cess (1976) obtained $\frac{\partial I}{\partial Ac}$ by differentiating a parametric function, which described the emitted longwave flux as a function of surface temperature and cloud amount. He derived similar empirical relationships for both the Northern and Southern Hemispheres by applying a least squares fit to annual-mean-zonal dependant variables. Differentiating both expressions with respect to cloud amount yielded -91 wm^{-2} and -81 wm^{-2} for $\frac{\partial I}{\partial Ac}$ of the Northern and Southern Hemispheres, respectively. The latitude dependence of his $\frac{\partial I}{\partial Ac}$ within each hemisphere was less than ±4 wm^{-2}, where as in the present study, it is greater than ±10 wm^{-2} in the annual mean case. It is not clear as to why his $\frac{\partial I}{\partial Ac}$ values are so much larger in absolute value than those of the present study.

The $\frac{\partial I}{\partial Ac}$ derived from both radiative transfer model results are shown in Table 4.8 for various effective cloud top heights. The $\frac{\partial I}{\partial Ac}$ value of the satellite method (-53 wm^{-2} with Ac = 0.50) is equivalent to a sensitivity with effective cloud tops at 5.5 km in Cox's model and between 3.5 km and 4.5 km in Schneider's model.

Table 4.8.: Annual and Global Mean Longwave Sensitivity derived from Models

Cloud Top Height (km)	3.5	4.5	5.5	6.5	7.5	8.5
Cox et al (1976) $\frac{\partial I}{\partial Ac}$ (wm^{-2})	-31.0	-40.0	-52.0	-65.0	-80.0	-91.0
Schneider (1972) $\frac{\partial I}{\partial Ac}$ (wm^{-2})	-45.0	-59.0	-75.0	-89.0	-104.0	-113.0

The $\frac{\partial I}{\partial Ac}$ of Cess allows for effective cloud tops in the Northern Hemisphere at 8.5 km and 6.5 km and in the Southern Hemisphere at 7.5 and 5.5 km, using the Cox and Schneider model results, respectively. Not only is there a large disparity between $\partial I/\partial Ac$ values of various studies but there is a large disparity between the effective cloud top heights of the various studies.

The differences in $\frac{\partial Ab}{\partial Ac}$ in Table 4.7 may be examined in terms of cloud albedo (αc) by differentiating equation (4.8) with respect to cloud amount,

$$\alpha t = \alpha c Ac + \alpha min\ (1 - Ac) \qquad (4.8)$$

to obtain

$$\frac{\partial \alpha t}{\partial Ac} = \alpha c + Ac\, \frac{\partial \alpha c}{\partial Ac} - \alpha min + (1 - Ac)\frac{\partial \alpha min}{\partial Ac} \qquad (4.9)$$

It is assumed that the albedo of clouds and of the cloud-free atmospheres are not functions of the cloud amount, so the equation (4.9) reduces to:

$$\frac{\partial \alpha t}{\partial Ac} = \alpha c - \alpha min \qquad (4.10)$$

Thus, it is seen that $\frac{\partial \alpha t}{\partial Ac}$ is a function of just the albedo above clouds and the albedo of the cloud-free earth and atmosphere system. Global values of αc and αmin which were used by Schneider are 0.50 and 0.12, respectively. Values of αc and αmin derived from the 29 month and Nimbus 3 data sets for the latitude zone 65N-to-65S are 0.389 and 0.155, respectively. The satellite derived αc is based on a cloud amount of 0.568. Now if an Ac of 0.50 is used in equation (4.8) along with the quasi-global albedo data of the 29 month satellite data set, one obtains an αc of 0.421, and a $\frac{\partial \alpha c}{\partial Ac}$ of 0.266 from equation (4.10). The 0.266 value is 30 percent less than Schneider's value of 0.380. Therefore, accuracy in the sensitivity of absorbed shortwave flux to cloud amount is critically dependent upon an accurate measure of the planetary albedo of clouds and of the cloud-free planet.

Schneider (1972) demonstrated that a variation in cloud top height by 0.6 km, while conserving the vertical temperature lapse rate and cloud amount, could cause a $2^{\circ}K$ change of the same sign in surface temperature. He also demonstrated that an increase (decrease) in cloud amount, while conserving the vertical temperature lapse rate and the cloud top height, should decrease (increase) the surface temperature. The magnitude of his temperature change result is model dependent. Since both his study and the present one show $\frac{\partial N}{\partial Ac}$ to be negative, then the sign of the surface temperature change under identical conditions should be the same in both studies. Thus, the results of the present study indicate that an increase (decrease) in cloud amount, while conserving the vertical temperature lapse rate and the cloud top height, should decrease (increase) the surface temperature.

5. CONSLUSIONS AND RECOMMENDATIONS

A number of conclusions are drawn from this study. The principle conclusion is that a uniform increase (decrease) in global cloud amount, with all other factors held constant, will cause a negative (positive) planetary radiation budget to prevail. If the present atmospheric vertical temperature lapse rate is conserved, then the global mean surface temperature will decrease (increase) until radiative equilibrium is restored. Without compensating changes in cloud albedo, emittance, transmittance and height, a uniform change in cloud amount does appear to be a significant climate feedback mechanism.

The cloud effect for the globe as a whole is larger in the absorbed shortwave flux than in the longwave emitted flux. Similarly,the sensitivity of the absorbed shortwave flux to changes in cloud amount is larger than the sensitivity in longwave emitted flux to changes in cloud amount. The cloud effect in the absorbed shortwave flux is significantly larger over ocean surfaces than over land surfaces.

The presence of clouds act to reduce the amplitude of the annual variation of the planetary net radiation budget. The amplitude reduction is mostly in the planetary longwave flux term, because the presence of clouds decrease the transmittance of the atmosphere to longwave flux upwelling from the earth's surface. Thus, the full amplitude of the annual variation in surface temperature is not seen in the planetary longwave flux. The annual variation of the planetary net radiation budget is approximately ±15 wm^{-2}. This variation is apparently real and is caused by : 1) an annual cycle in the incoming solar flux, due to the eccentricity of the earth's orbit around the sun, 2) an annual cycle in the longwave flux, due to large amplitude continental surface temperature changes of the Northern Hemisphere, 3) a semi-annual variation in albedo due to apparent north-south seasonal migration of the sun's path with latitude over dark tropical zones relative to brighter extra tropical zones, and 4) a small residual variation, due to measurement and sampling biases and to time varying atmospheric and surface albedoes.

The cloud-free planetary albedo determined from satellite shortwave radiance measurements was shown to be higher than the value commonly associated with planetary heat budget studies.

It is recommended that a similar study be carried out with the scanning measurements from Nimbus 6 and Nimbus G Earth Radiation Budget (ERB) experiments. This would permit verification of the results derived from the small satellite sample used in this study. An assessment of inter-annual variability, if any exists, in the cloud effect on the planetary radiation budget could also be done.

It is further recommended that the results of this study be implemented in planetary heat budget and "climate" models to test model sensitivity to them.

REFERENCES

Adem, J. 1967: On the relations between outgoing longwave radiation, albedo, and cloudiness. Mon. Wea. Rev., 95, 257-260

Bandeen, W.R.,M. Halev, and I. Strange, 1965: A radiation climatology in the visible and infrared from TIROS meteorological satellites, NASA TN D-2534.

Budyko, M.I. (ed), 1963: Atlas of the heat balance of the globe (in Russian), 69 pp., Moscow Hydrometeorol, Serv., Moscow.

Cess, R.D. 1976: Climate change: An appraisal of atmospheric feedback mechanisms employing zonal climatology. J.Atmos. Sci., 33, 1831-1843.

Chen, T.S. 1975: Monthly minimum and maximum albedoes, Memorandum to William Smith, Chief, Radiation Branch, NOAA/NESS Washington, D.C.

Clapp, P.F. 1964: Global cloud cover for seasons using TIROS nephanalyses. Mon. Wea. Rev., 92, 495-507

Coburn, A.R. 1971: Improved three dimensional nephananalysis model. AFGWC TM 71-2, Air Force Global Weather Central, Air Weather Service (MAC), Offutt AFB, NEBR.

Conover, J.H. 1965: Cloud and terrestrial albedo determinations from TIROS satellite pictures. J. Appl Meteor, 4, 378-386.

Cox, S.K. 1973: Infrared heating calculations with a water vapor pressure broadened continuum. Quart. J. Roy. Meteor. Soc., 99, 669-679.

Cox, S.K., M.C. Polifka, K. Griffith, A. Rockwood, D. Starr, 1976: Radiative transfer computational routines for atmospheric science applications, Dept. of Atmospheric Science, Colorado State University, Fort Collins, Colorado.

Crutcher, H.L. and J.M. Meserve,, 1970: Selected-Level Heights, Temperatures and Dew Point Temperatures for the Northern Hemisphere. NAVAIR 50-1C-52 (revised). Chief of Naval Operations, Washington, D.C.

Drummond, A.J., R.J. Hickey, W.J. Scholes, and E.G. Love, 1968: New value for the solar constant, *Nature*, 218, 259-261.

Dutsch, H.U., Photochemistry of atmospheric ozone, *Advances in Geophysics*, 15, 219-322.

Ellis, J.S. 1975: Radiative properties of large scale cloudiness for climate models. Second Conference on Atmospheric Radiation of the American Meteorological Society, Arlington, Virgina.

Ellis, J.S., and T.H. Vonder Haar, 1976: Zonal average earth radiation budget measurements from satellites for climate studies. *Atmos. Sci. Paper 240* Dept of Atmos. Sci., *Colorado State University*, Fort Collins, Colorado.

Ellis, J.S., and T.H. Vonder Haar, 1976: The annual cycle in planetary radiation exhange with space. COSPAR, ICSU, Proceedings of the Symposium on Meteorological Observations from Space: Their Contribution to the First GARP Global Experiment, Philadelphia, Pennsylvania.

Ellis, J.S., T.H. Vonder Haar, J. Levitus, and H.H. Oort, 1978: The annual variation in the global heat balance of the Earth. Accepted for publication in *J. Geophys. Res*.

Flanders, D.H. and W.L. Smith, 1975: Radiation budget data from the meteorological satellites, ITOS 1 and NOAA1. NOAA TM NESS 72.

Frank, W.M. 1976: The structure and energetics of the tropical cyclone. *Atmos. Sci. Paper 258*, Dept of Atmos. Sci., *Colorado State University*, Fort Collins, Colorado.

Gray, W.M., E. Ruprecht, and R. Phelps, 1975: Relative humidity in tropical weather systems. *Mon. Wea. Rev.*, 103, 685-690.

Hauth, F.F., and J.A. Weinman, 1968: Investigation of clouds above snow surfaces utilizing radiation measurements obtained from Nimbus II satellite. *Final Report NASW-65 1958-1968*, Dept. of Meteor. *The University of Wisconsin*, Madison, Wisconsin.

Hoyt, D.V., 1976: The radiation and energy budgets of the earth using both ground-based and satellite derived values of total cloud cover. NOAA TR ERL 362-ARL4.

Joint Organizing Committee, 1975: The physical basis of climate and climate modelling, GARP Publications Series No. 16, Report of the International Study Conference in Stockholm, 29 July-10 August, 1974, WMO/ICSU.

Joseph, J.H., 1971: On the calculation of solar radiation fluxes in the troposphere. Solar Energy, 13, 251-261.

Kornfield, J. and A. Hasler, 1969: A photographic summary of the Earth's cloud cover. Studies on Atmospheric Energetics Based on Aerospace Probings, Annual Report, ESSA Grant E-230-68, Space Science and Engineering Center, The University of Wisconsin, Madison, Wisconsin.

Krueger, A.J. and R.A. Minzner, 1976: A mid-latitude ozone model for the 1976 U.S. Standard Atmosphere. J.Geophys. Res., 81, 4477-4481.

Kukla, G.J. and H.J. Kukla, 1974: Increased surface albedo in the Northern Hemisphere. Science, 183, 709-714.

London, J. 1957: A study of the atmospheric heat balance. Final Report, Contract AF19 (122)-165, Research Division, College of Engineering, New York University, University Heights, New York.

London, J. and T. Sasamori, 1971: Radiative energy budget of the atmosphere, Man's Impact on the Climate, Chapter 6, The MIT Press, 1971.

MacDonald L.H. 1970: Data reduction processes for spinning flatplate satellite-borne radiometers. ESSA TR NESC 52.

McKee, T.B. and S.K. Cox, 1974: Scattering of visible radiation by finite clouds, J. Atmos. Sci., 31, 1885-1892.

Miller, D.B. and R.G. Feddes, 1971: Global Atlas of Relative Cloud Cover, 1967-70. A Joint Production of NOAA/NESS and USAF/ETAC, Washington, D.C.

Murakami, T. 1975: Interannual cloudiness changes. Mon. Wea. Rev., 103, 996-1006.

Nimbus Project Staff, 1969: The Nimbus III Spacecraft System, Nimbus III User's Guide, NASA/GSFC, pp. 1-8.

Oort, A.H. and E.M. Rasmusson, 1971: Atmospheric circulation statistics. NOAA Professional Paper 5, U.S. Dept. of Commerce, Rockville, M.D.

Raschke, E. 1973: Satellites measure the radiation budget of the Earth (in German). Umschau, 73, 464-466.

Raschke, E. and M. Pasternak, 1967: The global radiation balance of the earth-atmosphere system obtained from radiation data of the meteorological satellite Nimbus II, Document X-622-67-383, NASA/GSFC. Greenbelt, M.D.

Raschke, E., T.H. Vonder Haar, W.R. Bandeen, and M. Pasternak, 1973a: The annual radiation balance of the earth-atmosphere system during 1969-70 from Nimbus III measurements. J.Atmos. Sci., 30, 341-364.

Raschke, E., T.H. Vonder Haar, M. Pasternak, and W.R. Bandeen, 1973b: The radiation balance of the earth-atmosphere system from Nimbus III Radiation measurements. NASA TN D-7249.

Ruff, I., R. Koffler, S. Fritz, J.S. Winston, and P.K. Rao, 1967: Angular distribution of solar radiation reflected from clouds as determined from TIROS IV radiometer measurements. ESSA TR NESC-38.

Sadler, J.C. 1969: Average cloudiness in the tropics from satellite observations. IIOE Meteor Monogr., Number 2, East-West Center Press, University of Hawaii, Honolulu.

Sasamori, T., J. London and D.V. Hoyt, 1972: Radiation budget of the Southern Hemisphere, Meteor. Monogr. 13, American Meteorological Society.

Schneider, S.H. 1972: Cloudiness as a global climate feedback mechanism: The effects in the radiation balance and surface temperature of variations in cloudiness. J. Atmos Sci., 29, 1413-1422.

Sellers, W.D. 1965: Physical Climatology, The University of Chicago Press, Chicago and London.

Sikula, G.J. and T.H. Vonder Haar, 1972: Very short range local area weather forecasting using measurements from geosynchronous meteorological satellites. Atmos. Sci. Paper 185, Dept. of Atmos. Sci., Colorado State University, Fort Collins, Colorado.

Simpson, G.C. 1928: Further studies in terrestrial radiation. Memoirs of the Royal Meteorological Society, Vol. III, No. 21.

Simpson, G.C. 1929: The distribution of terrestrial radiation by finite clouds. Memoirs of the Royal Meteorological Society, Vol. III, No. 23.

Taljaard, J.J., H. Van Loon., H.S. Crutcher, and R.S. Jenne, 1969: Climate of the Upper Air: Southern Hemisphere, Vol. I, Temperatures, Dew Points. and Heights at Selected Pressure Levels. NAVAIR 50-1C-55, Chief of Naval Operations, Washington, D.C.

Van Loon, H. 1972: Cloudiness and precipitation in the Southern Hemisphere. Meteor. Monogr., 13, American Meteorological Society.

Vonder Haar, T.H. 1968: Variations of the Earth's Radiation Budget. Ph.D. Dissertation, Dept. of Meteor., The University of Wisconsin, Madison, Wisconsin.

Vonder Haar, T.H. and J.S. Ellis, 1974: Atlas of radiation budget measurements from satellites. (1966-1970) Atmos. Sci. Paper 231, Dept. of Atmos. Sci., Colorado State University, Fort Collins, Colorado.

Vonder Haar, T.H. and J.S. Ellis, 1975: Albedo of the cloud-free earth-atmosphere system, Second Conference on Atmospheric Radiation of the American Meteorological Society, Arlington, Virginia.

Vonder Haar, T.H. and V.E. Suomi, 1971: Measurements of the Earth's radiation budget from satellites during a five year period. Part I: Extended time and space means. J. Atmos. Sci., 28, 305-314.

Vowinckel, E. and S. Orvig, 1970: The climate of the north polar basin. World Survey of Climatology, Volume 14, Chapter 3, ed. S. Orvig, Elsevier Publishing Company, Amsterdam-London-New York.

Wang, W. and G.A. Domoto, 1974: The radiative effect of aerosols in the Earth's atmosphere. J. Appl, Meteor., 13, 521-534.

Washington, W.M. and L.G. Thiel, 1970: Digitized global monthly mean ocean surface temperatures, NCAR-Tn 54, Boulder, Colorado.

Winston, J.S. 1967: Planetary scale characteristics of monthly mean longwave radiation and albedo and some year-to-year variations. Mon. Wea. Rev., 95, 235-256.

Winston, J.S. and V.R. Taylor, 1967: Atlas of world maps of longwave radiation and albedo: for seasons and months based on measurements from TIROS IV and TIROS VII. ESSA TR NESC 43.

Zdunkowski, W.G. and W.K. Crandall, 1971: Radiative transfer of infrared radiation in model clouds, Tellus, XXIII, 517-527.

Zdunkowski, W., D. Henderson and J.V. Hales, 1965: The influence of haze on infrared measurements, detected by space vehicles. Tellus, XVII, 147-165.

Zdunkowski, W.G., and R.L. Weichel, 1971: Radiative transfer in haze atmospheres, Contributions to Atmospheric Physics, Vol 44, 53-68.

APPENDIX A

The Ocean Reflectance Model

"Ocean" and "Cloud-land" directional reflectance and bi-directional reflectance models which were applied to Nimbus 3 MRIR satellite measurements are described in Raschke et al. (1973). The directional reflectance part of the "cloud-land" and ocean models gives the dependence of directional reflectance on solar zenith angle. It is a model derived from a limited number of measurements by a number of authors.

The effects of application of the directional reflectance model to a directional reflectance value, $r\ (\xi)$, may be simulated. This is accomplished by assuming a value for the directional reflectance at zero solar zenith angles, $r\ (\xi=0)$, and then applying the model. It is described mathematically by:

$$r(\overline{\xi}) = R(\overline{\xi})\ r(\xi=0) \tag{A.1}$$

with ξ = solar zenith angle

$r(\overline{\xi})$ = the daily mean directional reflectance

$r(\xi=0)$ = directional reflectance at zero solar zenith angle and

$$R(\overline{\xi}) = \frac{\int_{Td}^{Tn} \frac{r\xi(t)}{r(\xi=0)} \text{Cos } \xi \text{ (t) dt}}{\int_{Td}^{Tn} \text{Cos } \xi \text{ (t) dt}} \qquad \text{(A.2)}$$

with Td, Tn = Time of sunrise and sunset, respectively.

The expression, $\frac{r(\xi)}{r(\xi=0)}$, is the directional reflectance model as given in Table A.1. The table values were taken from Sikula and Vonder Haar (1972), which were tabulated from graphs in Raschke et al. (1973). In Table A.1., there are two reflectance models: a cloud-land model and a cloud-free ocean model. For the application of the cloud-land model in estimating albedo over clouds as a function of solar zenith angle, a value of 0.25 was selected for $r(\xi=0)$. This value was taken from earlier work of Ruff et al. (1967) in which they investigated the angular dependence of solar radiation from clouds with TIROS IV measurements.

The ocean model was applied to obtain an upper limit for albedo over a cloud-free ocean. This upper limit is applied as an albedo cutoff; values larger than it are considered to contain cloud contamination while those lower are considered cloud-free. The value for $r(\xi=0)$ was taken from Conover (1965) as 0.09. Of course, this value is high, but it is used only as an upper limit.

Table A.1.: Directional reflectance relative to the value at solar zenith angle of zero degrees for the Nimbus III ocean and cloud models

ζ	Cos ζ	Ocean $\left(\frac{r(\zeta)}{r(\zeta=0)}\right)$	Cloud $\left(\frac{r(\zeta)}{r(\zeta=0)}\right)$
0°	1.00	1.00	1.00
18°	0.95	1.00	1.00
26°	0.90	1.00	1.00
32°	0.85	1.00	1.00
37°	0.80	1.00	1.05
41°	0.75	1.03	1.10
45°	0.70	1.10	1.14
49°	0.65	1.20	1.18
53°	0.60	1.30	1.22
57°	0.55	1.40	1.28
60°	0.50	1.60	1.32
63°	0.45	1.80	1.38
66°	0.40	2.00	1.42
69°	0.35	2.20	1.48
72°	0.30	2.50	1.52
75°	0.25	2.80	1.55
78°	0.20	3.10	1.58
81°	0.15	3.40	1.60
84°	0.10	3.70	1.60
87°	0.05	4.00	1.60

APPENDIX B

Sensitivity of the Broadband Longwave Radiance Model to Clouds

The method by which radiance values from the four longwave spectral channels of the MRIR (Medium Resolution Infrared Radiometer) aboard the Nimbus 3 satellite were converted to a longwave broadband radiance value(3 to 30 um) has been discussed by Raschke et al. (1973). A least squares relationship between spectral radiances and broadband radiances was derived by using radiances which were calculated from model atmospheres. Radiances were calculated at various zenith angles and at eight different cloud levels from a set of 160 model atmospheres. The purpose in this section is to assess the sensitivity of that derived empirical relationship to changes in the spectral radiances as clouds, at various levels, are introduced into a model atmosphere.

The emperical relationship between spectral longwave radiances in the four channels and the broadband longwave radiance derived by Raschke et al. is:

$$Nt = Ao + A_1N_2 + A_2N_2^2 + A_3N_2^3 + A_4N_4 + A_5N_1 + A_6N_3 \qquad (B.1)$$

where Nt is the broadband radiance, $N_{1...4}$ are the spectral radiances and $A_{1..6}$ are the regression coefficients. The coefficients and the standard error of estimate are given in Table B.1.

A global model atmosphere was selected for this experiment. (The model atmosphere is discussed in Section 2.3.2). Broadband and spectral longwave radiances were calculated for this atmosphere for various cloud top heights by applying broadband and spectral radiative transfer models, as discussed in Cox et al. (1976). The spectral resolution of the spectral model was 10 cm^{-1}. The spectral intervals used in the radiance calculation could not be precisely matched to the channel spectral intervals. The channel spectral intervals, defined by the half power spectral interval of the channel response function, and the spectral intervals used in the model calculation are shown in Table B.2. The radiance measured by each channel is represented by:

$$N_i = \int_{\nu 1}^{\nu 2} f_i(\nu) N(\nu)\, d\nu \qquad \text{(B.2)}$$

where fi is the normalized spectral response function for channel "i", N is the spectral radiance and ν1 to ν2 denote the spectral interval of the channel response. Equation (B.2) was applied to the model calculated spectral radiances in an approximate form, as

$$N_i = \int_{\nu 1(\frac{1}{2})}^{\nu 2(\frac{1}{2})} N(\nu)\, d\nu \qquad \text{(B.3)}$$

Table B.1. Regression coefficients (A) and standard error of estimate (e) for equation (B1) (Raschke et al., 1973)

A0($calcm^{-2}min^{-1}$)	A1	A2	A3	A4	A5	A6	e($calcm^{-2}min^{-1}$)
0.0160	0.00385	0.000317	-0.951×10^{-5}	0.0139	0.00215	0.003144	0.00070

Table B.2. Infrared spectral channels of the MRIR of the Nimbus 3 satellite.

Channel	Half Power Interval		Model	
	um	cm^{-1}	cm^{-1}	Weighting function peak
1	6.35-6.72	1488-1575	1485-1585	Upper tropospheric water vapor
2	10.1-11.2	893-990	895-995	Window channel
3	14.5-15.8	633-690	635-695	Lower stratospheric CO_2
4	20.8-23.2	431-481	435-485	Lower tropospheric water vapor

where a normalized rectangular response function, fi = 1, was applied across the spectral interval of the half power channel response, defined between wave number ν_1 (½) and ν_2 (½). The approximate equation (B.3) was used because the limited spectral resolution of the radiative transfer model did not justify using the exact equation (B.2).

The outgoing longwave radiance values, computed by equation (B.1) and by the broadband radiance transfer model for a no-cloud case and for three cloud top altitude cases, are shown in Table B.3. The differences between equation (B.1) computed values (empirical) and the broadband radiative transfer model values (model) also are shown in the table. The difference between the model results and the empirical results are quite large. Some of the difference may be attributed to differences between the prescribed radiative characteristics of the absorbers and the numerical methods applied within the three different radiative transfer models used to compute broadband radiances, spectral radiances and the coefficients of equation (B.1). The differences may also be attributed to not computing radiance values, using Cox's spectral model, over spectral intervals identical to those intervals for which the coefficients in equation (B.1) were derived.

Even though the difference between the empirical and model computed broadband radiances is quite large for each cloud case, the sensitivity of the empirical results to

Table B.3. Spectral broadband empirical, roadband model and spectral radiances calculated for a model atmosphere.

Cloud Top Height (km)	Broadband Radiance ($wm^{-2}sr^{-1}$)			Spectral Radiances ($wm^{-2}sr^{-1}$)			
	Model	Empirical	Difference	Channels 1	2	3	4
no clouds	86.103	99.863	-13.760	0.302	8.381	3.059	4.893
3.5	72.820	85.755	-12.935	0.301	5.796	3.058	4.720
5.5	64.200	76.364	-12.164	0.294	4.499	3.058	4.345
8.5	51.249	62.245	-10.996	0.244	2.935	3.051	3.551

cloud top height can be determined by examining the difference of the differences between the cloud cases. This difference of a difference will be called a D2 difference. The broadband differences for the no-cloud and the 8.5 cloud top cases differ (a D2 difference) by 2.8 $wm^{-2}sr^{-1}$ (Table B.3). This difference exceeds the 0.05 $wm^{-2}sr^{-1}$ (0.00070 $calcm^{-2}sr^{-1}$) standard error of regression of equation (B.1) (Table B.1) by nearly two orders of magnitude. This D2 difference value might be attributed to differences in the radiative transfer models used, as was previously discussed. How significant is this D2 difference with respect to the sensitivity of equation (B.1) to changes in height of opaque cloud tops?

The sensitivity of the D2 difference to changes in the spectral radiances input to equation (B.1) should be the largest for no cloud and the 8.5 km cloud top cases. Thus, the no cloud and the 8.5 km cloud top cases have been selected for the sensitivity study. Each channel radiance will be examined for its effect on equation (B.1) and on the D2 differences between the two cases. The channel 3 radiance value does not contribute to the D2 difference, since it does not change significantly between the two cases. The effect of the channel 1 radiance value on the empirical results can be assessed by holding it constant to the no cloud value, and recomputing the empirical value from equation (B.1) for the 8.5 km cloud top case. The empirical value for the 8.5 km cloud top case increases by a mere 0.1 $wm^{-2}sr^{-1}$ when the channel 1 no-cloud radiance value is used in the calculation. Equation (B.1) is quite insensitive to cloud effects in the channel 1 radiances. The bulk of the sensitivity of equation (B.1) to clouds is caused by changes in the radiances of channel 2, the long-wave window channel, and channel 4, the lower tropospheric water vapor channel. The sensitivity of equation (B.1) to channel 4 radiances is tested in the same way as was done with channel 1. Holding the channel 4 radiance constant at the no-cloud case value, 4.893 $wm^{-2}sr^{-1}$, and recomputing the 8.5 km cloud top case with this channel 4 radiance value and equation (1), causes the 8.5 km cloud top broadband empirical value to increase by 13.1 $wm^{-2}sr^{-1}$. Channel 4 radiances account for 35 percent of the broadband difference between the no-cloud and the 8.5 cloud top cases. This increase is 4.8 times greater than the 2.8 $wm^{-2}sr^{-1}$ D2 difference. The channel 2 radiance accounts for the remaining 65 percent of the difference. Equation (B.1) is indeed significantly sensitive to the change in spectral composition of the outgoing spectral radiances due to cloud changes. The sensitivity is significantly larger than the possible errors of this simple test.

If the D2 difference is taken as a lack of sensitivity of equation (B.1) to cloud changes rather than as an experimental error, then it should be examined for its effect on ΔI, the cloud and no-cloud broadband irradiance difference. The 5.5 km cloud top height may be considered as the approximate global mean opaque cloud top height. The D2 value at 5.5 km computed from Table B.3 values is 1.6 $wm^{-2}sr^{-1}$. If 50 percent global cloud cover is assumed, then the D2 difference is reduced to 0.8 $wm^{-2}sr^{-1}$. The earth-atmosphere system is assumed to be a homogeneous and isotropic emitter, so that multiplication of the radiance difference by π yields an irradiance difference of 2.5 wm^{-2}. This irradiance difference is less than 10 percent of the 26 wm^{-2} global ΔI value (see Section 2.3.2).

APPENDIX C

Global Integration

Global integrated values of planetary net flux, albedo, and longwave flux emitted to space were obtained from the 29 months of satellite measurements. These measurements were averaged into zonal profiles of mean months (Ellis and Vonder Haar, 1976).

Global integrated values of longwave flux were computed from the zonal profiles of the 29 month set by:

$$I(t) = \int_{-\pi/2}^{\pi/2} I(\phi,\ t)\ d(\sin\ \phi) \qquad \text{(C.1)}$$

where:

t = month

ϕ = latitude

They appear in Table C.1.

Global integrated values of albedo were also computed from zonal profiles by:

$$\alpha(t) = \frac{\int_{-\pi/2}^{\pi/2} \alpha\ (\phi,\ t)\ S(\phi,t)\ d(\sin\ \phi)}{\int_{-\pi/2}^{\pi/2} S(\phi,t)\ d(\sin\ \phi)} \qquad \text{(C.2)}$$

where symbols are the same as in equation (C.1) and

$$S = SC(\frac{\bar{d}}{d})^2\ \mathrm{Cos}\ (\xi),$$

Table C.1. Mean monthly global planetary radiation budget

	S* INSOLATION (wm^{-2})	α ALBEDO (Percent)	R REFLECTED (wm^{-2})	I EMITTED (wm^{-2})	N NET (wm^{-2})
January	350.7	30.2	105.9	231.1	13.7
February	347.6	30.5	106.0	230.0	11.6
March	342.5	28.8	98.6	227.8	16.1
April	336.8	30.4	102.4	246.8	-12.4
May	332.0	31.4	104.2	245.0	-17.2
June	329.1	31.1	102.4	245.4	-18.7
July	328.8	29.6	97.3	236.5	- 5.0
August	331.1	29.0	96.0	235.2	- 0.1
September	335.7	28.7	96.3	231.1	8.3
October	341.6	29.1	99.4	235.8	6.4
November	347.1	32.0	111.1	232.6	3.4
December	350.5	31.7	111.1	230.7	8.7
Annual	340.0	30.2	102.7	235.7	1.6

* Based on a Solar Constant = 1360 wm^{-2}

the solar insolation. The denominator of equation (C.2) is the global integrated solar insolation, S(t).

The global integrated albedoes were not computed from the 29 month set as presented in Ellis and Vonder Haar (1976), but from a 23 month set (Table C.1). The 23 month set is the 29 month set less 6 months of ESSA 7 measurements. These were excluded because the albedoes from the ESSA 7 were derived by Mac Donald, 1970 with an assumption that radiative equilibrium existed in global net flux. The Table C.1 values show that planetary radiative equilibrium does not generally exist on time scales less than a year.

From the component albedo and longwave flux values, global average net flux, as shown in Table 1, was computed by:

$$N(t) = (I-\alpha(t))\ S(t) - I(t) \qquad (C.3)$$